UCLouvain

École polytechnique de Louvain

Study of Contactless Power Transmission for Rotating Sun Generator Used in Spatial Applications

Author: **Simon KELLEN**
Supervisor: **Marc BEKEMANS**
Readers: **Emmanuel DE JAEGER, Eduardo VASQUEZ**
Academic year 2021–2022
Master [120] in Electrical Engineering

Abstract

Satellites launched into orbit generate the necessary power for their operation from the sunlight using solar panels. To ensure that the power generation is maximum, these solar panels rotate in order to have their surface always facing the sun. The power is then transferred from the solar panels to the satellite via a rotating system called Solar Array Drive System. Nowadays Solar Array Drive Systems use slip rings technology to transfer power from the rotating solar panels to the static satellite. However, slip rings technology suffers from limitations in the harsh spatial environement such as voltage limitation and wear. In this work, a complete satellite power system using a contactless rotating transformer for the power transfer is studied and simulated using LTSpice, in order to chose the best topology for all the parts of the studied system, namely the solar panel, the rotating transformer and the power electronic converter used to transfer power from the solar panel to the satellite without contact. At first, a state of the art on contactless power transfer is presented to help in choosing topologies for the elements making up the entire system. Then, the different parts of the system are modeled and the models are confirmed using LTSpice. Finally, the entire system is modeled and simulated, and three different power electronic converters are compared in order to chose the most suitable for this work.

Acknowledgements

Firstly, I would like to personally thank my supervisor Prof. Marc Bekemans for his constant assistance, insight, and knowledge. I would like to thank him again, for his course on power electronics, and Prof. Emmanuel De Jaeger, for his course on solar panels, as both courses helped me greatly in writing this master thesis.
Finally, I would like to thank my aunt for her correction of my English, and my family for their continuous moral support and encouragement.

Contents

Introduction

Since the start of the spatial conquest, mankind has sent many artificial satellites into the Earth orbit. Their usages and purposes are multiple, ranging from telecommunications to meteorology, and including spying and other observation activities. The common point of all these activities is that they require energy to be accomplished. As a satellite has no direct link to Earth, its energy must be auto-generated, and it comes from an inexhaustible energy source, the Sun. Since Vanguard 1 launched in 1958, nearly all launched satellites come accompanied with solar panels, harnessing energy from the Sun's rays to power them. These solar panels are usually split up across two solar arrays, set up on both wings of the satellite. To maximize the harnessing of energy, these wings have to able to rotate or pivot around an axis in order to have their surface always oriented towards the sun, effectively maximizing the power harnessing. However, a system with moving parts has more chances of failures than a completely static system, explaining why not every satellite use rotating/pivoting solar arrays. Also, a problem arises from the transfer of power from the solar panel to the main body of the satellite, as rotating parts do not allow simple wires to be used to transfer the power. To remedy this difficulty, satellite nowadays have an internal system called *solar array drive system* which is responsible for the transfer of power. These solar array drive systems use slip rings to transfer power, but this technology suffers from drawbacks, particularly in the harsh spatial environment.

Chapter 1 introduces the problem of power transfer in spatial conditions, and lays down the need of contactless power transfer as well as the objectives of this thesis.

Chapter 2 summarizes various solutions and technologies used in contactless power transfer that are useful for the resolution of the objectives set in chapter 1. Different topologies are presented for different elements of the system, and help to find the best solution for this thesis.

A complete solar panel is modelled and simulated in Chapter 3. To do so, theoretical background on solar energy and photovoltaic modules modeling is presented. A single solar cell is designed from its datasheet and a solar panel is designed from this solar cell using various simulation techniques.

Chapter 4 chooses the best topology for the magnetic coupling element, and uses different models to design it. The resulting magnetic coupling element is incorporated in the system.

Finally, the complete system is assembled in Chapter 5 to be simulated. A theoretical background on the chosen power electronic converter is presented, and three different topologies of this converter are simulated and compared, in order to chose the topology that best fits the system.

Chapter 1

Context

This chapter gives context has to why a contactless power transfer is needed between the solar panels and the satellite. First, the spatial constraints are presented, and their impact on the actual slip rings systems are explained. The objectives of this work and the specifications of the system are then introduced.

1.1 Spatial Context

Satellites are launched into orbit, which is an environment with several constraints. Indeed, satellites are launched outside of the Earth protective atmosphere and must face the following constraints:

- Maintenance : As satellites sit far away from the Earth surface, maintenance is nearly impossible, except for some rare software maintenance. As satellites are launched into orbit to accomplish their task for years (even decades), satellite systems are designed to have great robustness and to be fault-tolerant.

- Gravity : The gravity in the Earth orbit is zero. This makes it possible to decrease weight forces and frictions but it also removes the possibility to use convection in sealed systems.

- Vacuum : As there is no gas, convection can not be used to cool down satellites in orbit. Conduction is the only way to cool down satellite systems. This also suggests that the satellite has a significant temperature gradient: the side facing the sun is heated, whilst the side facing the darkness of space is cooled. The satellite systems therefore have to be able to cope with high and low temperatures.

- Radiations & Plasmas : Spatial radiations are made up of particles that are harmful to the satellite systems, and in particular to any part of the satellite that contains semiconductor electronics. Solar radiations also cause plasmas to appear by ionisation of atmospheric molecules. Plasmas encourage the electric discharge phenomenon between conductors. The different technologies found on a satellite have to be robust to those radiations and plasmas.

- Electric Discharge Phenomenon : Electrostatic discharges are caused by a dielectric breakdown that occurs when the voltage difference between two conductors is superior than a voltage threshold called the breakdown voltage. In a gaseous environment, this threshold voltage depends on the outside pressure and distance between the conductors, according to Paschen's law. From this law, curves called *Paschen's curves* can be obtained. These curves, shown in figure 1.1.1, indicate the maximum voltage difference between two conductors that will not induce a dielectric breakdown.

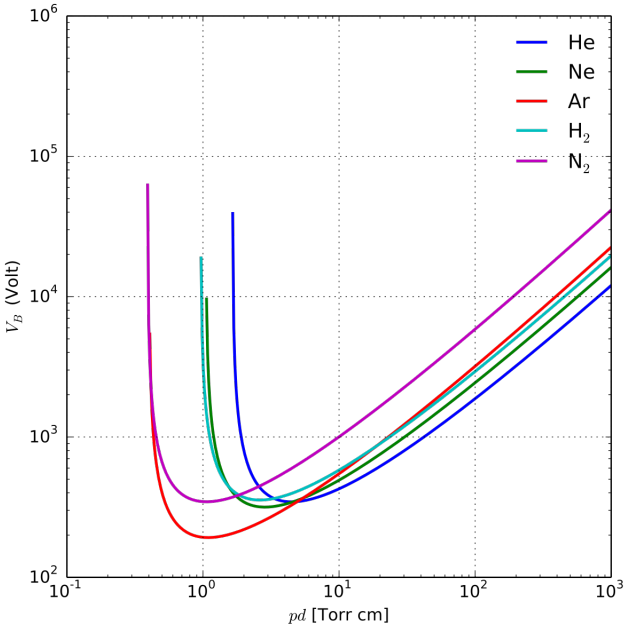

Figure 1.1.1: Paschen's curves for different gases [27]

As shown on figure 1.1.1, the maximum voltage difference in space should be infinite, as there is no pressure in spatial environment. However, as stated earlier, the presence of plasmas, with a non-zero pressure, can lead to dielectric breakdowns happening anyways. Because of this and because of past events, space designers have decided to keep the voltage of bare conductors below the minimum breakdown voltage. The voltage of bare conductors is thus limited to 110 V.

1.2 The Need of Contactless Power Transfer

Slip rings use metallic brushes or collectors which make contact with a rotating metallic ring to conduct current from a rotating body to a static body or inversely. Different slip rings technology exist but all of them have limiting features in spatial applications. Figure 1.2.1 shows a slip ring system used for spatial power transfer.

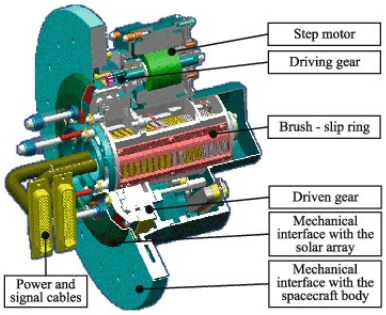

Figure 1.2.1: Slip ring system [51]

As stated in the spatial constraints above, maintenance can not be achieved in space, and the wear induced by the rubbing of the brush on the rotating metallic ring is therefore problematic for long-term uses. The limitation in voltage imposed by the presence of plasmas and the risk of electric discharges happening is also a limiting constraint set upon slip rings uses, especially when high power transfer is needed.

Figure 1.2.2 shows the power system present inside a satellite. The energy of the Sun is harnessed by the solar arrays, and is then transferred to the power conditioning and distribution unit by the solar array drive system. The power is stored in batteries or used directly by the satellite to accomplish its various tasks. Figure 1.2.2 shows a solar array drive system made with a slip ring technology, but as seen previously, this technology presents drawbacks in spatial applications. A new system studied by Thales Alenia Space to replace the slip rings technology is the center of this work. This new system uses a contactless magnetic coupling rotating element to replace the slip ring and effectively transfer power from the solar arrays to the satellite, without any kind of wires or contacts between the two.

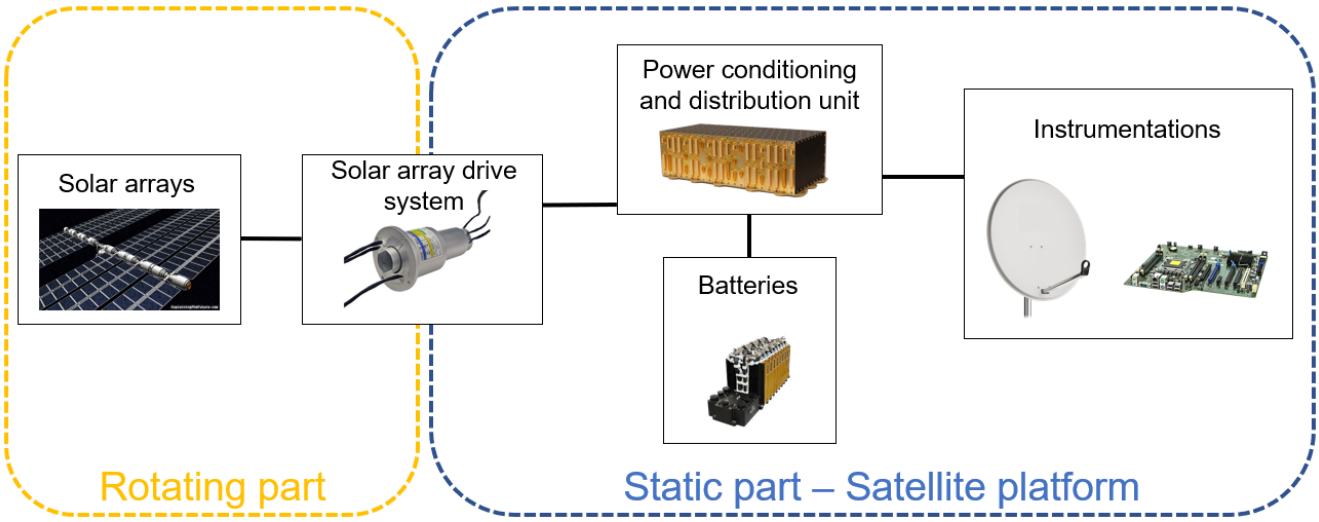

Figure 1.2.2: Satellite Power System

1.3 Objectives and Specifications

The objective of this thesis is to design an effective contactless power transfer system able to replace the slip rings technology to transfer power from a solar array to a satellite. To do so, it is necessary to have a good understanding of the already existing contactless power transfer technologies, as well as power electronics converters and solar arrays systems. For this purpose, a complete system has been modelled and simulated using LTSpice, in order to understand how the system behaves, and to compare different topologies of power transfer. In this regard, the following elements of the system have been modelled analytically and simulated with LTSpice:

- **Solar panels** : In order to understand the nature of the source of energy of the satellite, a complete simulation of the solar panels has been made, from the simulation of a single solar cell.

- **Magnetic Coupling Element** : To transfer the power from the solar panels to the satellite, a magnetic coupling element has been studied and modelled to be fitted into the simulation of the whole system.

- **Power Electronics** : As the magnetic coupling element introduces magnetizing currents, a power electronic converter is needed to avoid a saturation of the material making up the core of the magnetic coupling element. Three different topologies of power electronic converters are studied, simulated and compared, namely a current-driven converter, a voltage-driven converter, and a resonant converter.

All these elements were modelled using realistic, existing materials such as semiconductors, circuit elements and solar cells. The final objective of this thesis is to obtain a power-voltage curve at the output of the system that is similar to the power-voltage curve of the solar panel feeding energy into the satellite. The system has to be able to transfer 5 kW of power at a maximum of 150 V.

Chapter 2

State of the Art on Contactless Power Transfer

This chapter aims to present the vast knowledge existing on contactless energy transfer and used throughout this thesis. It begins by delving into the history and the different types of contactless energy transfer. Afterwards, an overview of the different power electronics used in the literature will be presented, as well as the different magnetic coupling elements used in different applications.

2.1 Types of contactless power transfer

Contactless, or wireless, power transfer is the transmission of electrical energy without contact, or without wires, between a transmitter, which is connected to an energy source, and a receiver, which can be connected to a load. The energy transfer relies on the principles of electromagnetism. The receiver extracts power from a time-varying electromagnetic field created by the transmitter. Contactless power transfer is useful for applications where mobility is one of the predominant manufacturing factor, and also in applications where connecting wires is impractical, or not possible.

Contactless power transfer can be divided into two main categories, and each of them can again be divided into different technologies of power transfer. The two main categories are near-field and far-field (or non-radiative and radiative) energy transfers. Far-field (or radiative) techniques use beams of electromagnetic radiations. They can be used to transfer energy over long distances but the beams must be aimed at the receiver. These techniques are not used in this thesis.

Near-field (or non-radiative) techniques use fields to transmit energy over small distances. The two main technologies are capacitive coupling, which uses an electric field to transfer energy between metal electrodes, and inductive coupling, which uses a magnetic field to transfer energy between coils of wire. Both technologies can be improved efficiency-wise by using resonant circuits. In this thesis, inductive coupling as well as its resonant counterpart will be used.

A small comparison of the different techniques and technologies with their advantages and drawbacks, as well as an application example, is shown in table 2.1.

Technology	Type	Advantages	Drawbacks	Possible application
Inductive Coupling	Near-field	Simple Safe High efficiency	Short distance Expensive	Transfer of energy between PV panel and load in a satellite
Capacitive Coupling		Low cost	Decreases low frequency gain of system Can introduce distortions at low frequencies Smaller frequency range	Charging portable devices
Resonant Inductive Coupling		Efficiency	Complex	Electric vehicles
Microwaves	Far-field	Long distances	Low efficiency	Solar power satellites
Light waves		Long distances	Ultra-high frequency Low efficiency	Charging portable devices

Table 2.1: Comparison of the different contactless power transfer technologies

2.1.1 Inductive Coupling

In inductive coupling, coils of wires on the transmitter side create an electromagnetic field, which will be intercepted by coils of wire on the receiver side. The coils on the transmitter and receiver sides form together a magnetic coupling element, which most of the time is a transformer. The source, often via a power electronic circuit, feeds an alternating current to the transmitter coil. By Ampere's law, this creates an electromagnetic field which oscillates and passes through the receiver's coil. As an oscillating electromagnetic field passing through a coil creates an EMF by Faraday's law of induction, an alternating current is created in the receiving coil, and fed to the load. This alternating current can either be fed directly to the load, or be rectified and transformed into a direct current to feed the load.

The transferred power is dependant on several parameters. The frequency of the alternating current, the mutual inductance between the coils and the distance between them all influence the efficiency of the inductive power transfer. The coupling coefficient k is often used to characterize such efficiency. Its value is $k = \frac{M}{\sqrt{L_1 L_2}}$, with M being the mutual inductance between the coils and L_1 and L_2 being the inductances of the transmitter coil and the receiver coil, respectively. k can be seen as the *fraction of magnetic flux through the transmitter coil L_1 that passes through the receiver coil L_2 when L_2 is open circuited.*

The closer together the coils are, the closer k will be to 1 and the efficiency will be close to 100%. So to achieve high efficiency, the coils must be very close to each other, usually a few centimeters. A scheme representing inductive coupling can be seen in figure 2.1.1.

As explained above, inductive power transfer can only achieve high efficiency at very short distances. However, using resonant inductive coupling can help achieve the same efficiency for greater distances.

2.1.2 Resonant Inductive Coupling

When using an inductive coupling, a large part of the magnetic flux generated by the transmitter coil will be transformed into energy by the receiver coil, but a part of this magnetic flux will not be coupled and will therefore be lost. This part of the flux is called the leakage flux. The open-circuit voltage appearing on the receiver coil will be smaller than expected, because of this leakage flux. This leakage flux is modelled by a leakage inductance, L_μ. By adding a capacitance of the right

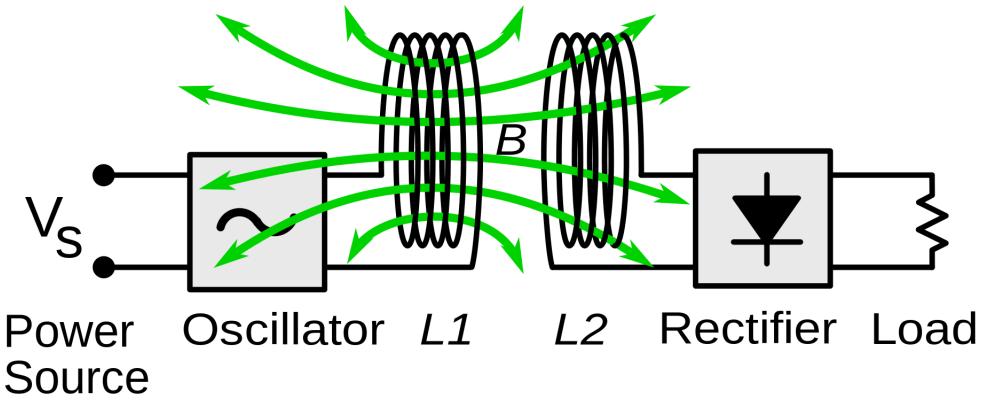

Figure 2.1.1: Inductive Power Transfer [33]

value, this leakage inductance L_μ can be used to create a resonant circuit. This technique is called leakage inductance compensation. The resonant circuit will help the system to exchange energy faster than it loses it, and therefore cut losses and help with exchanging energy over a longer distance. Resonance will also prevent switching losses, by allowing the device to perform Zero-Current Switching (ZCS) or Zero-Voltage Switching (ZVS), as it will be demonstrated further in this thesis.

Different topologies of leakage inductance compensation exist, using series or parallel montages. Namely:

- Series-Series (SS)
- Series-Parallel (SP)
- Parallel-Series (PS)
- Parallel-Parallel (PP)

The first letter stands for the topology of the primary side of the transformer, while the second letter stands for the secondary side. Topologies with series compensation have been studied and analysed extensively in various works [33]. Models of the four different topologies can be seen in figures 2.1.2 and 2.1.3.

(a) Series-Series (SS)

(b) Series-Parallel (SP)

Figure 2.1.2: Models of leakage inductance compensation topologies with series compensation at the primary side

(a) Parallel-Series (PS)

(b) Parallel-Parallel (PP)

Figure 2.1.3: Models of leakage inductance compensation topologies with parallel compensation at the primary side

2.2 Qi Standards

In 2008, the Wireless Power Consortium was created and introduced global interface standards for contactless power transfer, and called it Qi. Qi standards use inductive power transfer to charge Qi devices when set down on a Qi pad, bypassing the need to plug in a charging cable, as shown on figure 2.2.1. Companies like Asus, Samsung and Sony adhered to the standard and used it to develop wireless charging in their products. In 2017, the Wireless Power Consortium introduced the Power Class 0 specification, which enables the transfer of power from 5 to 30 W. Practically, the charging pad and the device will exchange information on the power that needs to be exchanged before the start of the charging phase.

Figure 2.2.1: Mobile phone charging on a Qi pad

The Power Class 0 specification sets a standard operating frequency range from 87 up to 205 kHz. The amount of power transferred can be controlled via the operating frequency used, but it is not mandatory to do so. The amount of power transferred is inversely proportional to the operating frequency, so a lower operating frequency will result in more power transferred. Hence

power transmitter using the operating frequency to control the amount of power transferred will have a resonant frequency near the lower end of the operating frequency range [6]. In the same fashion, the standard for the charging area specifies the outer diameter of the power transmitter coil (50 mm) and the coil in the power receiver (40 mm). Maximum power transfer is obtained when the coils are perfectly aligned, so charging pads usually feature a spot to place the device. However, multiple coils in the power transmitter can be connected in an array or in a matrix, as seen in triple coil charging stands shown on figure 2.2.2, that allow multiple devices of different sizes and coil locations to charge with the Qi pad.

Figure 2.2.2: Triple coil charging Qi stand

As inductive charging uses a magnetic field to transmit power from the Qi pad to the device, it is important to protect the device from the magnetic field to avoid deterioration of the device or the formation of Eddy current inside the device, which will lead to power dissipation which will in turn lead to a temperature increase in the device. To prevent the magnetic field having an impact on parts of the device where it should not, the device should be separated from the secondary coil via *shielding*. The Shielding should be placed on the top face of the secondary coil and should cover it completely.

Another safety parameter is over-voltage protection. If an user poorly places a device on the charging pad and a large current in the primary coil is required to transfer the appropriate charging power, and then suddenly the user improves the coupling by changing the position of the device, it is possible that large voltages will be present in the secondary coil and will be harmful for the device. To avoid this scenario, a 20 V limit is set on the output voltage and is implemented by controlling on the current circulating in the primary coil. This limit is defined according to the amount of power exchanged [6], in order to avoid being unable to meet the target power level when a load is connected.

2.3 Power Electronics

The power electronics used in contactless power transfer can be divided in two categories. At the transmitter side, an inverter is tasked to create an alternating current to feed the primary coil, which will lead to the apparition of the time-varying magnetic field. At the receiver side, this magnetic field will induce an alternating current, which if needed has to be transformed into a direct current via a rectifier.

2.3.1 Inverter

The role of the inverter is to transform a DC signal into an AC, square signal. Multiple topologies able to achieve this are found in the literature and presented below.

2.3.1.1 H-Bridge

The H-Bridge or Full-Bridge is the most commonly used inverter for contactless power transfer. It consists of two branches, each having two switches. The switches can be implemented with MOSFETs or BJTs. The H-Bridge model can be seen in figure 2.3.1a.

The switches SW1 and SW4 are controlled to open and close at the same time, opposite to the switches SW2 and SW3. From t_0 to t_1, SW1 and SW4 are closed, and SW2 and SW3 are open. The voltage between V_+ and V_- is thus the source voltage V_{in}. From t_1 to t_2, no switches is closed, to avoid over-voltages due to the saturation of the magnetic coupling element. More about that will be seen later in this thesis. From t_2 to t_3, the switches SW2 and SW3 are closed, and the switches SW1 and SW4 are open, so the voltages between V_+ and V_- is $-V_{in}$. The voltage between V_+ and V_- is thus a square wave of amplitude V_{in}. The waveforms can be seen in figure 2.3.1b.

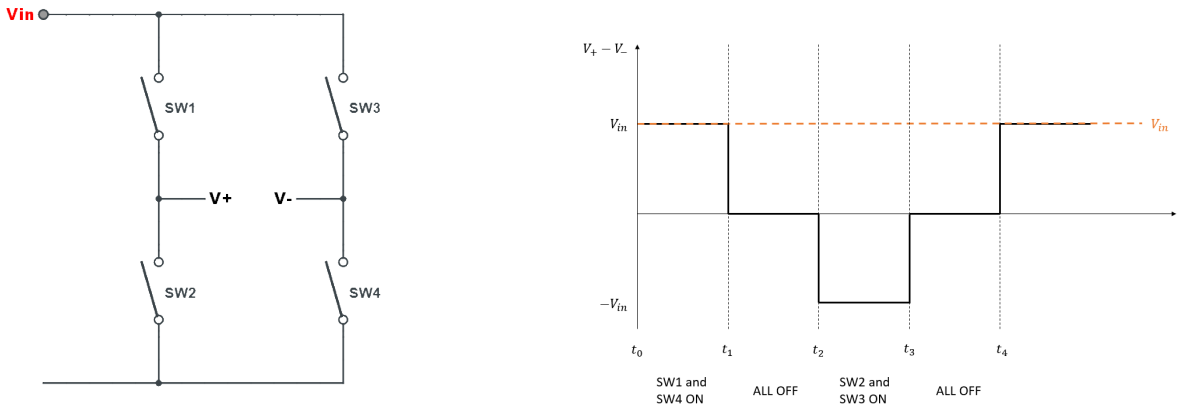

(a) H-Bridge model

(b) H-Bridge waveforms

Figure 2.3.1: Model and waveforms of the H-Bridge

2.3.1.2 Half-Bridge

The Half-Bridge is used in some works on contactless power transfer [38] [10]. It reassembles the H-Bridge except that the switches SW3 and SW4 are replaced by capacitances of the same value to absorb alternating current. From t_0 to t_1, the switch SW1 is closed and the switch SW2 is open. As the capacitances have the same value, they both have the same voltage across their terminal, equal to $V_{in}/2$. So the voltage between V_+ and V_- is $V_{in} - V_{in}/2 = V_{in}/2$. As with the H-Bridge, no switch is open from t_1 to t_2 to prevent the magnetic coupling element from saturating. From t_2 to t_3, the switch SW2 is closed and SW1 is open. The voltage between V_+ and V_- is thus $0 - V_{in}/2 = -V_{in}/2$. The model and waveforms of the Half-Bridge can be seen in figure 2.3.2.

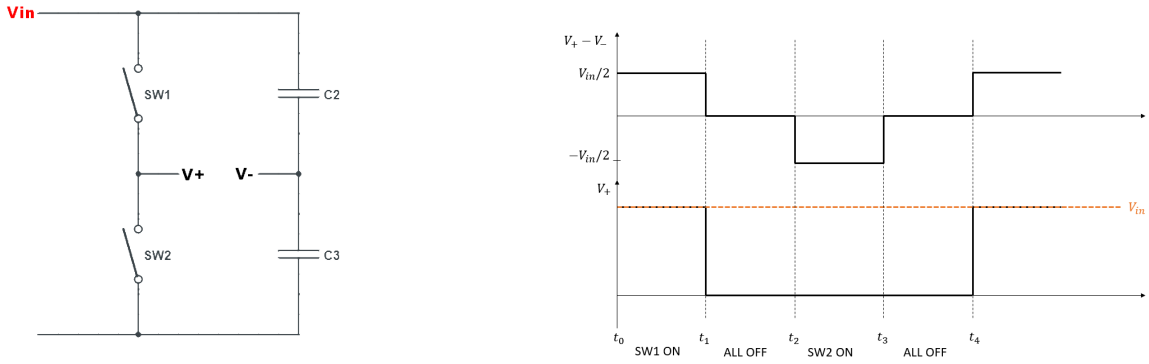

(a) Half-Bridge model

(b) Half-Bridge waveforms

Figure 2.3.2: Model and waveforms of the Half-Bridge

An advantage of this topology is that the command of the electronics is simplified, as there are only two switches instead of four. But as the power output stays the same and the voltage is divided by two, there is two time more current circulating in the switches, so the use of silicium stays the same. But practically, this topology has a drawback related to the parasitic resistances of the capacitors used. The circuit can not be correctly polarized because of them. To prevent this problem, smaller, parallel, resistances have to be added to have a smaller impedance and a reference voltage of $V_{in}/2$.

2.3.1.3 Boost-Converter

[22] combines the Half-Bridge with a Boost Converter in order to get a desired voltage at the input of the bridge, which is higher than the source voltage. The model of the Boost-Converter, combined with the Half-Bridge, can be seen in figure 2.3.3.

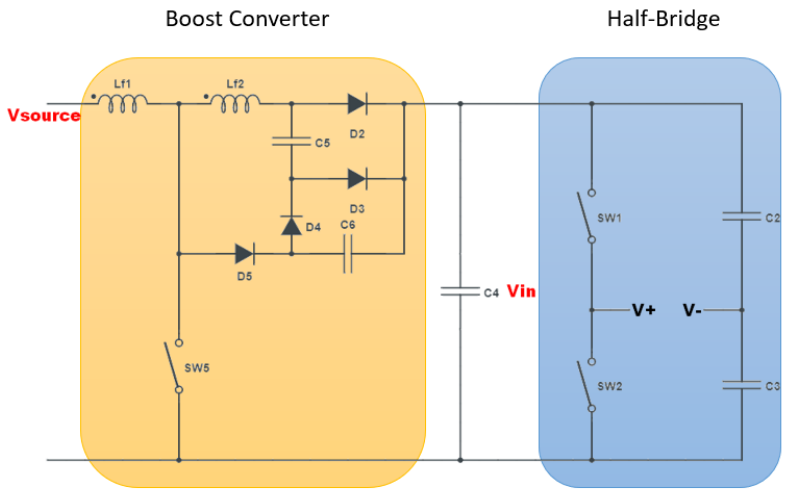

Figure 2.3.3: Boost Converter and Half-Bridge

This Boost Converter is based on a high efficiency, lossless snubber. From t_0 to t_1, the switch SW3 is open and diode D_2 is conducting, so the voltage at the output of the boost converter is V_{in} and the capacitor C_4 charges itself. Between t_1 and t_3, the switch S3 is closed. The mutual inductor L_{f2} discharges itself via the low impedance path created by the capacitors C_5 and C_6. The capacitor C_4 discharge itself to ensure that the output voltage is still at V_{in}. From t_3 to t_4, the switch SW3 is still closed so there is no current flowing in the right part of the circuit. When the switch SW3 opens again, from t_4 to t_5 the current flows trough the diode D_5 and the capacitor C_6 and the output voltage goes back to V_{in}. From t_5 to t_6 current flows out of L_{f2} again to reach the output via diode D_3 and capacitor C_5. Current flows and waveforms can be found in figure 2.3.4a and 2.3.4b. [22]

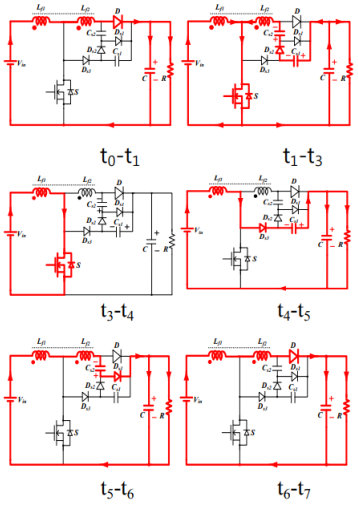

(a) Boost Converter current flows

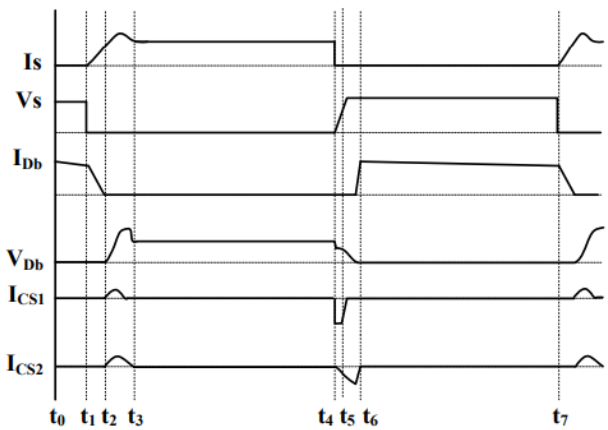

(b) Boost Converter waveforms

Figure 2.3.4: Current flows and waveforms of the Half-Bridge [22]

2.3.2 Rectifier

The role of the rectifier is to transform the AC, square signal received in the secondary coil into an DC signal to feed the load. Multiple topologies able to achieve this are found in the literature and presented below.

2.3.2.1 Passive Rectifier

Passive rectifiers are widely used in contactless power transfer. The reason for their popularity is their passive nature, which means that no control circuit must be implemented. Their principle rely on passive diodes. When V_s is positive, diodes D_1 and D_4 are conducting, providing a way for the positive voltage to the load, and a way to the ground. When V_s is negative, diodes D_2 and D_3 are conducting, to rectify the negative voltage into a positive voltage for the load and still providing a path to the ground.

In practice, a capacitor is added in parallel with the load to have a smoothing of the output voltage. The output voltage increases when the diodes are conducting and decreases with the discharging of the capacitor. The time constant $\tau = R \cdot C$ must be high to have the smoothest output voltage possible. However, an excessive capacitance value can be harmful to the diodes. If τ increases then the conduction time of the diodes t_{ON} decreases. As the mean current in the load is constant, the diodes will have to provide that current in a shorter time span, leading to higher current peaks in the diode. The drawbacks of passive rectifiers is that their harmonic content is high, they also tend to have a low power factor and due to the voltage drop on the diodes they have a low efficiency.

A model of a passive rectifier and its waveforms can be seen in figure 2.3.5.

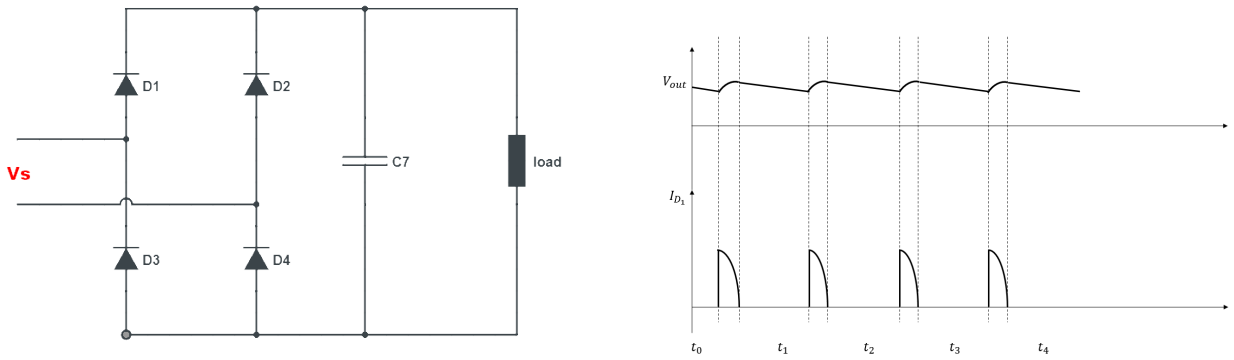

(a) Passive Rectifier Model

(b) Passive Rectifier waveforms

Figure 2.3.5: Current flows and waveforms of the Passive Rectifier

2.3.2.2 Active Rectifier

Active rectifiers solve most of the drawbacks of passive rectifiers. They do not generate harmonics, their power factor is close to unity and they have a higher efficiency since the voltage drop across MOSFETs is lower than the voltage drop across diodes. But this topology requires a command circuit. The model is the same as with the passive rectifier, except that the diodes are replaced with MOSFETs or IGBTs. Diodes are added in parallel with the transistors to provide a path for the current. When an active rectifier is used at the secondary and a H-Bridge at the primary, the total circuit is called a Dual-Active Bridge.

The principle of rectification remains the same as the passive rectifier, except that the setting ON and OFF of the transistors has to be done via a command circuit. One command technique is to compare the DC current at the output with a reference DC current, then input the error into a PI controller, which output will be multiplied with a $cos(\omega t)$ created by a PLL fed with the input voltage. This product, which represents the reference current, is compared to the actual input current, and the current error is fed to a PR (proportional resonant) controller. The output of the PR controller is added to the input voltage to get the reference voltage, which is fed to an unipolar PWM generation block. Inside this block, the reference voltage is compared with a triangular carrier wave, the output of each comparison (with positive and negative reference voltage) is sent to each transistors. The model of the active rectifier and the proposed control technique can be seen in figure 2.3.6.

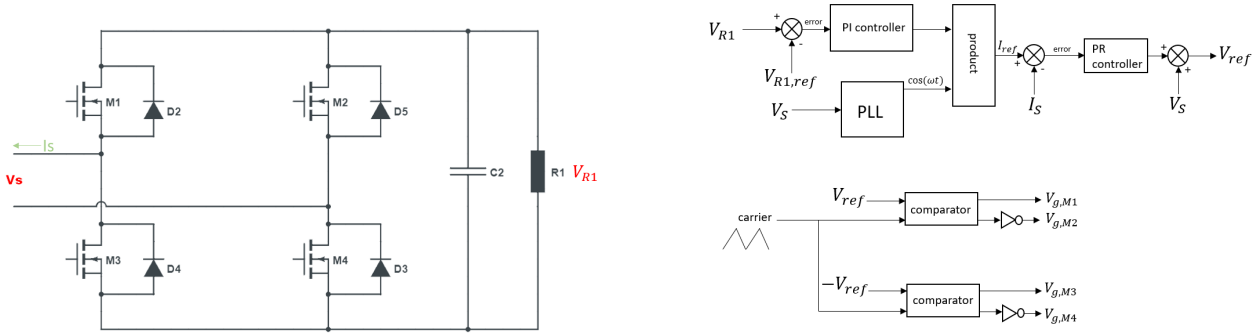

(a) Active Rectifier Model

(b) Active Rectifier proposed control circuit

Figure 2.3.6: Model and proposed circuit of the Active Rectifier

2.3.2.3 Passive rectifier with two diodes

Another passive topology using only two diodes is presented in [36]. When V_S is positive, the current in inductor L_1 increases, and when V_S is negative, the diode D_1 conducts, and so the current in L_1 decreases. The opposite happens in inductor L_2. This topology uses less diodes, but the output voltage is only half of the RMS value of V_S. The model and the waveforms of this topology can be seen in figure 2.3.7.

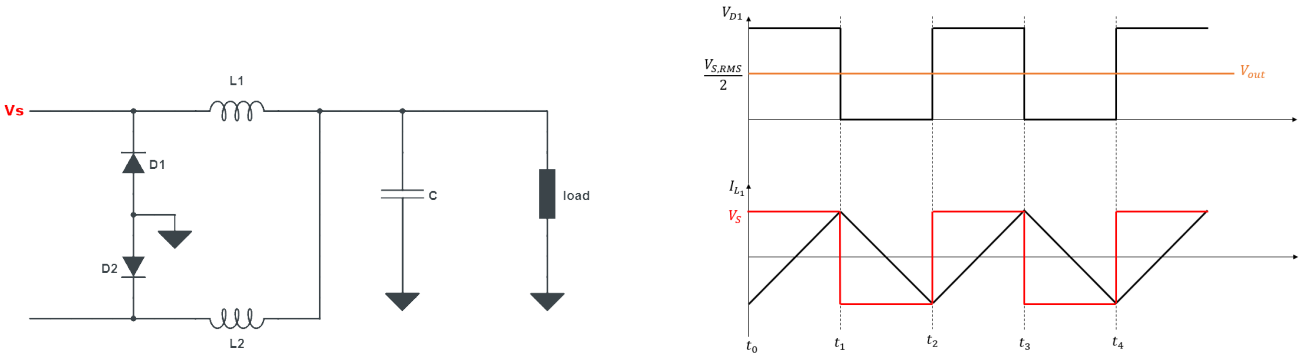

(a) Passive Rectifier with 2 diodes Model

(b) Passive Rectifier with 2 diodes waveforms

Figure 2.3.7: Model and proposed circuit of a Passive Rectifier with 2 diodes

2.4 Magnetic Coupling Element

Between the inverter and the rectifier, a magnetic coupling element with inductive coupling factor k transmits the energy from its primary coil to its secondary coil. As the secondary is not physically connected to the primary, it can be movable. This adds mobility, flexibility and safeness to the design. The mobility of the secondary can be linear or rotating. The magnetic coupling element is often a transformer and its core will be different depending on the air gap length and the power range used. Applications with multiple primary or secondary coils can also be found in the literature.

2.4.1 Qi Reference Designs

Qi Power Class 0, introduced in chapter 2.2, sets standards for contactless power transfer for device charging. The standards also include magnetic coupling elements reference designs.

The power transmitter reference designs include two different design groups. The first group, called **Type A**, includes power transmitter designs with one or more primary coils, but with only a single one activated at a time. The other group, called **Type B**, includes designs with an array of primary coils. One or more primary coils from the array can be activated at the same time. Several reference designs are presented in [7]. This document presents the mechanical (number of coils, form, diameter, thickness, number of turns per layer, etc...) and the electrical (electrical diagram of the power electronics circuits used, PID parameters for control, etc...) details used for each primary and secondary coils reference designs. As the number of reference designs presented is quite extensive, they will not be all covered in this thesis, but Power Transmitter Design A2 will be presented as an example.

Power Transmitter design A2 uses a single circular shaped primary coil, as shown in figure 2.4.1. This primary coil consists of a Litz wire having an equivalent of 30 strands of 0.1 mm of diameter. Litz wires are a type of wire made to carry current at high AC frequencies. These wires reduce the skin and proximity effects, seen in chapters 4.6.1 and 4.6.2. Litz wires consist of multiple strands of thin wire which are individually insulated and are then twisted together following a pre-indicated pattern. Figure 2.4.2 shows the difference between a Litz wire and a stranded wire.

The primary coil consists of multiple layers, which are all stacked with the same polarity.

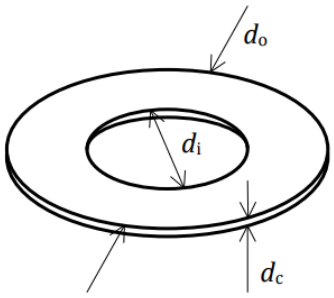

Figure 2.4.1: Primary coil of power transmitter design A2 [7]

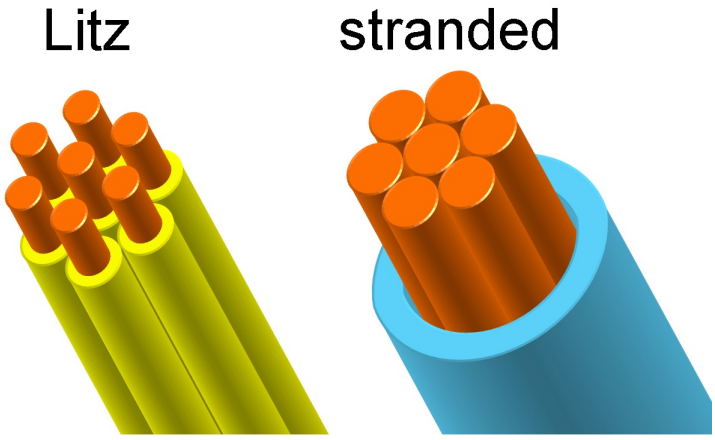

Figure 2.4.2: Difference between a stranded and a Litz wire

Figure 2.4.3 shows the shielding used to protect the rest of the base station from the generated magnetic field. The shielding consists of a combination of Zinc (either with Manganese or Nickel) Ferrite and its thickness should be at least 2 mm.

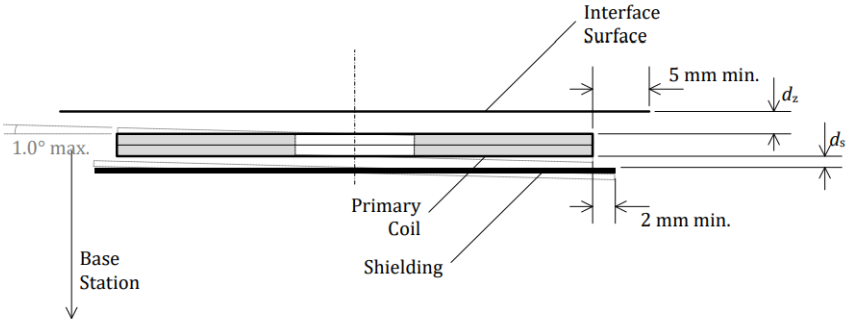

Figure 2.4.3: Shielding of power transmitter design A2 [7]

2.4.2 Rotating Transformer

Rotating transformers are often used in contactless power transfer, typically with a rotating load. Different transformer geometries can be used for a rotating transformer, namely the pot core and axial rotating transformer topologies. Both are shown in figure 2.4.4. Both geometries are compared in [26], which concludes that the pot core transformer geometry has less core and winding losses, as seen in figure 2.4.5, and gives better performances for magnetic coupling and flux densities.

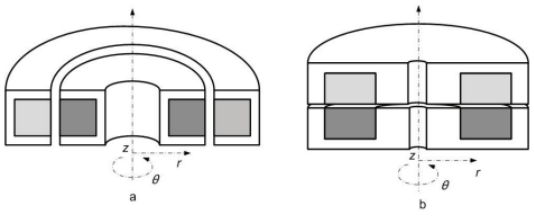

Figure 2.4.4: Axial rotating and pot core transformer geometry [26]

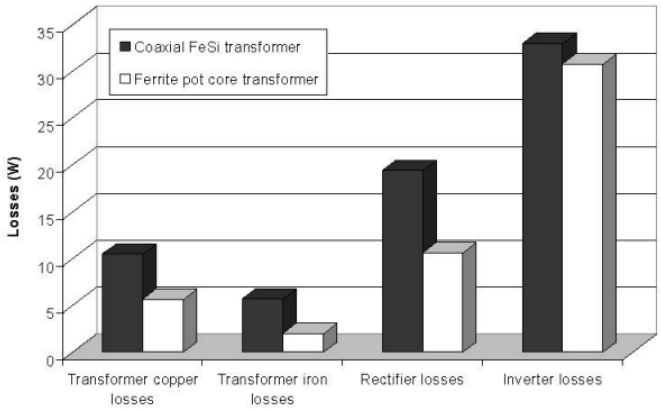

Figure 2.4.5: Comparison of the losses in pot core and axial rotating transformer geometries [43]

Pot core rotating transformers are analysed in details in [45], [44] and [35]. Figure 2.4.6 shows an example of a pot core rotating transformer. Pot core rotating transformers have two different winding topologies, namely adjacent winding and coaxial winding. A comparison between the two different winding topologies is made in [43], showing that lower losses could be obtained with the adjacent winding topology. Both topologies are shown in figure 2.4.7

Another transformer topology for space application is studied in [5]. The transformer is made of multiple pairs of ferrite assembly around a core. The transformer design is shown in figure 2.4.8. This designs has great flexibility given by the changeable size of the C ferrite pairs and by changing their number. Two concepts have been studied, a symmetrical and an asymmetrical number of C ferrites. The analysis shows that a solution with 20 ferrites on one side and 19 on the other gives the best results, improving the whole system stability, reducing cogging torque and allowing smoothing.

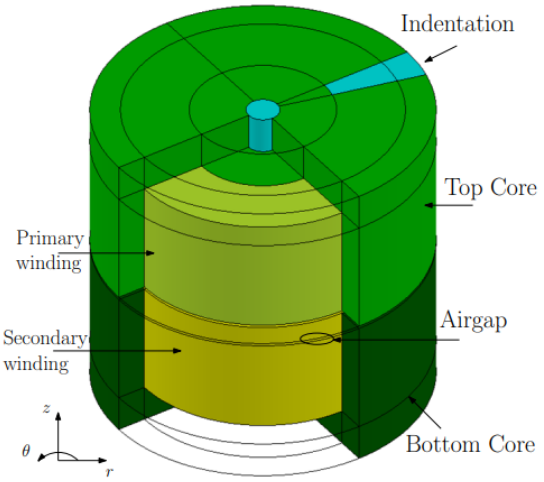

Figure 2.4.6: Pot core transformer design [45]

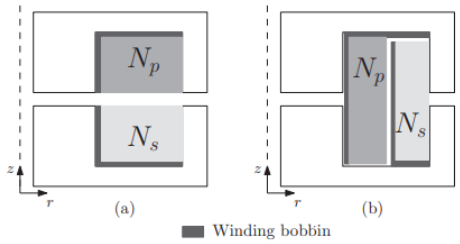

Figure 2.4.7: Adjacent and coaxial winding topologies in a pot core transformer

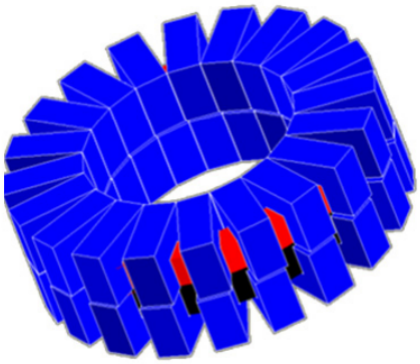

Figure 2.4.8: Proposed transformer from [5]

Rotating contactless power transfer systems can also be used to work with electrical excited synchronous machines, as studied in [28]. In this application the contactless system has to be able to transfer power but also to have an accurate control of the excitation current on the rotor side. Multiple solutions are constructed and analysed.

Another use of Rotating contactless power transfer systems is in association with active vertical maglev inductively coupled structure, notably for medical application. This application is studied in [24] and [25].

Industrial applications can also be found in the literature, notably for radar rotary joint systems [11] and for a commercial drilling tool, taking advantage of the removal of the rotational speed limitation that was present with slip rings [18].

2.4.3 Multiple Secondary

The magnetic coupling element of the contactless power transfer system can feature multiple secondary windings as shown in figure 2.4.9. This configuration is useful when multiple movable loads have to be supplied. It can also be used when the loads are not moving but have to be isolated from the source or from each other. This configuration results in more losses and thus a drop of the total efficiency. [12] took advantage of the flexibility of this topology to develop a new communication system called WISA (wireless interface for sensors and actuators), to provide both wireless communication and power supply to sensors and actuators. This solution has also been studied for use in homes, with [1] and [48] proposing a novel approach to replace plugs and sockets with contactless power transmission systems to increase safety of use. This solution was also used in [37] to supply power to an airbone radar with a rotating transformer.

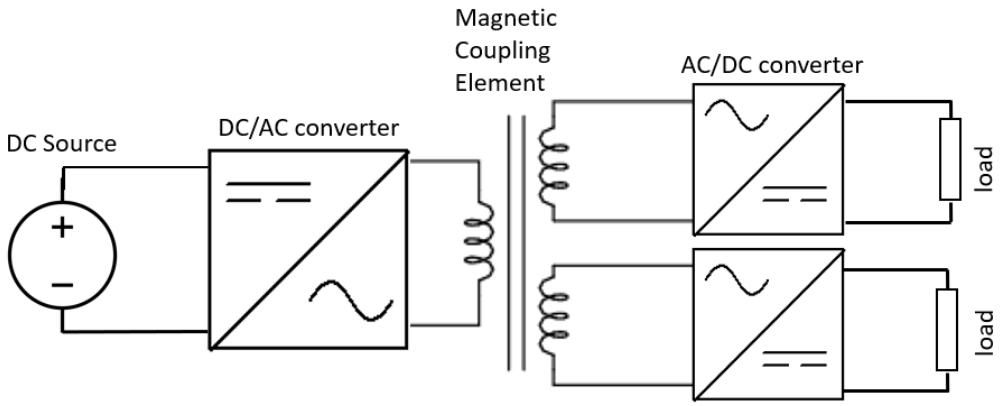

Figure 2.4.9: Magnetic Coupling Element with multiple secondary windings

2.4.4 Multiple Primary

Solutions with multiple primary windings can be used in applications such as charging pads. Power is transferred from multiple primary windings without magnetic cores to a single secondary winding using inductive power transfer across an air-gap. The multiple primary windings are set such that they form a matrix of coils embedded in a flat surface. This arrangement is capable to supply power to an electronic device with secondary windings mounted inside it. This solution is used in [8] to supply an actuator using rectangular shape circular coils, while [46] and [4] use hexagonal and rectangular shape circular coils (figure 2.4.10) in matrices to supply power to charge a laptop

and a drone respectively.

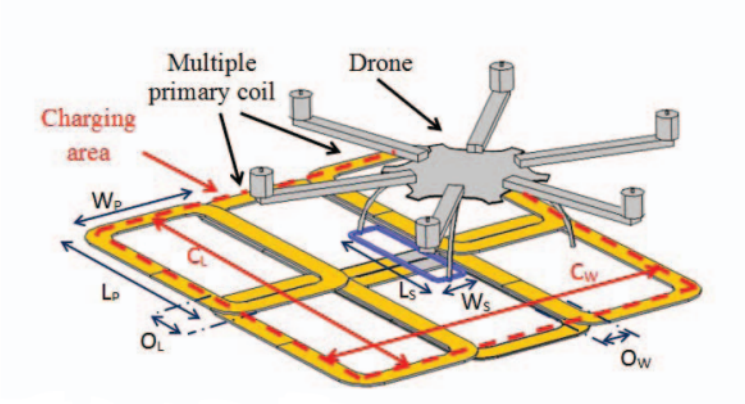

Figure 2.4.10: Rectangular shaped circular coils on a flat surface used to charge a drone [4]

2.4.5 Cascaded Transformers

A system with cascaded transformers (figure 2.4.11) can be used in applications to supply power to different moving secondaries belonging to the same system. [13] uses this topology with rotatable transformers to supply power for multiaxis robots. It transfers energy at a frequency of 25 kHz at 650 V to loads which are electric motors. Another use of this topology is made in [15] for a multi-layer optical disc used in data storage systems to supply electrical power to change the optical reflectivity of an electro chromic layer for layer selection.

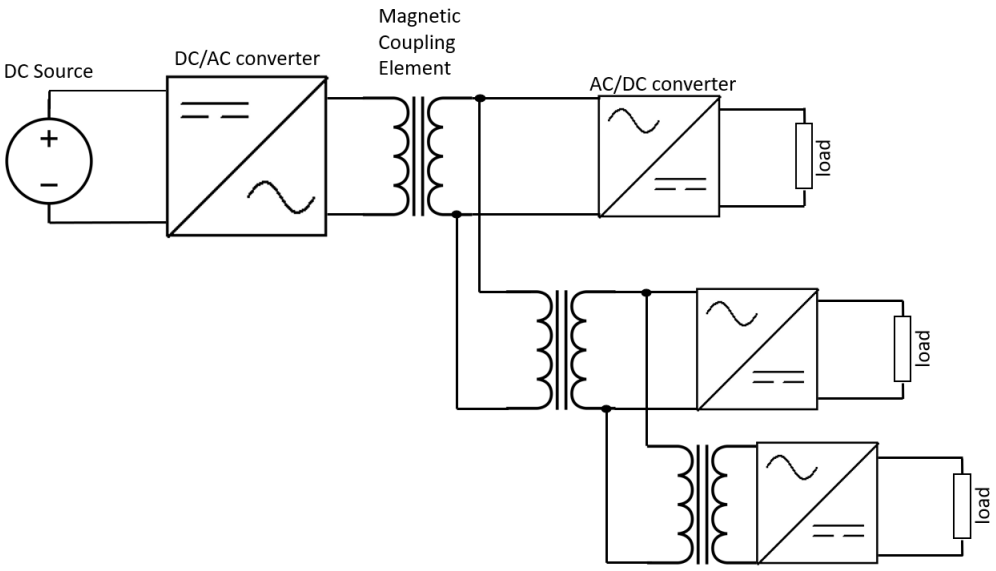

Figure 2.4.11: Cascaded Transformer

2.4.6 Sliding Transformer

Sliding transformers can be used to transfer power over a longer range, while keeping the flexibility advantage of a contactless power transfer. Multiple solutions and applications of sliding transformers can be found in the literature. Practically, two different approaches are adopted. The first one consists of elongating the primary winding to form a loop over the distance needed for the movement of the secondary winding. This topology is used in [30], [23], [3], and [32]. Figure 2.4.12 shows the principle of operation of this topology. Another implementation is studied in [17], where multiple secondary coils slide through the primary coil of a gapped transformer, constructing a long stroke of power transfer, as shown on figure 2.4.13. [47] uses the same method, but with planar coils. Another approach, presented in [49], make use of both primary and secondary cores.

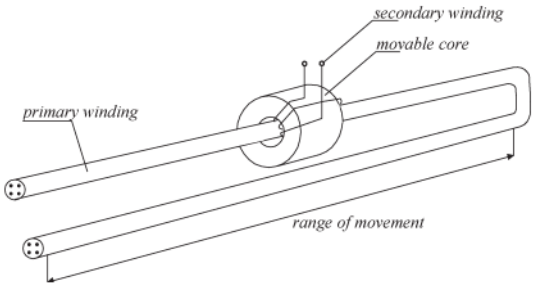

Figure 2.4.12: Sliding secondary coil over long-rage primary coil [23]

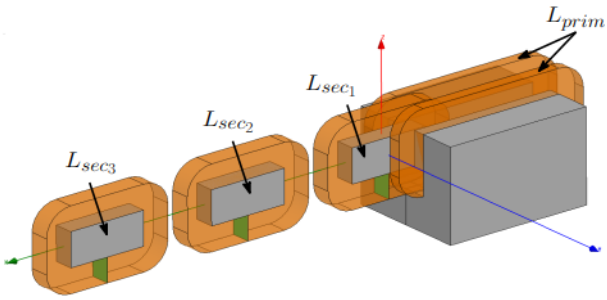

Figure 2.4.13: Sliding secondary coils through the primary coil of a gapped transformer [17]

Chapter 3

PV Panel

The energy used to power the satellite comes from the sun, and more precisely from its light. Light is transformed into electrical energy by a photovoltaic power generation system. The basic element of a photovoltaic power generation system is the photovoltaic cell, an electronic device with electrical characteristics varying when exposed to a light source. This device consists of a junction between two semiconductor layers, or between a metal plate and a semiconductor layer. Each layer is connected to an electrical conductor, to connect the solar cell to an external electrical circuit. The cells are grouped into modules. As each cell provides only a very low voltage, they are connected in series within the modules. Several modules set side by side in the same plane form a photovoltaic panel, and several photovoltaic (PV) panels together form a photovoltaic array, which is the complete power-generating unit.

This chapter will focus on the constitution, operation principles, modeling and design of the photovoltaic array used in the system. This will lead to the design of a solar panel that can be simulated in LTSpice, and that is part of the entire system. The P/V curve of this simulated solar panel will be the point of comparison when simulating P/V curves at the output of the system, and will be useful to visualize the losses present in the system.

3.1 Characterization of the resource

The resource used by PV is solar radiation. It consists of photons carrying energy. The energy carried is given by:

$$E_{ph} = hv = \frac{hc}{\lambda} \tag{3.1.1}$$

with h = 6,626 $\times$ 10^{-34}[J·s] the Planck constant, and c = 2,998 $\times$ 10^{8}[m/s] the speed of light. This expression is often given in eV (electronvolt, 1eV = 1,602 $\times$ 10^{-19} J) and reduces to

$$E_{ph}(eV) = \frac{1.24}{\lambda(\mu m)} \tag{3.1.2}$$

Because $hc = 1.24[eV \cdot \mu m]$. The photon flux is given by $\Phi = \frac{\#photons}{m^2 s}$ and so the power density or irradiance is given by

$$H = \Phi \frac{hc}{\lambda} [W/m^2] \tag{3.1.3}$$

To characterize a light source, the spectral irradiance as a function of a photon wavelength is used. It is denoted by **F**. **F** gives the power density for a particular wavelength. **F** is given in $Wm^{-2}m^{-1}$, with the Wm^{-2} term giving the irradiance at the wavelength λ, given in μm.

Light sources, such as the sun, are modelled as black bodies. A black body is a body that has zero reflectance, meaning that all incident radiations are allowed to pass into it, and zero transmittance, meaning that all incident radiations are absorbed by it. A black body in thermal equilibrium emits radiations according to Planck's law, so the radiations spectrum is determined by temperature alone. The spectral irradiance from a blackbody is therefore given by Planck's radiation law:

$$F(\lambda) = \frac{2\pi hc^2}{\lambda^5 (e^{\frac{hc}{k\lambda T}} - 1)} [Wm^{-2}m^{-1}] \tag{3.1.4}$$

With h the Planck constant and $k = 1,38 \cdot 10^{-23}[JK^{-1}]$ the Boltzmann constant. The total power density from a black body is determined by integrating the spectral irradiance over all wavelengths:

$$H = \sigma T^4 \tag{3.1.5}$$

where T is the temperature of the black body (in K) and σ is the Stefan-Boltzmann constant ($\sigma = 5,67 \cdot 10^{-8}[Wm^{-2}K^{-4}]$).

The peak wavelength of the spectral irradiance is the wavelength at which the spectral irradiance is the highest, meaning that it is the wavelength at which the highest power is emitted. This wavelength is determined by differentiating the spectral irradiance and solving the derivative when it is equal to 0. The result is known as Wien's law:

$$\lambda_p(\mu m) = \frac{2900}{T} \tag{3.1.6}$$

In the case of a photovoltaic array powering a satellite, the resource is the sun. It has a temperature of approximately 5800K, which gives a surface power density of $H_{sun} = 64x10^6[\frac{W}{m^2}]$. So the total power emitted by the sun is calculated by multiplying the emitted power density by the surface area of the sun. It amounts to a total of $3.9 \cdot 10^{26}[W]$. The radiation emitted by the sun is emitted according to Planck's law, so the body's shape or composition does not affect the spectrum of radiation, only the temperature does. Black bodies in thermal equilibrium have two important properties:

- It is an ideal emitter: at every frequency, no other body emits as much energy at the same temperature than the black body.
- It is a diffuse emitter: the energy is radiated isotropically, independent of direction.

To find the solar irradiance on an object, the total power emitted from the sun has to be divided by the surface area over which the sunlight falls. The total solar radiation emitted by the sun is obtained by multiplying the total power density from the sun $H = \sigma T^4$ by the surface area of the sun ($S = 4\pi R_{sun}^2$). The surface area over which the power from the sun falls is $4\pi D^2$, where D is the distance of the object from the sun. This distance is taken from the center of the sun. The solar radiation intensity incident on an object, H_0 in (W/m^2), is given by

$$H_0 = \frac{R_{sun}^2}{D^2} H_{sun} \tag{3.1.7}$$

The solar irradiance at the Earth's atmosphere is about 1.37 $[kW/m^2]$, as shown in figure 3.1.1. However, as the Earth moves in its elliptical orbit around the sun, and because the sun's emitted power is not constant, the actual power density varies slightly. The variation is, however, approximately equal to 3.4%, and for spatial photovoltaic applications the solar irradiance can be considered constant.

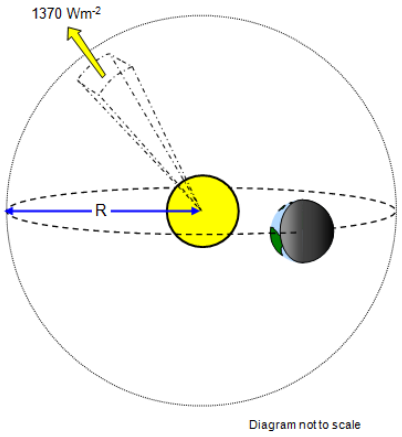

Figure 3.1.1: Visualization of the solar irradiance at the Earth's atmosphere

3.2 PV cells constitution and basic operation principle

The basis of energy production by photovoltaic effect is the generation of charge carriers. A minority and a majority carrier are created when a photon is absorbed by the material. This happens when the energy of a photon is sufficient, meaning that it is greater or equal to the band gap of the material. Photons with an energy lower than the band gap of a material will not interact with the material, or only weakly, and will pass through the material as if it were transparent. When the energy of a photon is much greater than the band gap, then the photon is strongly absorbed. But as the electron quickly thermalize back down to the conduction band edges, the energy of the photon is wasted. When the energy of the photon is equal to the band gap of the material, $E_{ph} = E_G$, there is just enough energy to create an electron-hole pair and the photon is then efficiently absorbed.

The current generated in a solar cell is known as the light-generated current. Two important processes are involved in this current generation. The first process is the aforementioned absorption of photons by the photovoltaic material. Electron-hole pairs are generated in the cell when the energy of the incident photon is greater to or equal to the band gap of the material. But since they are meta-stable, electrons in p-type materials and holes in n-type materials can only persist for about as long as the minority carrier lifetime before recombining. If the carrier recombines, the electron-hole pair produced by the incident photon is lost, and no current or power is produced. The second important process is the collection of these electron-hole pairs by a P-N junction. This process use an electric field present in the P-N junction to separate the majority and minority carriers spatially, to prevent any recombination. When the minority carrier produced by the incident photon reaches the P-N junction, the electric field at the P-N junction sweeps it across the junction, where it becomes a majority carrier. If the solar cell is short-circuited, the carriers generated by the incident photons flow, generating current and voltage. Figure 3.2.1) shows that solar have a spectral response in A/W that is dependent on the wavelength of the incident photon, and that cells are not ideal, and are subject to losses.

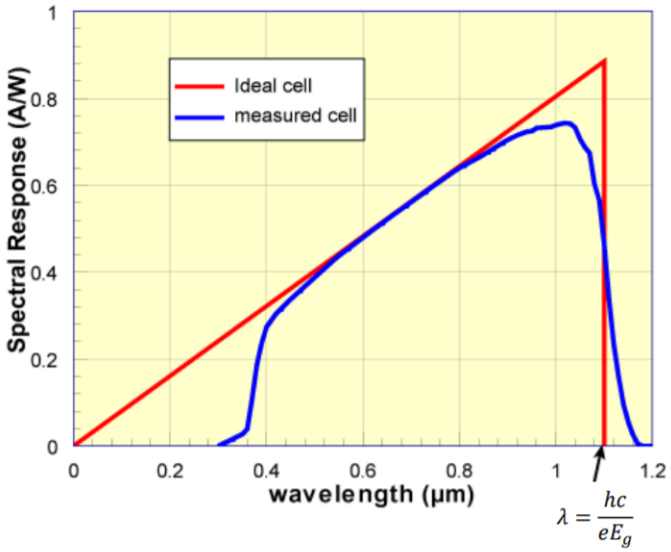

Figure 3.2.1: Spectral response [19]

The choice of semiconductor used determines E_g. It is a compromise between the desire to use the energy from photons at wavelengths in the broadest range possible and the wish to keep an efficiency that is sufficient at wavelengths below the cutoff wavelength.

Crystalline silicon (with $E_g \approx 1.12eV$) is widely used due to its interesting properties at a wide range of wavelengths. But crystalline silicon cells have an efficiency limit at 33% due to losses. It is also worth noting that the band gap E_g depends on the temperature because the spectral sensitivity varies along with it. So the current and power generated by a solar cell vary with the temperature, as shown in figure 3.2.2. For a crystalline silicon cell, the equation linking the band gap to temperature is $E_g = 1.16 - 7.0210^{-4} \cdot \frac{T^2}{T+1108}$.

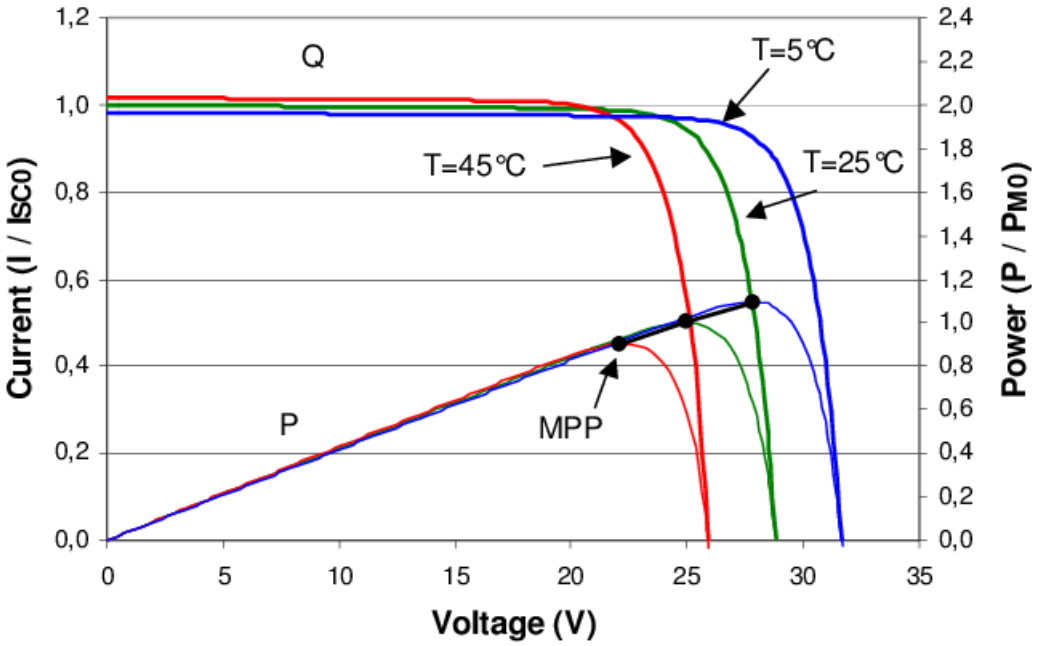

Figure 3.2.2: I/V and P/V curves of a solar cell for various temperatures [41]

3.2.1 PV cells modeling

The characteristic curves of an Si-diode and an Si solar cell can be seen in figure 3.2.3. When the solar cell is in the dark, it has the characteristics of a diode. When illuminated, the electrical characteristics of the cell shift downwards, with a shift proportional to the illumination level. A negative current is created by the diode, but the electrical characteristics are flipped for convention. I_{sc} is the short-circuit current and V_{oc} the open circuit voltage. The largest product of current and voltage is the point of interest where the largest power is generated, it is called the Maximum Power Point or MPP and MPPT or Maximum Power Point Tracking techniques are used to get it.

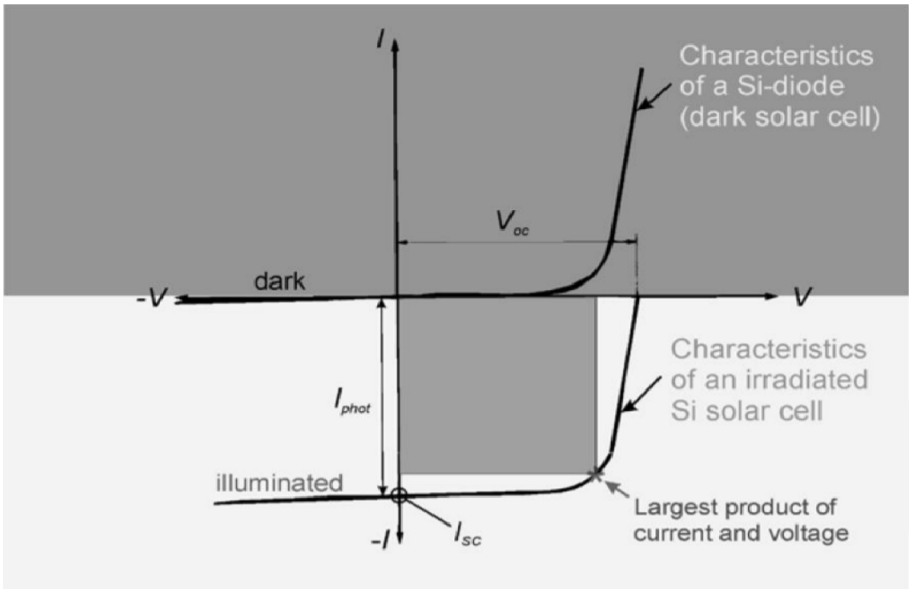

Figure 3.2.3: Electrical characteristics of a solar cell [1]

The electrical equivalent circuit of a photovoltaic cell can be seen in figure 3.2.4. It is in the generator sign convention. The equation giving the current I is

$$I = I_P - I_{D0}\left(e^{\frac{q(V+R_S I)}{kT}} - 1\right) - \frac{V + R_S I}{R_{sh}} \tag{3.2.1}$$

R_S and R_{sh} are the parasitic resistances of the diode. k is the Boltzmann constant ($= 1.38 \cdot 10^{-23}$) and q is the charge of an electron ($= 1.62 \cdot 10^{-19}$).

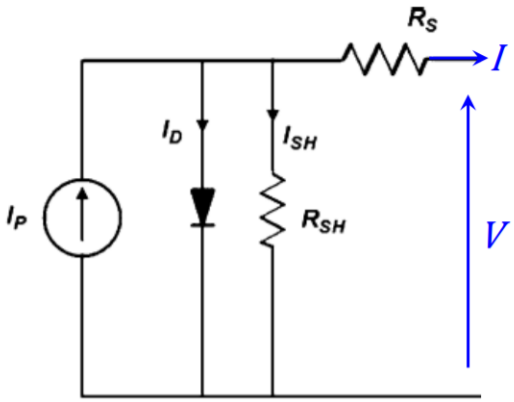

Figure 3.2.4: Electrical model of a solar cell [2]

[1] Graph issued from the slide of the course LENVI2007 - Renewable Energy Sources given at UCLouvain by P. Gerin, E. De Jaeger and H. Jeanmart

[2] See footnote 1

The I/V characteristic of a PV cell is used to show its current properties in function of the voltage. It can be seen in figure 3.2.5. The MPP, or Maximum Power Point, is the point of interest ($P_{MPP} = V_{MPP} \cdot I_{MPP}$). The MPP is reached when the load matches with the dynamic impedance of the source.

$$\frac{V_{MPP}}{I_{MPP}} = -\frac{\partial V_{MPP}}{\partial I_{MPP}} \tag{3.2.2}$$

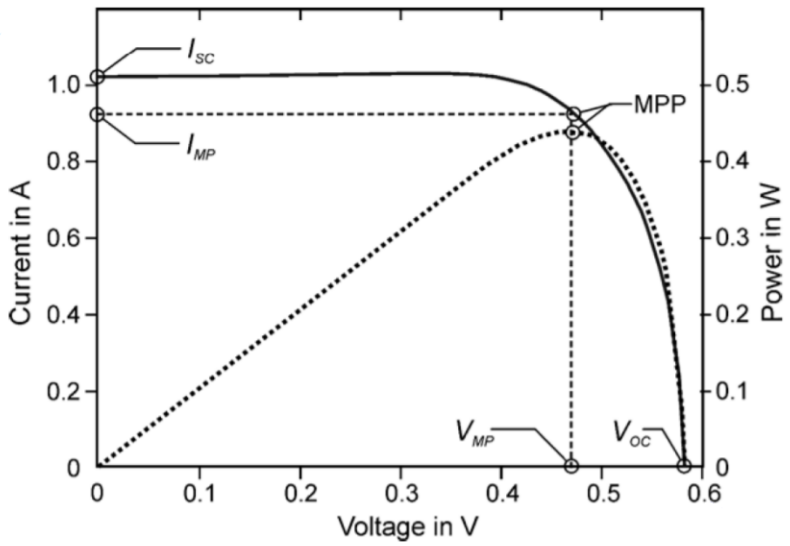

Figure 3.2.5: V-I characteristic of a PV cell [3]

The Fill-Factor (FF) is a measure of quality of the solar cell. It is calculated by comparing the maximum power to the theoretical power that would be output at both the open circuit voltage and short circuit current together.

$$FF = \frac{V_{MPP} I_{MPP}}{V_{oc} I_{sc}} \tag{3.2.3}$$

Both the open circuit voltage V_{oc} and the short circuit current I_{sc} depend on the band-gap (V_{oc} increases while I_{sc} decreases when the band gap increases). The theoretical maximum $V_{oc} I_{sc}$ is obtained for a 1,1 eV band-gap [39]. However, the efficiency of the solar cell is still limited by the Shocley-Queisser limit, which states the maximal theoretical efficiency of a solar cell using only one P-N junction, depending on the band gap. This limit is obtained by combining the different negative effects that can happen in a solar cell such as light reflection and recombination. The Shocley-Queisser limit is shown in figure 3.2.6.

[3] See footnote 1

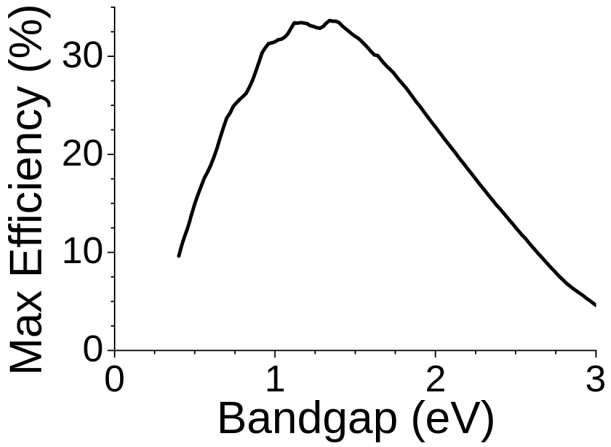

Figure 3.2.6: Maximum efficiency of a solar cell for various band gaps [50]

The I/V characteristic of a solar cell changes alongside the irradiance on the solar cell. The shift on the I/V characteristic is almost vertical, as seen in figure 3.2.7. When the illumination is not high, the power output is not proportional to the illumination and the module efficiency decreases. When the irradiance is equal to 0, the solar cell characteristics are the same as one of a diode. As there is a link between irradiance and temperature, it could be used to control the system to work at the Maximum Power Point. However, this is difficult because the relation between irradiance and temperature is non-linear.

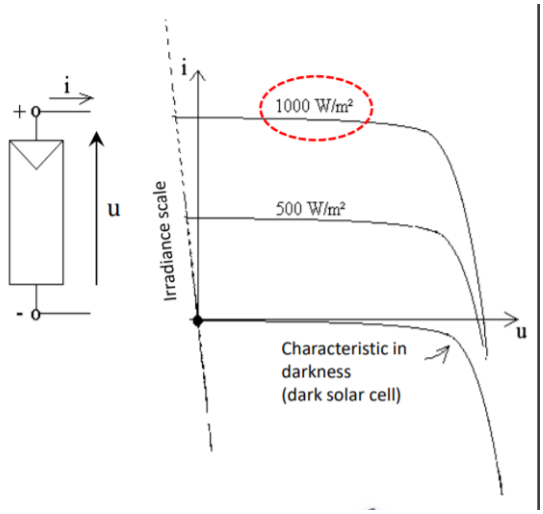

Figure 3.2.7: V-I characteristic of a PV cell for different irradiance levels [29]

The solar cells in a solar panel can be connected in series or in parallel. When similar cells are connected in series, the voltage is multiplied by the number of cells for each value of the current. Contrarily, when similar cells are connected in parallel, it is the current that is multiplied by the number of cells for each values of the voltage. In both cases, the number of cells multiplies the maximum power. A common method is to connect the cells in parallel branches of series-connected cells. The loss of a cell induces the loss of a branch. It is best used when each branch has its own MPPT.

3.3 PV modules advanced modeling

Two connected aspects have to be taken into account when modeling a photovoltaic cell or module. A complete model incorporates a photovoltaic- or light-model and an electrical model.

3.3.1 Light model

This model illustrates the conversion of the energy in the sunlight to photovoltaic current. It is possible to consider that the current generated from the absorption of photons by the material and the irradiance are proportional, if the spectral content remains unchanged

$$I_L = \frac{I_{LN}}{I_{rN}} I_r \tag{3.3.1}$$

with I_{rN} a standard irradiance level of 1000 W/m^2, I_L the photo-generated current and I_r the irradiance on the module (in W/m^2). But, as seen in figure 3.2.1, the spectral response is not constant below the cut-off wavelength $\lambda = \frac{hc}{eE_g}$. Therefore, the actual sensitivity of a solar module is lower than the ideal spectral sensitivity, and it also depends on the temperature, as seen in figure 3.2.2. But the current is only slightly affected by temperature changes. A linear approximation can therefore be used:

$$I_L = \frac{I_{LN}}{I_{rN}} I_r[1 + \mu(T_{junc} - T_{ref})] \tag{3.3.2}$$

With μ a parameter depending on the material used for the solar cell and the spectrum, given in $\%/°C$.

3.3.2 Electrical model

The general equivalent circuit contains a non-linear element that models a number of phenomena that redirect some part of the current generated by the absorption of photons. One or more non-ideal diodes can be used to represent these phenomena, as seen in figure 3.3.1. This induces exponentials in the model equation 3.3.3.

The first diode, and therefore the first exponential, has a factor γ_1 accounts for carrier recombinations, as stated in the Shockley ideal diode equation [39]. Without particular solar concentration, the recombination is limited by the minority carrier and the diode can be considered ideal, so $\gamma_1 = 1$. The two different types of carriers restrict recombination under conditions of high light concentration, and $\gamma_1 = 2$. The second diode represents the presence of defects. Defects create

intermediate energy levels in the forbidden band, and as a result carriers recombine in the depletion zone. γ_2 is usually comprised between 1 and 4, and is equal to 2 if the defects are uniformly distributed. When the injection of photon is very large, Auger recombinations can happen. An Auger recombination happens when a majority carrier and a minority carrier are combined by sending the energy generated by the recombination to another majority carrier. An additional exponential term is added to the model with $\gamma_3 = 2/3$. The general equivalent circuit equation is

$$I = I_L - I_1\left(e^{\frac{e(V+R_sI)}{\gamma_1 kT}} - 1\right) - I_2\left(e^{\frac{e(V+R_sI)}{\gamma_2 kT}} - 1\right) - ... - \frac{1}{R_{sh}}(V + R_sI) \tag{3.3.3}$$

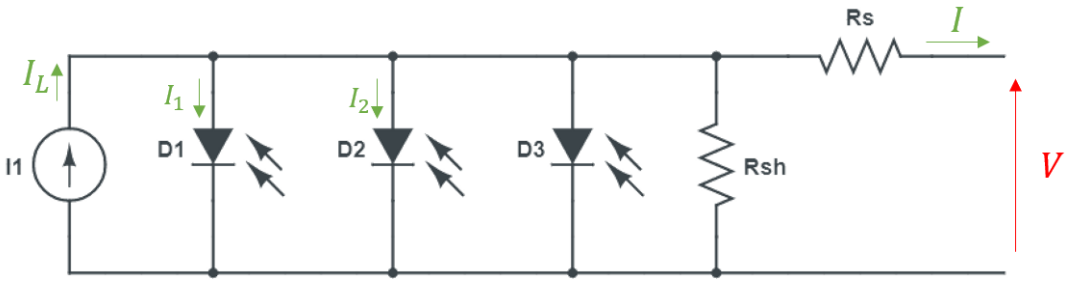

Figure 3.3.1: General equivalent circuit

The general equivalent circuit is however quite complicated and needs a great number of experimental results to be fully characterized. If these results are not available, a simpler model, the standard model, can be used to model the solar cell.

The standard model for PV cells is made of one diode and two resistances. The coefficient γ of the diode is an intermediate value related to the various coefficients γ_i of the complete reference model seen previously. The standard electrical model can be seen in figure 3.3.2.

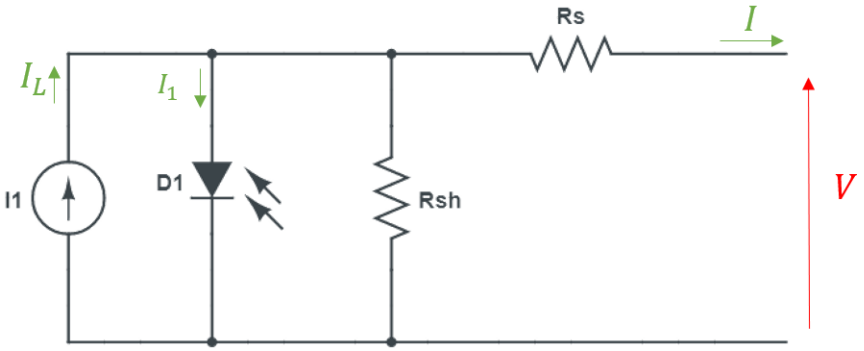

Figure 3.3.2: Standard solar cell model

To characterize a solar cell, the values of $I_L, I_1, \gamma, R_{sh} and R_s$ have to be identified. For crystalline silicon cells, it is possible to start by choosing an upper bound for a realistic value for R_s. It can be chosen such that

$$0 \leq R_S \leq \frac{V_{oc} - V_{MPP}}{I_{MPP}} \tag{3.3.4}$$

With V_{oc} the open circuit voltage, and V_{MPP} and I_{MPP} the voltage and current at the Maximum Power Point, respectively. Still, four parameters remain to be found to solve the model equation 3.3.5

$$I = I_L - I_1 \left(e^{\frac{e(V+R_s I)}{\gamma k T}} - 1 \right) - \frac{1}{R_{sh}}(V + R_s I) \tag{3.3.5}$$

The standard data given by the manufacturers of the solar cell for reference irradiance and temperature are usually the open-circuit voltage V_{oc}, the maximum power point V_{MPP} and I_{MPP} and the short-circuit current I_{sc}.

A fourth value is necessary to solve the system to obtain the parameters of the solar cell. It is obtained by expressing the fact that the power is maximum at the MPP. This leads to equation 3.3.6

$$\frac{dP}{dV}|_{MPP} = I_{MPP} + V_{MPP}\frac{dI}{dV}|_{MPP} = 0 \tag{3.3.6}$$

So, I_L, I_0, γ and R_{sh} can then be calculated for different values of R_S. An appropriate value of R_S has to be chosen with the four remaining parameter all positives.

3.4 MPPT

As explained earlier, the MPP is the point on the I/V curve where a maximal power output is reached. This point is characterized by a maximal power point current I_{MPP} and a maximal power point voltage V_{MPP}. MPPT or Maximum Power Point Tracking is a set of different techniques used to locate the MPP in variable conditions, and set the load characteristic so that the output is at this MPP. In the case of a contactless power transfer, the load characteristic is found only after the contactless part of the system. So the power electronics and the contactless power transfer influence the I/V curve of the transformer, and the MPP is moved because of the losses generated by the power electronics and the contactless coupling element. These losses might not be the same for every load characteristics, so the new MPP's voltage and current can not be predicted in advance. So the MPPT technique has to be implemented on the static part of the system, in the satellite, where the load is. Actually, the MPPT does not realize that there is a whole system

connecting the solar panel to the load, as the I/V curve is transposed from the solar panel to the load via the power electronics and the contactless power transfer element. The new I/V curve at the load is compatible with MPPT techniques, and is therefore used. In a sense, the I/V curve at the load might be interpreted as characterizing a "new" solar panel, similar to the actual solar panel.

Multiple MPPT techniques have been compared in [40]. From this comparison, it results that Perturb & Observe techniques have the smallest response time. Perturb & Observe techniques (P&O) use perturbations (increase or decrease) of the voltage of the solar panel and comparisons of the new obtained power with previous power points to reach the MPP. In the case of a contactless power transfer, it is the voltage of the load that will be perturbed. The direction of the perturbation is made in accordance with the direction of change in power output. If the power increases after the perturbation, then the next perturbation will go in the same direction. And if the power decreases, then the next perturbation will go in the opposite direction. These techniques have a great advantage in the case of wireless power transfer that the characteristics of the solar panel do not have to be known in advance [39]. Since the characteristic of the equivalent solar panel made from the transposition of the characteristic of the actual solar panel to the load via the system can not be determined in advance, these P&O techniques suit the system. However, the operating point will oscillate around the MPP in steady-state due to the nature of the perturbations, and that will cause losses. This drawback can be removed by using a variable perturbation [14] or by using the Three-Point Weighted technique, which compares the obtained power points with 3 other points obtained on the P/V curve [20].

3.5 Design of the solar panels

3.5.1 Solar cell model

The solar cells used for this application are Triple-Junction Solar Cell for Space Applications (CTJ30) from CESI S.p.A. The datasheet of the solar cells can be found in appendix A. Triple-Junction solar cells are multi-junction solar cells, which are cells with multiple P-N junctions each made of different materials. The different materials will react to photons of different wavelength, allowing for an absorption of photons in a wider range of wavelengths. The CTJ30 solar cells are made of InGaP, GaAs and Ge P-N junctions, which allows an absorption of light with wavelengths going from 300 to 1700nm.

The datasheet gives a typical current-voltage curves for the cells and the following parameters: the short-circuit current I_{sc}, the open-circuit voltage V_{oc}, and the current and voltage at the MPP I_{MPP} and V_{MPP}, as well as the power at the MPP P_{MPP}. The values of these parameters can be seen in table 3.1.

Parameters	I_{sc} (A)	V_{oc} (V)	I_{MPP} (A)	V_{MPP} (V)	P_{MPP} (W)
Values	0.473	2.6	0.455	2.32	1.05

Table 3.1: Parameters of the solar cell given by the datasheet

To model the solar cell in LTSpice, the parameters of the electrical model of the cell have to

be found. These are the light current I_L, the saturation current of the diode I_s, the ideality factor or emission coefficient of the diode γ, the parasitic series and parallel resistances R_s and R_{sh}. All these parameters are computed for a temperature $T = 25°C$.

By replacing the parameters given in the datasheet in equation 3.3.5, we obtain the following system of three equations

$$\begin{cases} I_{sc} = I_L - I_0 \cdot \left[exp\left(\frac{q(R_s I_{sc})}{\gamma k T}\right) - 1 \right] - \frac{1}{R_{sh}} R_s I_{sc} \\ 0 = I_L - I_0 \cdot \left[exp\left(\frac{q V_{oc}}{\gamma k T}\right) - 1 \right] - \frac{1}{R_{sh}} V_{oc} \\ I_{MPP} = I_L - I_0 \cdot \left[exp\left(\frac{q(R_s I_{MPP} + V_{MPP})}{\gamma k T}\right) - 1 \right] - \frac{1}{R_{sh}} (R_s I_{MPP} + V_{MPP}) \end{cases} \tag{3.5.1}$$

However, the system only has 3 equations for 4 unknowns. A fourth equation is obtained by expressing the fact the the power is maximum at the MPP as in equation 3.3.6. The system is still very difficult to resolve, as it is composed of 4 non-linear equations. A way to resolve the system easily with simplifications is presented in [21]. The first simplification consists of neglecting the impact of R_s and R_{sh}. So, by setting $R_s \approx 0$ and $\frac{1}{R_{sh}} \approx 0$, the first equation becomes

$$\begin{aligned} I_{sc} &= I_L - I_0 \cdot \left[exp\left(\frac{q \cdot 0}{\gamma k T}\right) - 1 \right] - 0 \\ \Rightarrow I_L &\approx I_{sc} \end{aligned} \tag{3.5.2}$$

Using equations 3.3.5 and 3.3.6, the ideality factor can be obtained with the equation

$$\gamma = \frac{q \cdot (2V_{MPP} - V_{oc})}{kT \left[\frac{I_{MPP}}{I_{sc} - I_{MPP}} + ln\left(1 - \frac{I_{MPP}}{I_{sc}}\right) \right]} \tag{3.5.3}$$

Which yields $\gamma = 3.604$. The saturation current is obtained with the second equation of the system, simplified to neglect the impact of the parallel resistance R_{sh}

$$I_s = I_L \cdot exp\left(\frac{-q V_{oc}}{\gamma k T}\right) \tag{3.5.4}$$

And its value is $I_s = 3.1 \cdot 10^{-13}$A. Now, equation 3.3.5 can be expressed as

$$I = I_{sc}\left[1 - exp\left(q\frac{V - V_{oc} + IR_s}{\gamma kT}\right)\right] \tag{3.5.5}$$

And by replacing I and V by the values of the current and the voltage at the MPP this equation becomes

$$I_{MPP} = I_{sc}\left[1 - exp\left(q\frac{V_{MPP} - V_{oc} + I_{MPP}R_s}{\gamma kT}\right)\right] \tag{3.5.6}$$

The series resistance R_s can now be computed thanks to this last equation. It gives

$$R_s = \frac{\frac{\gamma kT}{q}ln\left(1 - \frac{I_{MPP}}{I_{sc}}\right) + V_{oc} - V_{MPP}}{I_{MPP}} \tag{3.5.7}$$

Which gives $R_s = 0.0504\Omega$. The last parameter to be computed is the parallel resistance R_{sh}, which is obtained with the third equation of the system in 3.5.1

$$\frac{1}{R_{sh}} = \frac{I_{MPP} - I_L - I_0 \cdot \left[exp\left(\frac{q(R_s I_{MPP} + V_{MPP})}{\gamma kT}\right) - 1\right]}{R_s I_{MPP} + V_{MPP}} \tag{3.5.8}$$

This final equation gives $R_{sh} = 203.72\Omega$. The five parameters of the electrical model of the PV cell that have been computed are summarized in table 3.2.

Parameters	I_L (A)	I_0 (A)	γ	R_s (Ω)	R_{sh} (Ω)
Values	0.473	$3.1 \cdot 10^{-13}$	3.604	0.0504	203.72

Table 3.2: Computed parameters of the electrical model of the CTJ30 solar cell

The solar cell with these parameter is simulated in LTSpice from the model shown in figure 3.5.1. The diode parameters I_s and N correspond to the saturation current and the ideality factor, respectively. The current-voltage and power-voltage curves of the simulated solar cell are shown in figure 3.5.2a and compared with the curves provided by the CTJ30 datasheet in figure 3.5.2b.

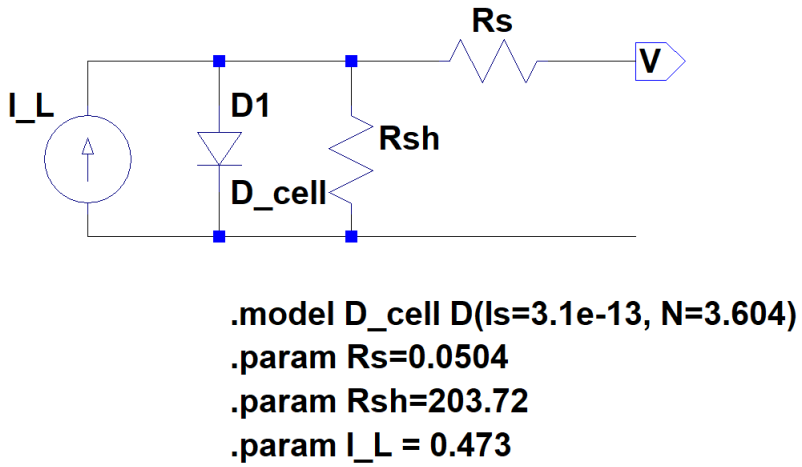

Figure 3.5.1: LTSpice model of the CTJ30 solar cell

The simulated solar cell I/V and P/V curves are similar, although not exactly the same. The simulated solar cell has a maximum power of 1.013 W, for 1.05 W for the actual cell. The Maximum Power Point is not at the same voltage level, 2.29 V for the simulated cell and 2.32 V for the actual cell. The differences are not enormous, and so the simulated cell can be considered as behaving like the actual cell. These cells now have to be put together in series inside parallel branches to form a solar panel capable of outputting the desired power for the application at the MPP.

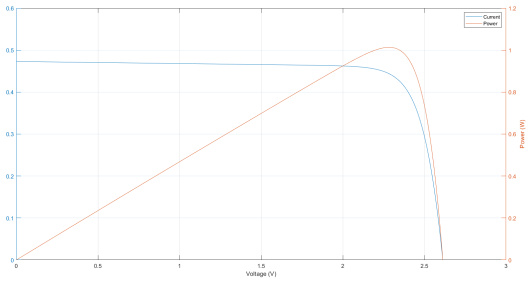

(a) I/V and P/V curves of the simulated solar cell (at 25°C)

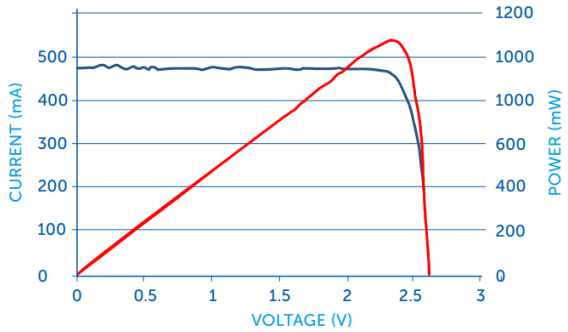

(b) Curves of the solar cell provided in the datasheet

Figure 3.5.2: Comparison of the I/V and P/V curves of the simulated and actual solar cells

3.5.2 Solar panel model

As the magnetic coupling element needs to transfer 5 kW of power at a maximum of 150 V, the power at the MPP of the solar array needs to be greater than 5 kW to account for the losses in the magnetic coupling element and in the power electronics converters. The solar panels are simulated using LTSpice, and are composed of solar cells CTJ30 simulated with the electrical parameters presented previously and with the model shown in figure 3.5.1.

Starting from the open-circuit voltage of a single cell V_{oc}, the number of cells to be put in series is obtained. As putting cells in series multiplies the voltage for any value of the current, and knowing that the maximum voltage, or the open-circuit voltage, of the panel must be 150 V, the number of cells to be put in series is obtained by dividing the open-circuit voltage of the panel by the open-circuit voltage of one cell, which gives $\frac{V_{oc,panel}}{V_{oc,cell}} = \frac{150}{2.6} \approx 58$ cells in series. Now, the number of parallel branches is obtained with the MPP. The desired MPP will be found at a voltage which is obtained by multiplying the MPP voltage of one single cell by the number of cells in series, so $58 \cdot V_{MPP} = 134.56V$. As the desired power at the MPP is superior to 5 kW, it can be set to 5.5 kW to account for a 90% efficiency of the power electronics and the transformer. The current at the MPP will be $\frac{5500}{134.56} = 40.87A$, and by dividing this current by the current at the MPP for one single cell, the number of parallel branches is obtained $\frac{40.87}{0.455} \approx 90$.

The model used and its symbol are shown in figure 3.5.3. The parameter **n** multiplies the output voltage of the cell for any given current. As seen earlier, this is equivalent to setting a number **n** of solar cells in series inside each parallel branches of the PV panel. The parameter **p** multiplies the current of the cell for any given voltage, which is equivalent to setting a number **p** of parallel branches of **n** series connected solar cells. The parameters **n** and **p** are set to 58 and 90 respectively.

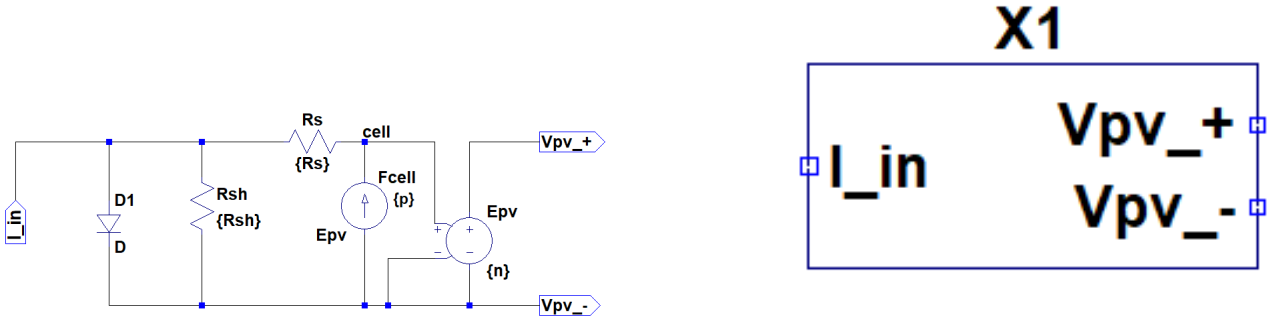

(a) Model of the PV panel

(b) Symbol modelling the solar panel

Figure 3.5.3: Model and symbol of the PV panel

The obtained I/V and P/V curves of the resulting solar panel can be seen in figure 3.5.4. The simulated solar panel issues 5.5 kW of power at the MPP, which is situated at 134V, as expected. The total number of solar cells is 5220, and as each CTJ30 solar cell has an area of $26.5cm^2$ as per the datasheet, the total area of a solar panel is $13.8m^2$.

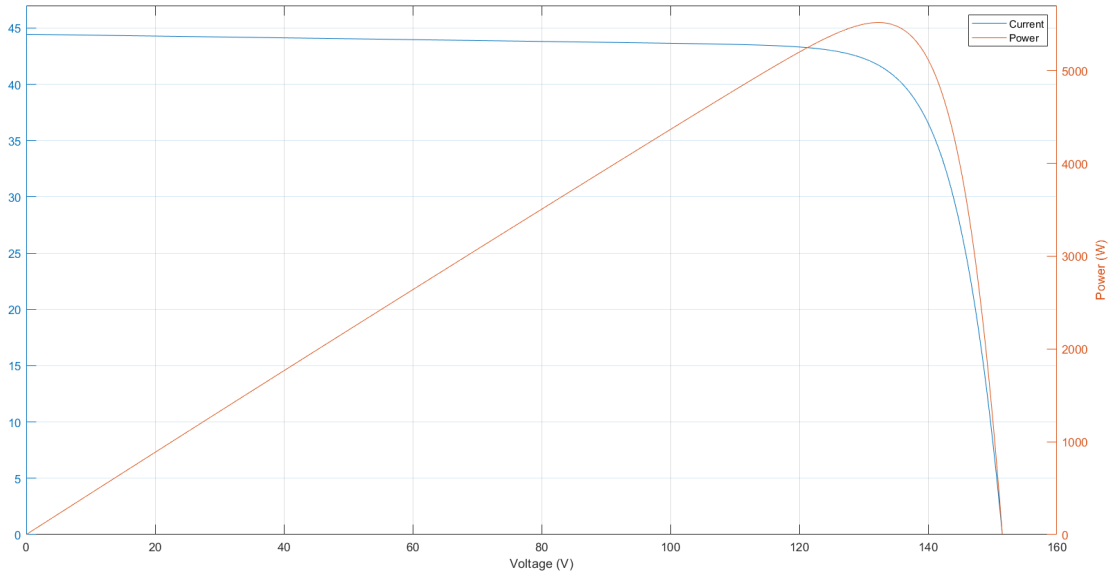

Figure 3.5.4: I/V and P/V curves of the simulated solar panel

Chapter 4

Magnetic Coupling Element : Transformer

This chapter aims at presenting and explaining the theory and the design process behind the magnetic coupling element used in the system. First, a comparison of the different topologies presented in section 2.4 is made in order to chose the most adequate topology for the magnetic coupling element. Then, each different characteristics of the chosen magnetic coupling element are explained with different models. All these model will be used to optimize the resulting magnetic coupling element, so that it has minimal losses and a maximal power density. The electrical model of the resulting magnetic element is used in the simulation of the complete system.

4.1 Selection of the topology

As multiple topologies have been presented in chapter 2, it is important to chose the topology that will best suit the system. The Qi reference with only a primary coil is not suited for the system, as the primary and the secondary need to be aligned to have a maximum transfer output. The geometry of the system requires that the transferred power is the same, not matter the position of the primary with regards to the secondary. Multiple primaries, secondaries, or a cascaded transformer are not needed. The solar panel needs to always be perpendicular to the irradiation coming from the sun, so the magnetic coupling element needs to be a rotating transformer. As a large shaft diameter is not needed and as a high power transfer is required, the rotating transformer presented in [5] is not retained. The pot core geometry is interesting as it has less core and winding losses [43] than the axial rotating geometry, and as it can be used to make a rotating transformer. A pot core geometry will be used for the transformer used in the system to transfer power from the solar panel to the satellite without contact. This rotating transformer will replace the systems with slip rings that are victim to wear and are voltage limited.

4.2 Geometry of the Transformer

The magnetic coupling element used is a transformer designed in [9] by T. Deceuleneer. It is a transformer with a pot core geometry, capable of transferring up to 10 kW of power. The transformer used for the system has a pot core geometry, with coaxial windings. This geometry

and winding direction have been chosen to minimize the air gap length and the winding losses (chapter 4.6). The air gaps are located on top of the windings, to maximize the interface area between each winding and its associated magnetic core [9]. Figure 4.2.1 shows the complete geometry and dimensions of the transformer.

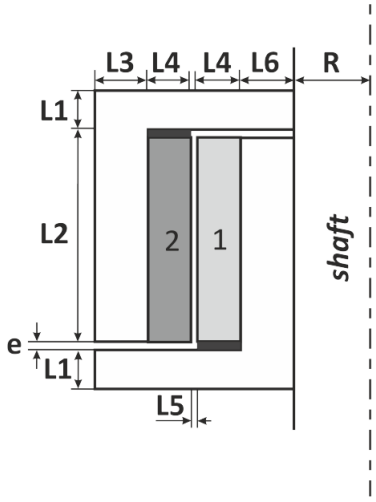

Figure 4.2.1: Geometry and dimensions of the transformer

4.3 Equivalent Electrical Circuit

The equivalent electrical circuit of a transformer is shown in figure 4.3.1. The inductances $L_{f,1}$, $L_{f,2}$ and L_μ represent the primary and secondary leakage inductances (which are used to model the leakage flux) and the magnetizing inductance, respectively. The resistances R_1, R_2 and R_{ml} represent the losses in the primary and secondary windings, and the losses in the magnetic core, respectively. n_1 and n_2 are the number of turns that the primary and secondary windings have. The transformer turn ratio is expressed as

$$N = \frac{n_1}{n_2} = \frac{V_1}{V_2} = \frac{I_{out}}{I_{in} - I_\mu} \tag{4.3.1}$$

It is worth noting that the current in the very large resistance R_{ml} is not taken into account in equation 4.3.1 as it is very small. Equation 4.3.1 shows that the magnetizing current I_μ is generating losses, and so it is important to reduce it. The losses in the transformer are generated in the windings and in the core. These are explained in 4.5 and 4.6. The effects of the leakage and magnetizing inductances are explained in 4.4.

4.4 Magnetic Circuit Modelling

The transformer used in the system has a core made of a magnetic material. This core is used to focus the magnetic flux, direct it through the windings, and lower leakage flux. The use of a

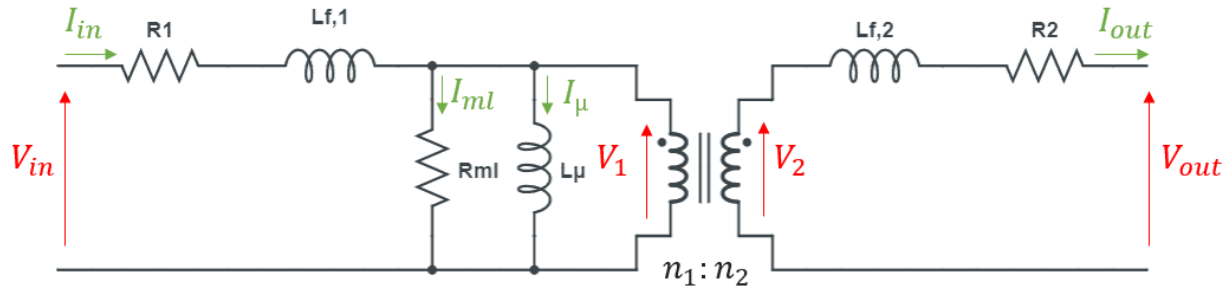

Figure 4.3.1: Equivalent electrical circuit of a real transformer

magnetic core impacts the values of the leakage and magnetizing inductances, and this impact is studied in 4.4.1 and 4.4.2.

4.4.1 B-H Curve

When considering winding induction, the voltage that induces a magnetic flux ϕ is called the induction voltage and has an amplitude given by

$$v = \frac{d\phi(t)}{dt} \tag{4.4.1}$$

As the windings are composed of N turns in series, a factor N multiplies the second part of equation 4.4.1. As the magnetic flux links the windings with their surface area, it can be expressed as

$$\phi = \int_A \mathbf{B}\, dA \tag{4.4.2}$$

Where A is the surface area of the windings and $\mathbf{B}$ is the magnetic flux density. From equations 4.4.1 and 4.4.2, with windings made of N turns and considering the cross section's magnetic flux distribution to be uniform, the magnetic flux density can be expressed as

$$\mathbf{B}(t) = \frac{N}{A} \int v\, dt \tag{4.4.3}$$

To characterize a magnetic material, the magnetic flux density can be associated with the magnetizing field **H**. This magnetizing field can be determined with Ampere's law. It states that the total magnetomotive force around a closed path is equal to the current passing through its inner area

$$\oint_{l_p} \mathbf{H}\, dl = \int_{S_p} J\, dA \tag{4.4.4}$$

With l_p the length of the path, S_p the inner area, and J the current density. If this current density is assumed constant, and the path assumed separated from the outer region by a material, equation 4.4.4 can be simplified into

$$\sum_j \mathbf{H}_j \cdot l_j = n \cdot i \tag{4.4.5}$$

So the magnetizing field is related to the magnetic flux density with

$$\mathbf{B} = \mu_0 \mu_r \mathbf{H} \tag{4.4.6}$$

Where μ_0 and μ_r are the permeability of the vacuum and the relative permeability of the material. The B-H curves of air and of a magnetic material can be seen in figure 4.4.1. The magnetizing energy needed to transfer power from the primary windings of the transformer to the secondary windings needs to be minimum. It can not be 0 otherwise there would be no voltage. The magnetizing energy is minimized when a material with a high relative permeability is used.

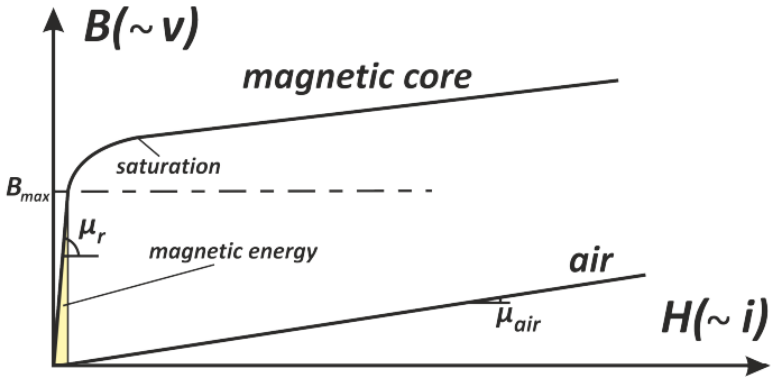

Figure 4.4.1: B-H curves of transformers with a magnetic core and with air

4.4.2 Reluctance Model

The reluctance model permits to do an analogy between the equivalent magnetic circuit of the transformer and an electric circuit. The idea is to make an equivalence between the magnetic flux density and the current density, and between the magnetizing field with the electric field. Other equivalences are then obtained from these equivalences and the equations governing electrical systems. The voltage, which is a difference of potential between 2 points in an electric field, is obtained with $V = \int_{P_a}^{P_b} E dl$ and has as equivalent value the magnetomotive force (MMF), which is thus given by $MMF = \int_{P_a}^{P_b} H\, dl$, as H is equivalent to E as stated earlier. The current has as equivalent value the magnetic flux, as stated in equation 4.4.2, as B and J are equivalent. Finally, Hopkinson's law is used to compute the MMF in a magnetic circuit. It is equivalent to Ohm's law in an electric circuit

$$\mathcal{F} = \mathcal{R} \cdot \phi \tag{4.4.7}$$

Where $\mathcal{R}$ is the reluctance, which represents the opposition to magnetic flux. It is equivalent to the electrical resistance and it depends on the geometry and structure of a material. The expression of the reluctance depends on the direction of the magnetic flux, which is either axial or radial

$$\mathcal{R}_{axial} = \frac{l}{\mu A} \tag{4.4.8}$$

With l then length of the magnetic circuit, $\mu = \mu_0 \mu_r$ and A the cross-sectional area of the circuit. For a radial flux

$$\mathcal{R}_{radial} = \frac{1}{\mu \alpha l} ln\left(\frac{b}{a}\right) \tag{4.4.9}$$

With a and b the inner and outer radii of the air gap, and α the angular opening, equal to 2π. These expressions stand for an uniform flux.

As the inductance is linked to the magnetic flux with $L = \frac{\Phi}{i}$, the inductance can be expressed with the reluctance because $\Phi = n \cdot \phi$ and $i = \frac{\mathcal{F}}{n}$ so

$$L = \frac{n \cdot \phi}{\mathcal{F} \cdot n^{-1}} = \frac{n^2}{\mathcal{R}} \tag{4.4.10}$$

The value of the inductances used to model the transformer can then be obtained by computing the reluctance of the transformer, which can be obtained from the transformer's geometry and material.

4.4.3 Magnetizing inductance

When transferring energy with a transformer, a part of this energy is stored in the core of the transformer, and magnetizes it. This is the magnetizing energy, or magnetizing current. This magnetizing energy is represented in the transformer equivalent electrical circuit by a magnetizing inductance. It was stated earlier that the magnetizing energy had to be low, among other things because the magnetizing current contributes to losses. So the magnetizing inductance needs to be high. The magnetizing inductance can be sized thanks to the reluctance model and the geometry of the transformer. The reluctance network is composed of 6 reluctances, 4 corresponding to the horizontal and vertical plates of the transformer, and 2 corresponding to the air gaps. The MMF sources correspond to the windings. The reluctance circuit can be seen in figure 4.4.2.

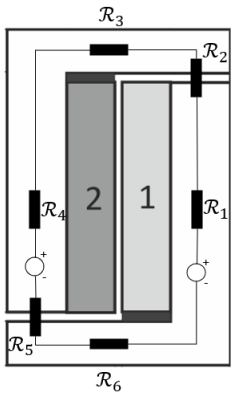

Figure 4.4.2: Reluctance network for the magnetizing inductance

The total reluctance corresponds to the sum of each reluctance. They can be computed with the dimensions of the transformer, and equations 4.4.8 for reluctances 1, 2, 4 and 5 and 4.4.9 for reluctances 3 and 6, which gives

$$\begin{aligned} \mathcal{R}_1 = \mathcal{R}_4 &= \frac{L_2}{\mu\pi[(L_6+R)^2 - R^2]} \\ \mathcal{R}_2 = \mathcal{R}_5 &= \frac{e}{\mu_0\pi[(L_6+R)^2 - R^2]} \\ \mathcal{R}_3 = \mathcal{R}_6 &= \frac{1}{\mu\, 2\pi L_1} ln\left(\frac{R_o/2}{R}\right) \end{aligned} \tag{4.4.11}$$

And so, from equation 4.4.10 comes

$$L_\mu = \frac{n^2}{\sum_i \mathcal{R}_i} \tag{4.4.12}$$

With $\mathcal{R}_i$ the reluctances from 1 to 6, and n the number of turn. For the magnetizing inductance to be large, the number of turn needs to be high and the total reluctance needs to be minimal. The equivalent reluctances of the air gaps $\mathcal{R}_2$ and $\mathcal{R}_5$ do not depend on the relative permeability of the material μ_r, so they are the dominant reluctances. The air gaps need then to be as small as possible in order to have a large magnetizing inductance and small magnetizing energy.

4.4.4 Leakage inductance

The reluctance model can also be used to evaluate the leakage inductance, which is an inductance representing the leakage flux. The leakage flux is a part of the flux generated by the windings which is flowing through the window of the transformer. The leakage flux generates no voltage at the secondary and is thus only responsible of losses. However, whereas the MMF was considered uniform for the evaluation of the magnetizing inductance, the MMF is now varying with radial position. Figure 4.4.3 shows the equivalent reluctance network linked with the leakage flux.

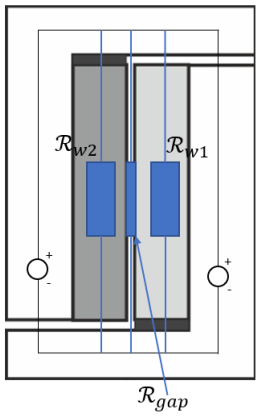

Figure 4.4.3: Reluctance network for the leakage inductance

The expression of the reluctance in the air gap $\mathcal{R}_{gap}$ is simply derived from equation 4.4.8 and the geometry of the transformer as the MMF in the air gap is uniform

$$\mathcal{R}_{gap} = \frac{L_2}{\mu_0 \, \pi[(R + L_4 + L_5 + L_6)^2 - (R + L_4 + L_6)^2]} \tag{4.4.13}$$

But the reluctances of the windings $\mathcal{R}_{w1}$ and $\mathcal{R}_{w2}$ can not be computed this way as the MMF is not uniform, but is linear over the windings. It increases linearly from left to right across the primary winding, and decreases linearly from left to right across the secondary winding. The reluctances with linear MMF are the same as the reluctance with uniform MMF multiplied by a factor 3. The winding reluctances are therefore given by

$$\begin{aligned} \mathcal{R}_{w1} &= \frac{3L_2}{\mu_0 \, \pi[(R + L_4 + L_6)^2 - (R + L_6)^2]} \\ \mathcal{R}_{w2} &= \frac{3L_2}{\mu_0 \, \pi[(R + 2L_4 + L_5 + L_6)^2 - (R + L_4 + L_5 + L_6)^2]} \end{aligned} \tag{4.4.14}$$

Computing the parallel connection of reluctances $\mathcal{R}_{gap}$, $\mathcal{R}_{w1}$ and $\mathcal{R}_{w2}$ gives the total leakage inductance

$$L_f = \frac{n^2}{\left(\frac{1}{\mathcal{R}_{gap}} + \frac{1}{\mathcal{R}_{w1}} + \frac{1}{\mathcal{R}_{w2}}\right)^{-1}} \tag{4.4.15}$$

And the leakage inductances corresponding to the primary and the secondary side of the transformer are

$$\begin{aligned} L_{f,1} &= \frac{n^2}{\mathcal{R}_{w1}} \\ L_{f,2} &= \frac{n^2}{\left(\frac{1}{\mathcal{R}_{gap}} + \frac{1}{\mathcal{R}_{w2}}\right)^{-1}} \end{aligned} \tag{4.4.16}$$

4.5 Core Losses Modelling

Adding a magnetic core to the transformer increases and concentrates the magnetic flux linking the primary winding to the secondary windings, but it is also a source of losses. These losses result from the Eddy currents in the core material and the hysteresis effect. Eddy currents are currents appearing in the material to oppose the change of flux density in the material. These currents generate losses according to

$$P_{losses,Eddy} = \frac{\left(\frac{d\phi}{dt}\right)^2}{R_{core}} = k_{Eddy} \cdot f^2 \cdot \hat{B}^2 \cdot V \tag{4.5.1}$$

The hysteresis effect states that the magnetization of a ferromagnetic material, resulting from a varying magnetic field, lags behind the field. This implies that the B-H curve of a material is not the same for an increasing and a decreasing flux density. This can be seen in figure 4.5.1.

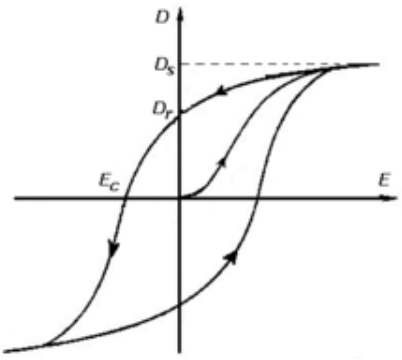

Figure 4.5.1: Hysteresis effect

The losses generated from the hysteresis effect can be expressed as

$$P_{losses,hysteresis} = k_{hysteresis} \cdot f \cdot \hat{B}^m \cdot V \tag{4.5.2}$$

In equations 4.5.1 and 4.5.2, V is the volume of the core, $\hat{B}$ is the peak value of the flux density, f is the frequency and k_{eddy}, $k_{hysteresis}$ and m are constants specific to the magnetic material used. Equations 4.5.1 and 4.5.2 can be combined to obtain the total power losses induced by the core

$$P_{losses,core} = k \cdot f^{\alpha} \cdot \hat{B}^{\beta} \tag{4.5.3}$$

Where k, α and β are material specific constants. Equation 4.5.3 is called the Steinmetz equation. However, this equation is only valid for a sinusoidal waveform in the transformer. In the case of the studied system, the waveform in the transformer is trapezoidal. An improved equation is made in [34]. For a trapezoidal waveform, it gives

$$P_{losses,core} = k \cdot f^{\alpha} \cdot \hat{B}^{\beta} \cdot 0.915 \cdot D^{1-\alpha} \tag{4.5.4}$$

Where D is the trapezoid duty cycle. The chosen core material is ferrite, because of its low losses generation. The values of the coefficient α for ferrite is 1.5, so equation 4.5.4 becomes

$$P_{losses,core} = k \cdot f^{1.5} \cdot \hat{B}^{\beta} \cdot 0.915 \cdot D^{-0.5} \tag{4.5.5}$$

The losses are then lower for a high duty-cycle. Finally, the resulting equivalent resistance is given by

$$R_{ml} = \frac{V_1^2}{P_{losses,core}} = \frac{V_1^2}{k \cdot f^{1.5} \cdot \hat{B}^{\beta} \cdot 0.915 \cdot D^{-0.5}} \tag{4.5.6}$$

4.6 Winding Losses Modelling

The windings are another source of loss that needs to be taken into account. The losses generated in the windings are copper losses. These losses have to be minimized because they are a great source of heat. To model these losses, the equivalent resistances of the windings are used. The DC-resistances of the primary and secondary windings are computed from the geometry of the windings

$$\begin{aligned} R_{DC,1} &= \frac{2\pi \cdot n^2 \cdot (R + 0.5L_4 + L_6)}{\sigma_{Cu} \cdot L_2 L_4 \cdot k_{f,winding}} \\ R_{DC,2} &= \frac{2\pi \cdot n^2 \cdot (R + 1.5L_4 + L_5 + L_6)}{\sigma_{Cu} \cdot L_2 L_4 \cdot k_{f,winding}} \quad = \end{aligned} \tag{4.6.1}$$

Where $k_{f,winding}$ is the fill-factor of the winding and σ_{Cu} is the electric conductivity of the copper (in $\Omega^{-1} \cdot m^{-1}$), which is itself dependant on the temperature with

$$\rho_{Cu} = 17 \cdot 10^{-8}(1 + 0.004(T - 20)) \tag{4.6.2}$$

Where T is the temperature in $°C$. The windings also have an equivalent AC-resistance, which is dependant on the frequency.

4.6.1 Skin Effect

The varying flux density inside of the conductor induce Eddy currents that change the distribution of the current. The current density is greater at the surface of the conductor than at the center of it. This is called the skin effect, it is characterized by the skin depth, which is the equivalent depth through which all of the current flows

$$\delta = \sqrt{\frac{\rho_{Cu}}{\pi \mu f}} \tag{4.6.3}$$

Equation 4.6.3 shows that the skin depth depends on the frequency of variation of the flux. It is smaller at high frequencies. The skin depth also depends on the resistivity of the copper ρ_{Cu} and the permeability of the copper $\mu = \mu_0 \mu_r$. The skin effect decreases the section of the wire in which the current flows, and thus increases the value of the equivalent AC-resistance and the losses. To avoid the skin effect, one might think about using wires made of strands with a cross section smaller than the skin depth multiplied by two, but the increase of strands negatively impacts the AC-resistance due to the proximity effect. Figure 4.6.1 shows the skin effect inside a conductor.

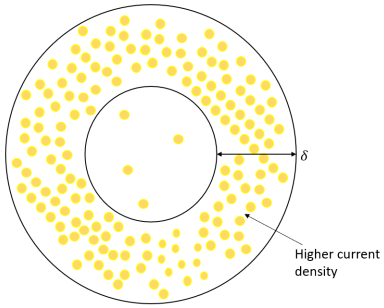

Figure 4.6.1: Skin effect inside a conductor

4.6.2 Proximity Effect

The proximity effect is an extension of the skin effect when wires with multiple layers or multiple strands are used. The varying flux density produces Eddy current in the strand, which is the cause of the skin effect. But similarly, the varying flux density will also induce Eddy current in the adjacent strands, with the current density in the adjacent strands pushed away from the initial strand. This reduces again the section of the strand in which the current flows, and once again increases the value of the equivalent AC-resistance. The Proximity effect is shown in figure 4.6.2. The proximity effect is amplified over each strand because of the smaller effective section of each strand. The proximity effect can be expressed with the Proximity factor, which is the ratio of the equivalent AC-resistance over the equivalent DC-resistance. The proximity factor is obtained with the Dowell's equation [42]

$$F_r = \Delta \left[\upsilon_1 + 2/3(m^2 - 1)\upsilon_2 \right] \tag{4.6.4}$$

With Δ the skin factor or penetration ratio equal to $\Delta = \sqrt{\frac{\pi}{4}} \frac{d}{\delta}$ with d the diameter of the conductor and δ the skin depth. m is the number of layers and υ_1 and υ_2 are given by

$$\begin{aligned} \upsilon_1 &= \frac{sinh\Delta - sin\Delta}{cosh\Delta + cos\Delta} \\ \upsilon_2 &= \frac{sinh2\Delta + sin2\Delta}{cosh2\Delta - cos2\Delta} \end{aligned} \tag{4.6.5}$$

So, the proximity factor decreases with the skin factor, which is itself inversely proportional with the frequency. Decreasing the the diameter d will also decrease the proximity effect, but for a same winding thickness the number of strands m will increase.

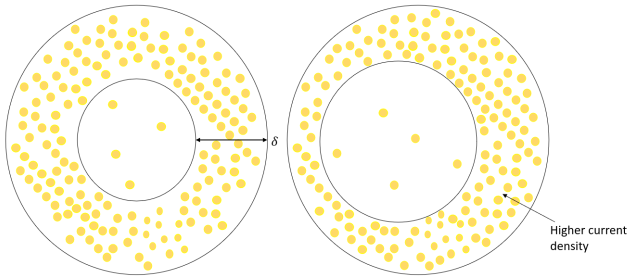

Figure 4.6.2: Proximity effect

4.7 Resulting Transformer

Thanks to the different models presented earlier, [9] has designed a transformer that will be used in the system. The design was made via a numerical optimization of 5 variables of the transformer, k_g, $\hat{J}$, n, f, and $\hat{B}$. These variables were chosen because they can represent the 8 physical dimensions of the geometry of the transformer, L_1 to L_6, R and e. For each variable, 10 values were considered in a predetermined range. The wires used for the transformer are composed of 840 strands with a diameter of $71\mu m$ (appendix C [9]), the core used is a ferrite 3C90 core made by Ferroxcube (appendix B [9]). The optimization results were compared for various frequencies on the losses that each resulting transformers produce and the power density (in W/kg) that they have. The dimension and electric properties of the resulting optimal transformer are shown in table 4.1. This transformer has been designed for a switching frequency of 40 kHz.

The corresponding equivalent electrical circuit of this transformer is obtained by applying the values of the electrical properties of the transformer on the circuit shown in figure 4.3.1. This is the circuit that will be used to model the transformer when simulating the system.

Transformer Dimensions		
Outer diameter	D_o (mm)	90
Height	H (mm)	86
Air gap length	e (mm)	0.1
Weight	M (kg)	2.2
Number of turns	N	9
Transformer electrical properties		
Magnetizing inductance	L_μ (μH)	450
Primary leakage inductance	$L_{f,1}$ (μH)	0.47
Secondary leakage inductance	$L_{f,2}$ (μH)	0.56
Core losses resistance	R_{ml} ($k\Omega$)	3
Primary winding resistance	R_1 ($m\Omega$)	5.18
Secondary winding resistance	R_2 ($m\Omega$)	6.84

Table 4.1: Dimensions and equivalent electrical properties of the transformer

Chapter 5

Power Electronics

The power electronic circuit used in the system is a Dual Active Bridge, or DAB. It is composed of a H-bridge before the primary coils of the transformer (figure 2.3.2), and an active rectifier after the secondary coil of the transformer (figure 2.3.6), presented in Chapter 2. The output signal is a DC signal with small oscillations. The DAB is a bidirectional device, meaning that it is able to transfer power both ways. But this characteristic of the circuit is not needed, as the goal is to send energy in one direction only, from the PV panel to the satellite. So a small change is made in order to reduce costs and the necessity of having two command systems. The active rectifier is replaced by a passive rectifier, diodes are used in place of controlled switches. The resulting schematic, showing the whole system, including the rotating and static part, can be seen in figure 5.0.1.

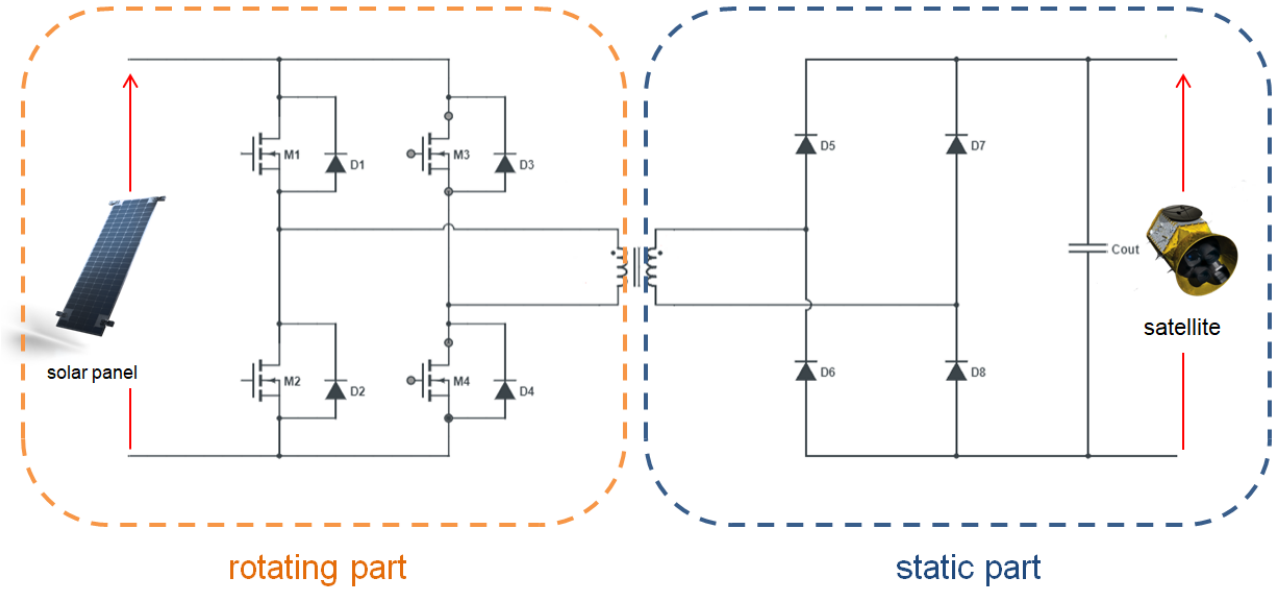

Figure 5.0.1: Schematic of the whole system

In this chapter, a small explanation will be made on the electronic switches. Then, three approaches for the DAB will be compared, namely a current-driven DAB, a voltage-driven DAB, and a voltage-driven Resonant DAB. The advantages and drawbacks of each topologies will be presented. The comparison will be motivated with the help of simulation results.

5.1 Switches

The characteristics of the switches in the H-bridge is to let current flow in both direction and no voltage difference at its terminals when it is closed (ON), and let close to no current flow and have a positive voltage difference at its terminal when it is open (OFF). This can be obtained with using a NMOS transistor as the switch. The NMOS lets current flow in both directions when it receives a voltage high enough at its Gate (ON), and lets no current flow when it is OFF. A 4-quadrant representation of the NMOS transistor is shown in figure 5.1.1. But as the load has inductive characteristics (from the transformer), a negative current might want to flow through the switch when it is open. This leads to over-current and can be harmful to the system if not taken care of. The solution is to add a diode in parallel with the NMOS transistor, to provide a path for the current to flow through. The resulting switch can be seen in figure 5.1.2.

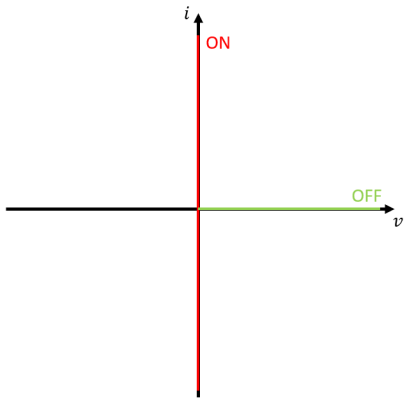

Figure 5.1.1: 4 quadrant representation of the NMOS switch

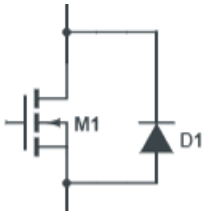

Figure 5.1.2: Switch used in the H-Bridge

The NMOS used to realize the switch has to be able to handle large values of current and voltage. The PV panel of the system outputs, at its MPP, more than 5 kW of power, at a current close to 45A, and for a maximum voltage of 150 V. The chosen transistors are IRFP260N HEXFET® Power MOSFET's from International Rectifier. They are capable of withstanding continuous drain current up to 50 A and drain-source voltages up to 200 V. These characteristics fit the requirements of the system, with a 5 A and 50 V margin. The characteristics of the IRFP260N are shown in table 5.1 and the complete datasheet can be found in annex D.

NMOS characteristics		units	value
Maximum drain-source voltage	$V_{DS,max}$	V	200
Maximum continuous drain current	$I_{D,max}$	A	50
Maximum power dissipation	$P_{D,max}$	W	300
Gate threshold voltage	$V_{GS(th)}$	V	2 - 4
Turn-ON delay + rise time	$t_{d(on)} + t_r$	ns	60 + 17
Turn-OFF delay + fall time	$t_{d(off)} + t_f$	ns	55 + 48

Table 5.1: IRFP260N characteristics

5.2 Circuit Analysis

The circuit in figure 5.0.1 shows the system with an ideal, lossless transformer between the H-bridge and the passive rectifier. The actual transformer has a circuit with added equivalent core and winding resistances, as well as added leakage and magnetizing inductances. The complete circuit with the real transformer can be seen in figure 5.2.1. The magnetizing inductance represents the magnetizing current, which is a part of the total current that is not transferred from the primary to the secondary windings, but that magnetizes the core instead. However, the core can not be magnetized forever, as it would reach magnetic saturation if that was the case. To avoid reaching magnetic saturation, the core has to be demagnetized, and the magnetizing current has to be returned to the circuit. This explains why we have an H-bridge before the primary, so that the magnetizing current has a triangular waveform, which represents the magnetizing and demagnetizing of the core.

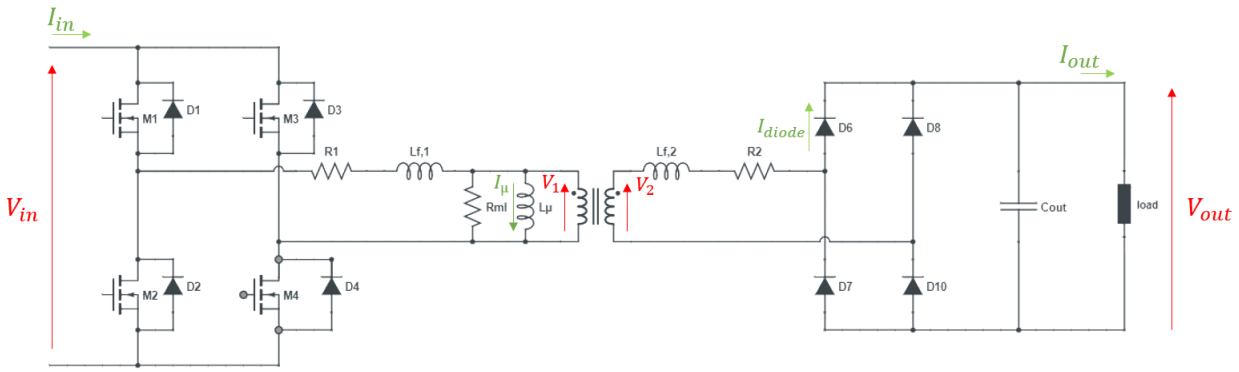

Figure 5.2.1: Complete equivalent of the DAB with the real transformer and passive rectifier

The flow inside the DAB when transistors $M_{1,4}$ and $M_{2,3}$ are ON is shown in figure 5.2.2. The waveforms of the voltages and currents across the DAB are shown in figure 5.2.3. The load requires a constant voltage, which is provided thanks to the diodes in the passive rectifiers and the smoothing output capacitance C_{out}. The amount of current exchanged is also dependent on the phase-shift of the command signals of the transistors making up the H-bridge. This phase-shift represents the portion of the switching period of the transistors M_1 and M_4 after which the transistors M_2 and M_3 will be set ON. The most current is exchanged when this phase-shift equals 50%, or $\phi = 180°$. Figure 5.2.4 shows different phase-shifts for the DAB.

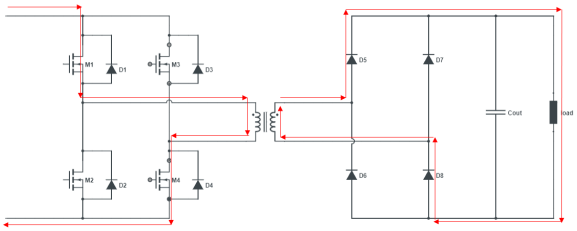

(a) Flow when transistors M1 and M4 are ON

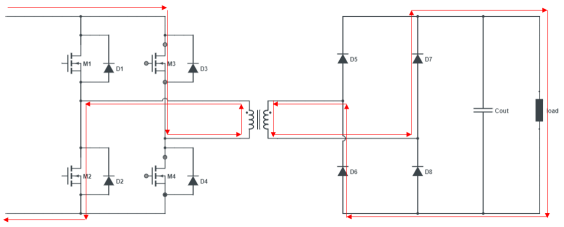

(b) Flow when transistors M2 and M3 are ON

Figure 5.2.2: Flow in the DAB

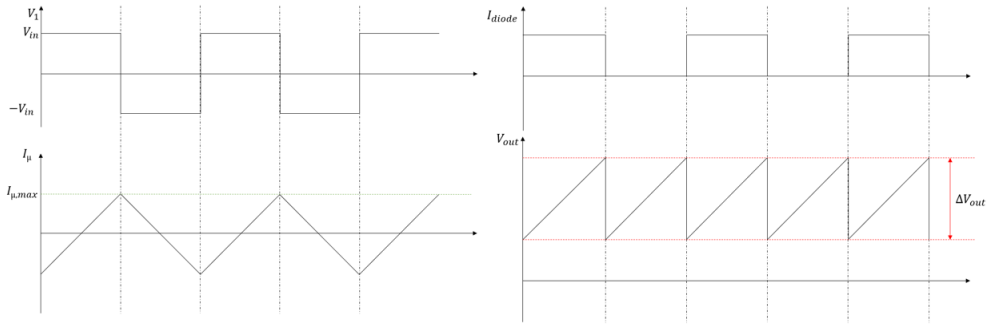

Figure 5.2.3: Important waveforms of the DAB

Now that the functioning of the DAB has been shown, it will be used in 3 different cases. The first case is when current is driving the DAB, which is equivalent to adding a current source as the input. The second case is when the DAB is driven by voltage. The final case is when the DAB is voltage driven but a capacitor is added at the output of the H-bridge to create a resonant circuit with the leakage and magnetizing inductances of the transformer. The 3 cases will then be compared, and the final system will be based on this comparison.

5.3 Current driven

Using the current characteristic of the solar array, it is possible to feed the DAB with a DC-current. For that it is necessary to add an inductance in series with the source, to force the source to the current characteristic of the solar array. The triple junctions solar cells constituting the array have an inside parasitic capacitance [16] [31], so the series inductance helps to smooth the current out of the solar panel, to keep a constant current, because the overlap presented in figure 5.3.1 means that the parasitic capacitance will not empty itself during commutation. The goal of the inverter is to create an oscillating current with an amplitude equal to the source current and a squared waveform. To do so, the switches 1 and 4 close and open at the same time, in alternance with the opening and the closing of the switches 2 and 3. This will feed the primary of the transformer with an alternating current, half of the time positive and half of the time negative.

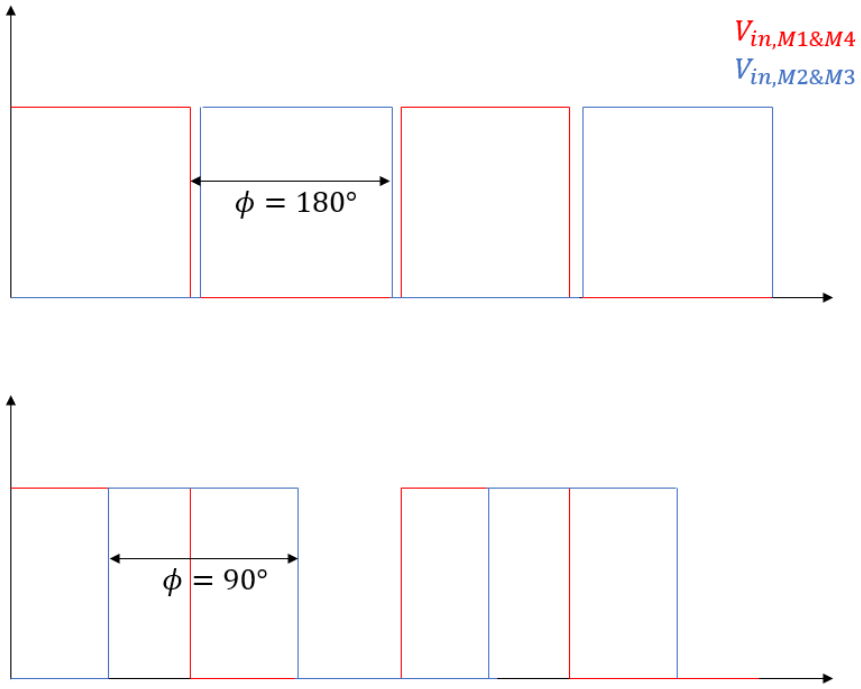

Figure 5.2.4: Phase-shift of the command signals

It is important to keep in mind that the current must always have a path to flow in, otherwise it will stagnate and over-voltages happen. To prevent this from happening, the command signals must overlap, like in figure 5.3.1. Having the command signals overlapping ensures that both switches S1 and S3 and both switches S2 and S4 can not be open at the same time and thus that there is always a path for the current to flow in.

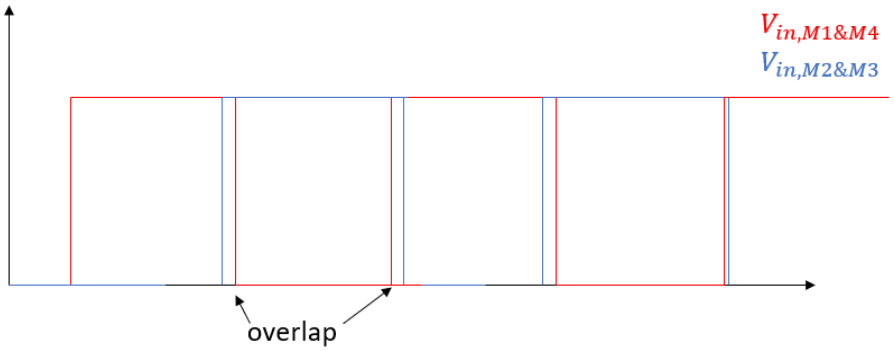

Figure 5.3.1: Overlapping command signals

However, additional losses occur when the two control signals overlap due to the turn OFF delay of the transistors. The turn OFF delay is the time between when the control signal goes to 0 and when the value of the current passing through the transistor reaches 90% of its maximum value. The turn OFF delay is part of the turn OFF time of the transistors. Voltage-driven DAB's use a parallel capacitance at the input of the H-Bridge and a deadband between the two control

signals instead of an overlap, and these two characteristics of the voltage-driven DAB will be helpful to reduce the losses induced by the storage time.

5.4 Voltage driven

To force the solar array onto its voltage characteristic, it is needed to add a capacitance in parallel with the solar array. This capacitance will act a voltage source at the scale of the commutation. The current exiting the bridge is no longer a square wave so there are no over-voltages to damp anymore. The parallel capacitance is a factor of additional losses, so it is important to size it well. Its value has been computed from the equation of a capacitance

$$I_{in} = C_{in}\frac{dV_{in}}{dt} \Rightarrow C_{in} = \frac{I \cdot \frac{1}{f_{sw}}}{\delta V} = 3\mu F \tag{5.4.1}$$

The output capacitance has an impact on the size of the ripples of the output voltage. A capacitance of $C_{out} = 500\mu F$ has been chosen, to have maximum ripples of $160mV$, as shown in figure 5.4.1.

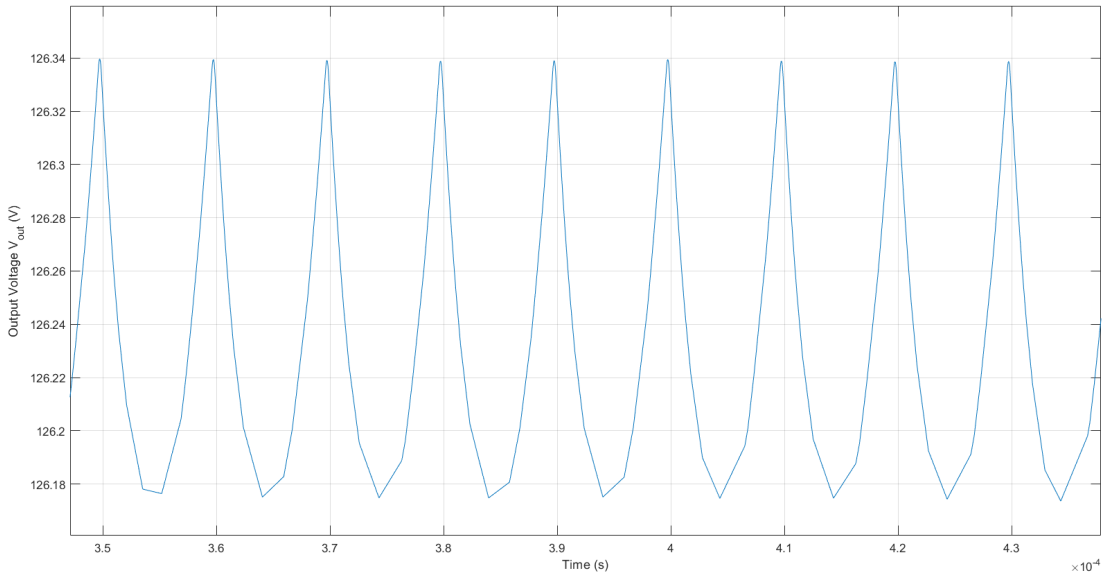

Figure 5.4.1: Output voltage ripples

The voltage driven DAB has an advantage over the current-driven topology, as it does not require an extra capacitance to damp over-voltages. Another change from the current-driven topology is that the control signals need a dead-band between them, to avoid to create a short-circuit to the ground and current spikes.

The transistors in the H-bridge used in the DAB are generators of two kind of losses, commutation losses and conduction losses. The conduction losses are present because when the transistor is ON and current flows through it, a small voltage difference is present at the terminals of the transistor, due to the transistor internal resistance. Switching losses are present because the turn ON and turn OFF of the transistor are not instantaneous. There is a small period of time during

the switching ON and the switching OFF of the transistor where there is both a positive current in the transistor and a positive voltage difference between its source and its drain. Theses two kind of losses are shown in figure 5.4.2.

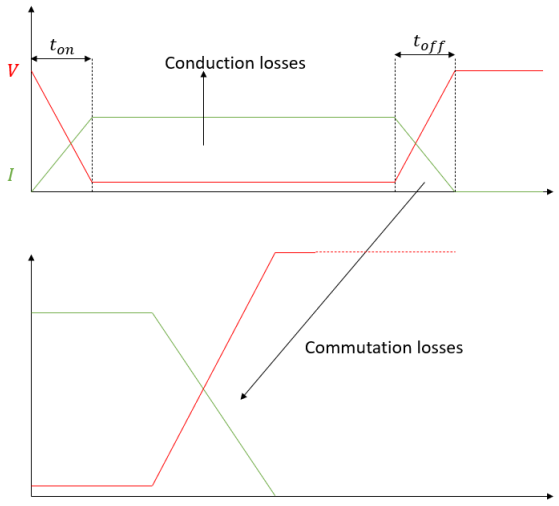

Figure 5.4.2: Conduction and Commutation Losses

The commutation losses can rise, although for a short moment, to very high values, which could be damaging for the transistor. Figure 5.4.3 shows the commutation losses for the voltage-driven DAB. The power dissipated in the transistor reaches 7 kW, albeit for a very short time (70ns). This is very damaging to the transistor as this power is dissipated in the form of heat. A solution exists to mitigate these losses, by adding a resonant tank.

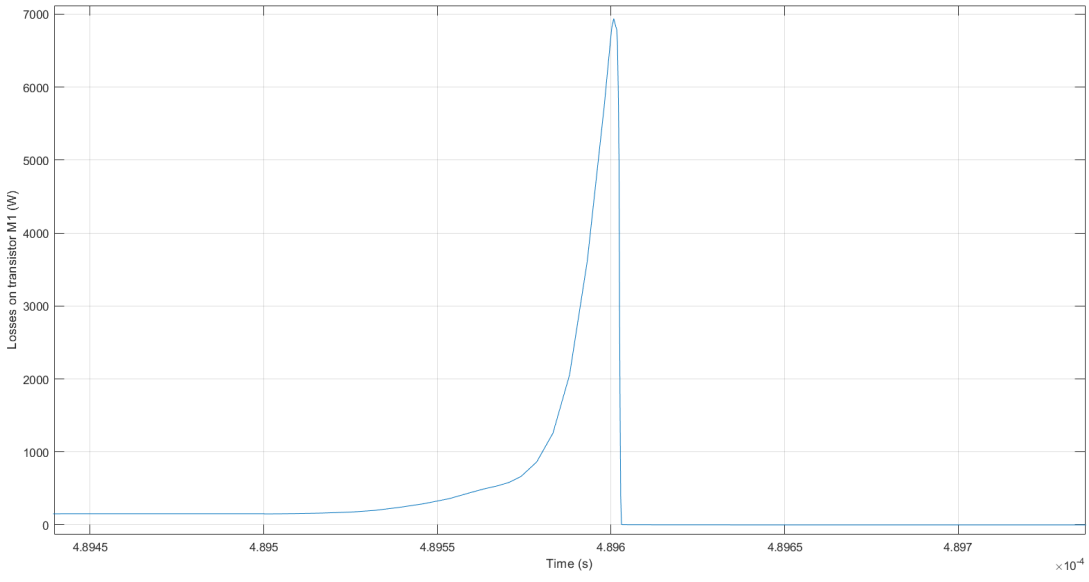

Figure 5.4.3: Commutation Losses on transistor M1

5.5 Resonant voltage driven

By adding a series capacitance at the exit of the H-bridge, it is possible to use the leakage inductance of the transformer as well as its magnetizing inductance to create an LLC resonant circuit. The advantage of such a circuit is to take advantage of the resonance such that at the commutation, the current is very low and thus the commutation losses are lowered. The method to size the capacitance to add is based on the method presented in [2]. Figure 5.5.1 shows the transformer circuit with an added capacitance to form an LLC resonant tank with the magnetizing and the leakage inductances. The voltage V_{sq} is a square voltage and the current I_{res} is the current that needs to be at low values when the voltage commutes.

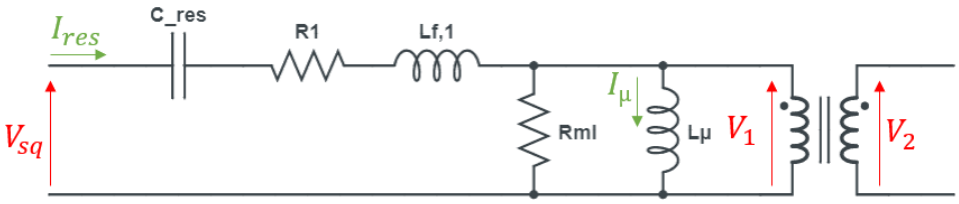

Figure 5.5.1: LLC resonant tank

By fixing a resonant frequency thanks to the value of C_{res}, 3 modes of operation can be used for the resonant DAB. These modes of operation are operation at, above, or below the resonant frequency. The operations mode above resonant frequency induces more losses because the first resonant half cycle of the DAB is not completed entirely (figure 5.5.2), as it is interrupted by the start of the other switching cycle. This leads to larger turn OFF losses, and hard commutation of the diodes in the rectifier part of the system. These phenomenons are shown in figure shown in figure 5.5.3. Operating below the resonant frequency allows to finish the resonant cycles, but adds an idle time called freewheeling operation, where the magnetizing inductance resonates with the leakage inductance and the resonant capacitance. No current flows through the transformer during this period, causing the secondary to "disconnect" from the primary. The current flows directly in the magnetizing inductance, and this causes increased conduction losses, because of the circulating energy. Working at the resonant frequency allows each resonant cycle to finish properly, and so the current in the leakage inductance is nearly zero when the switching occurs, which reduces the commutation losses. This is called Zero-Current Switching (ZCS).

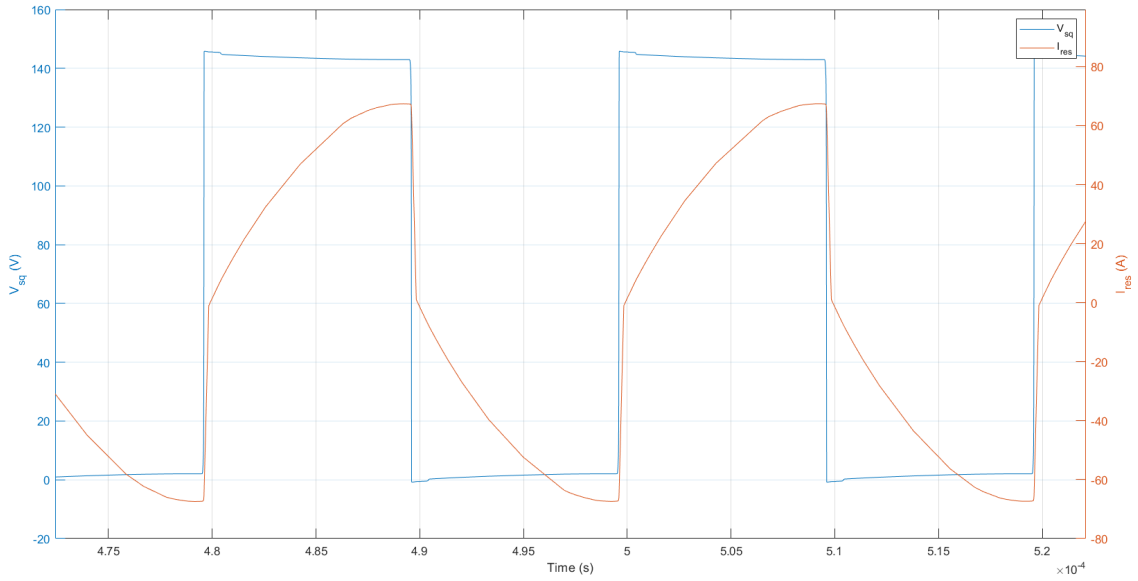

Figure 5.5.2: Interruption of the resonant cycle

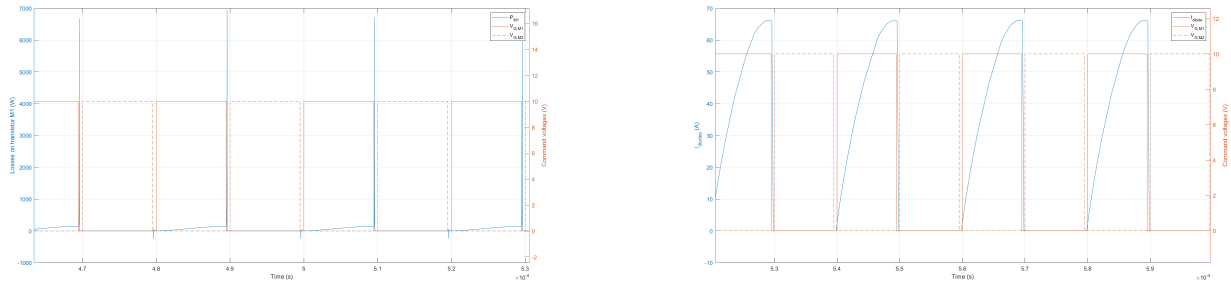

(a) Increased switch OFF losses

(b) Hard commutation of the rectifying diodes

Figure 5.5.3: Increased turn OFF losses and hard commutation of the diodes when $f_s < f_r$

This resonant tank has a voltage gain given by the magnitude of the transfer function, given in equation 5.5.1

$$K = \left| \frac{V_1}{V_{sq}} \right| = \frac{F^2 \cdot (m-1)}{\sqrt{(m \cdot F - 1)^2 + F^2 \cdot (F^2 - 1)^2 \cdot (m-1)^2 \cdot Q^2}} \tag{5.5.1}$$

Where:

- $F = \frac{f_s}{f_r}$ is the normalized switching frequency,
- $f_r = \frac{1}{2\pi\sqrt{L_{f,1} C_{res}}}$ is the ratio of switching frequency and the resonant frequency,

- $m = \frac{L_{f,1}+L_\mu}{L_{f,1}}$ is the ratio of total primary inductance to resonant inductance,

- $Q = \frac{\sqrt{\frac{L_{f,1}}{C_{res}}}}{R_{ac}}$ is the quality factor,

- R_{ac} is the reflected load resistance and is equal to $\frac{8 \cdot R_{load}}{\pi^2}$ for a transformer turn ratio equal to unity.

Figure 5.5.4 shows the gain of the resonant tank for a value m=3. It shows that the value of Q will depend on the load, with low Q corresponding to lower loads, while higher Q will correspond to higher loads. All the curves cross at $F_x = 1$, or when the resonant frequency is equal to the switching frequency. One can also trace a line linking the peaks of all the curves. The left side of this line is the capacitive region, and the right side is the inductive region. This is important, because the capacitive region is where Zero-Current Switching (ZCS) can be achieved, while the inductive region is where Zero-Voltage Switching (ZVS) can be achieved.

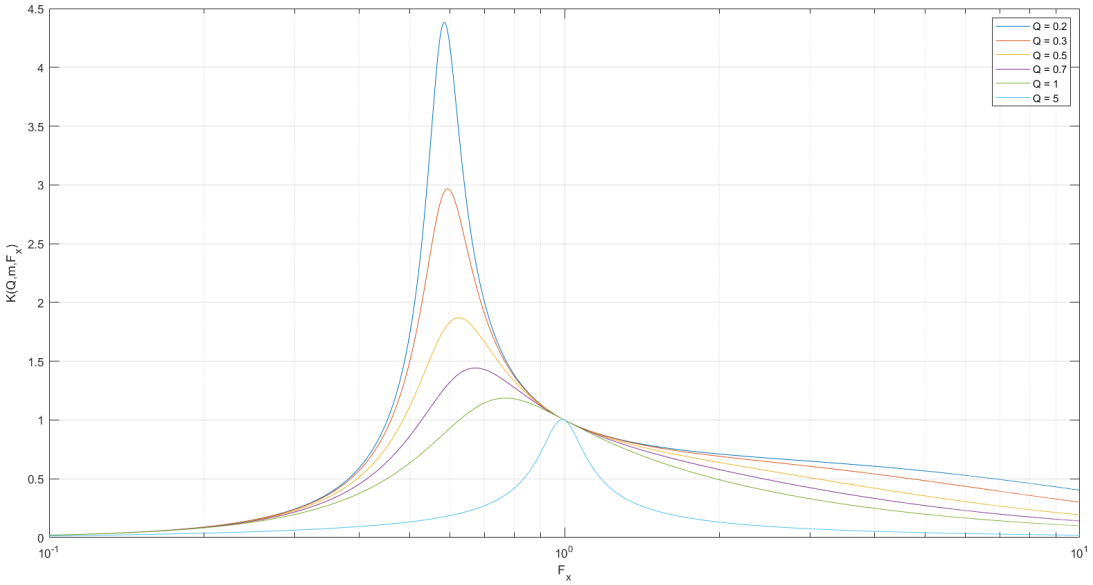

Figure 5.5.4: LLC resonant tank gain for m=3

In the case of the studied system, no extra inductor is added. As the value of the leakage inductance $L_{f,1}$ is very small compared to the value of the magnetizing inductance, the value of m is high

$$m = \frac{L_{f,1} + L_\mu}{L_{f,1}} = \frac{0.47\mu + 450\mu}{0.47\mu} = 958.44 \tag{5.5.2}$$

The resulting curves of the resonant tank gain are shown in figure 5.5.5. All the curves meet again when F_x equals 1. But none of them surpass a resonant tank gain of 1. The ratio F_x is thus set to 1, to have a resonant tank gain of 1, and to work at the resonant frequency and thus reduce

the commutation losses. As the value of the resonant frequency is now known, the value of the resonant capacitance can be computed

$$f_r = \frac{1}{2\pi\sqrt{L_{f,1}C_{res}}} \Rightarrow C_{res} = \frac{1}{4\pi^2 f_r^2 L_{f,1}} = 5.4\mu F \tag{5.5.3}$$

For practical uses, this value is rounded to the closest standard capacitor value, which is $4.7\mu F$. With this value, the actual resonant frequency is $f_r = 107kHz$ instead of $100kHz$. The operating mode in which the circuit operates is thus the mode where $f_s < f_r$, so ZCS will be achieved, but the conduction losses will be greater than if the system operated at $f_s = f_r$.

The value of Q can then finally be computed for an equivalent value of R_{load} at the MPP $R_{load} = 3\Omega$

$$Q = \frac{\sqrt{\frac{L_{f,1}}{C_{res}}}}{\frac{8 \cdot R_{load}}{\pi^2}} = 0.13 \tag{5.5.4}$$

The curve resonant tank gain for a quality factor $Q = 0.13$ and a ratio of total primary inductance to resonant inductance $m = 958.44$ is similar to the curve for $Q = 0.2$ on figure 5.5.5.

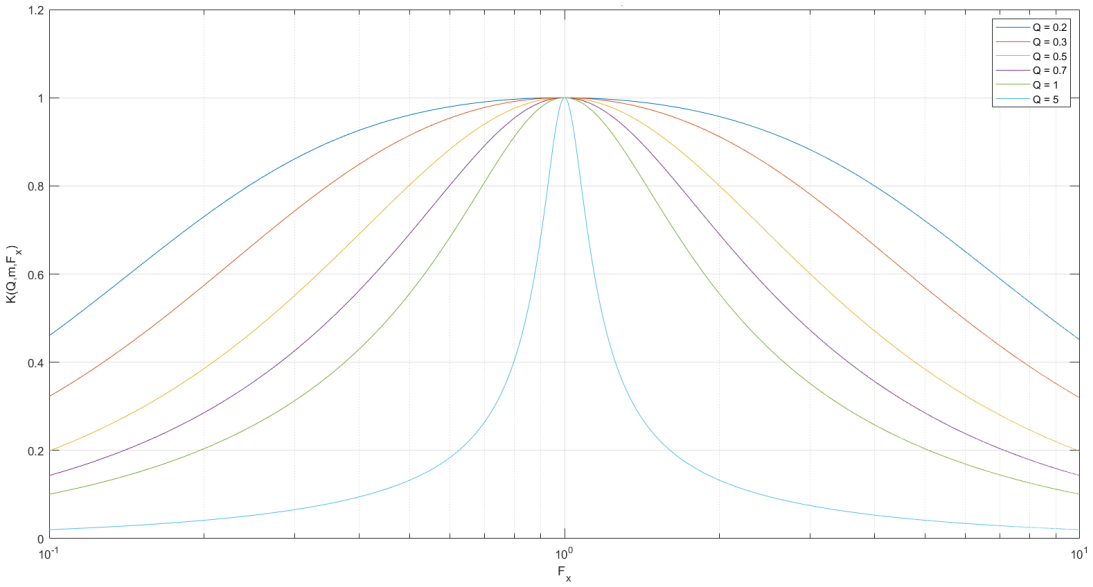

Figure 5.5.5: LLC resonant tank gain for m=958.44

The waveforms of the current I_{res} and the voltage V_{sq} shown in figure 5.5.6 show that, as the actual resonant frequency f_r is greater than the switching frequency f_s, near-ZCS is achieved, but an idle time causing greater conduction losses is also added.

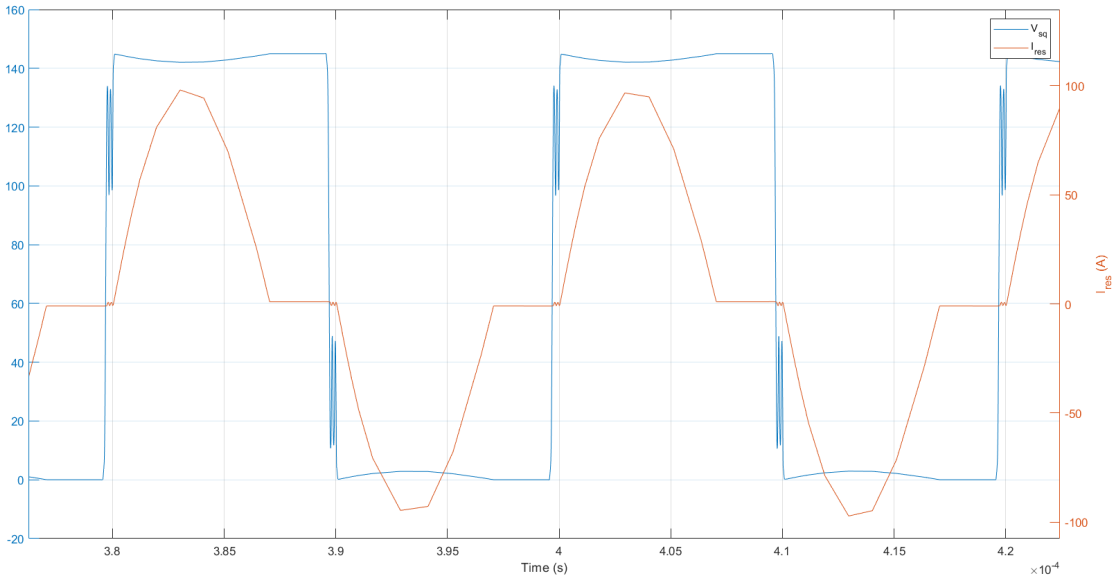

Figure 5.5.6: Near-ZCS of the resonant DAB

The conduction losses can be seen in figure 5.5.7, with the command signals of the transistor as a visual help to determine conduction from commutation losses. This figure also shows that the high commutation losses of the voltage-driven DAB have been effectively damped from 7 kW to less than 50W.

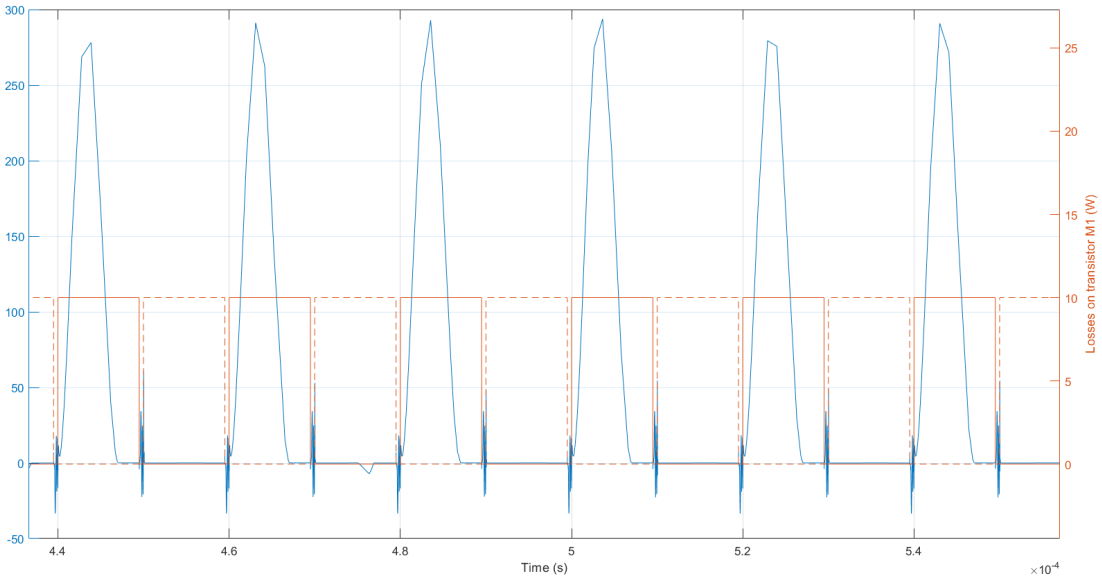

Figure 5.5.7: Losses in transistor M1

5.6 Comparison

The final system has been simulated using LTSpice. To reproduce the I/V and P/V curves of the solar panel after the power electronics circuit and the equivalent transformer circuit, a variable resistance going from very high values (to emulate an open-circuit) to very low values (to emulate a short-circuit) has to be used as the load. The resulting files are very large, because the values of the resistance have to be kept for some time in order to have a smooth curve. A small Python code has been written to reduce the size of the files, by keeping only increasing values for the output voltage. This code can be seen in appendix E.

The resulting P/V curves for the solar panel, a current-driven, a voltage-driven, and a resonant DAB can be seen in figure 5.6.1. As expected, the current-driven DAB has more losses than the other topologies because of the losses added during the overlap. The voltage-driven DAB issues more power at the MPP than the resonant DAB, which has additional conduction losses because of the idle time created by the fact that the resonant frequency is lower than the switching frequency. However, the voltage-driven DAB has commutation losses that go up to 7 kW, and that are harmful to the transistors. To increase the robustness of the system, a resonant DAB is chosen to link the satellite to the solar panel.

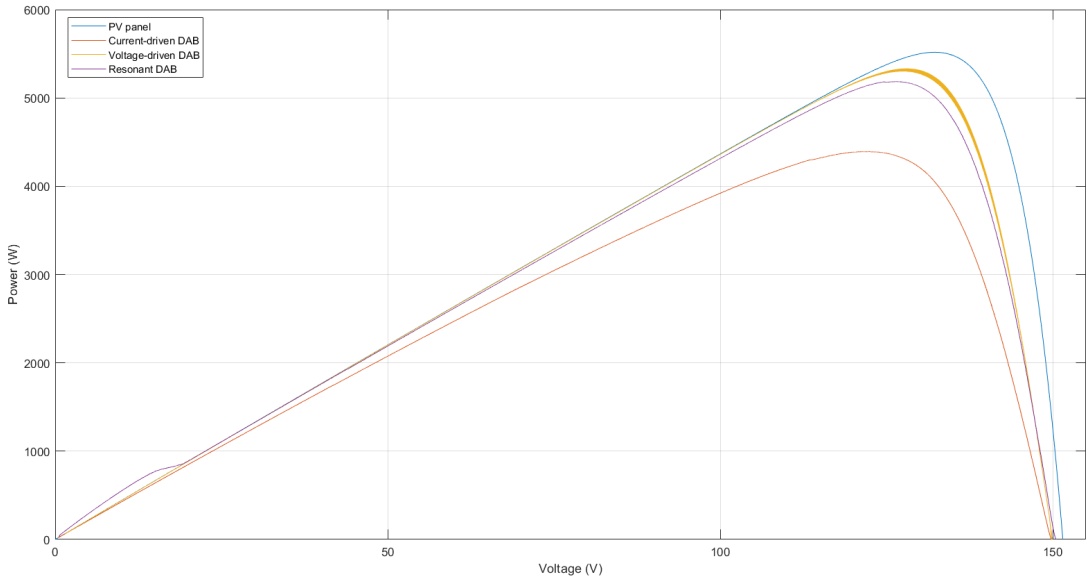

Figure 5.6.1: P/V curves for various system topologies

The resulting I/V and P/V curves can be seen in figure 5.6.2 and 5.6.3. The red line in figure 5.6.3 indicates 5000 W, which is the requirements of the system. It is used as a visual help to understand if the system meets the power requirement, which is the case. The vertical difference between the solar panel P/V curve and the P/V curve at the output of the system represents the total losses of the system. It can be observed that these losses increase when the voltage approaches the MPP voltage. The MPP of the solar panel is not the same as the MPP at the output, so it is important to use the output voltage when using MPPT methods.

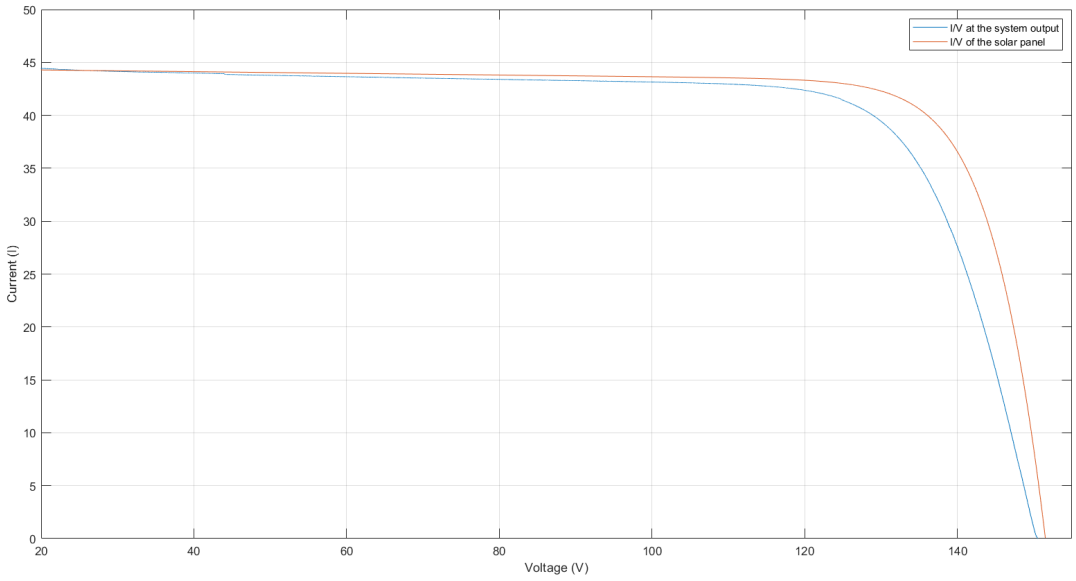

Figure 5.6.2: I/V curve of the system with resonant DAB

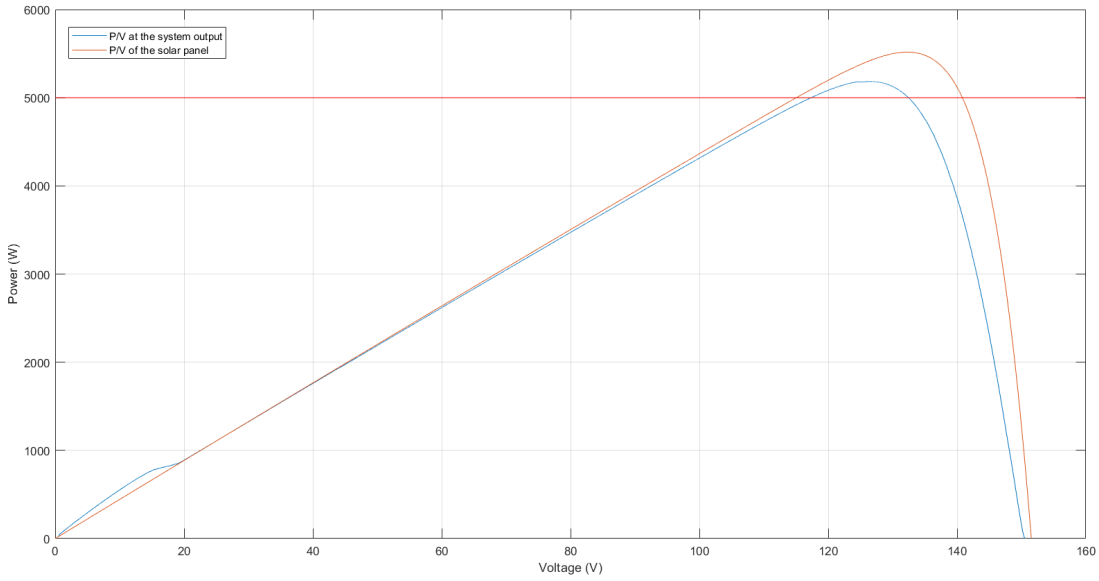

Figure 5.6.3: P/V curve of the system with resonant DAB

5.7 Effect of the phase-shift

The phase-shift between the command signals of transistors $M_{1,4}$ and $M_{2,3}$ is the only degree of freedom in the rotating part of the system. Indeed, the amount of current exchanged depends on the phase-shift. It was already stated in section 5.2 that the maximum amount of current is exchanged when the phase-shift is 50% or $\phi = 180°$. But it is interesting to see the relation between the phase-shift ϕ and the I/V curve present at the output of the system. Figure 5.7.1 shows the

I/V curves at the output of the system for different phase-shifts, from 45° to 160°, compared to the I/V curve for a maximum phase-shift of 180°. It can be observed that the resulting I/V curves are equivalent to the 180° phase-shift I/V curve, but divided by a factor equal to the phase-shift in degrees divided by 180. This result is expected as current only flows when one of the two command signals is at V_+, and no current flows if both command signals are at V_+ or none of them are. So the resulting current is the maximal current divided by the portion of time in a period where it flows, which is obtained by dividing the phase-shift by 180 degrees. As the I/V curves are influenced by the phase-shift ϕ, the P/V curves are influenced in the same fashion, so the phase-shift is a parameter that could be used to tweak the MPP of the system.

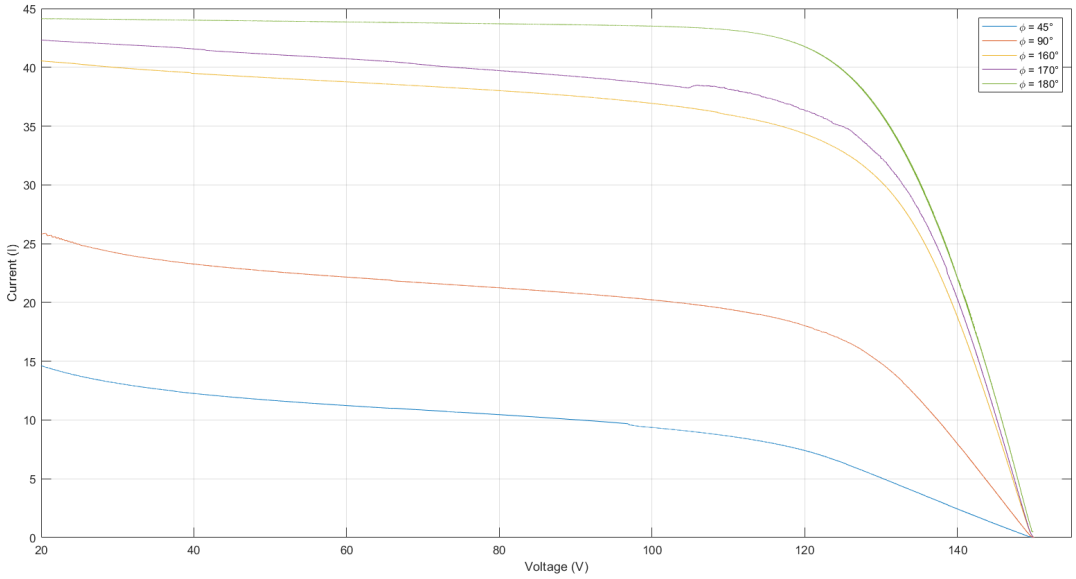

Figure 5.7.1: I/V curves for different phase-shifts

Conclusion and further work

The objective of this thesis was to design a system including a contactless power transfer to replace the slip rings technology currently used in satellites. The main study points were an approach to the existing works done in contactless power transfer, the accurate design and simulation of an authentic solar panel capable of delivering more than 5 kW of power, the geometrical and electrical design and understanding of a contactless transformer, and the design of an authentic power electronic converter, limiting the amount of losses and stress placed upon the entire system.

First, an introduction to the constraints found in a spatial environment aided the comprehension of why a contactless power transfer was needed to replace the current slip rings technology. Then, the state of the art on contactless power transfer showed the many different approaches and topologies available to realize this project. It helped to understand what topologies were best suited for the different parts composing the entire system.

The designing process of the solar panel was then explained. A theoretical background was used to model a single solar cell, and simulation tools were then used to simulate a whole panel capable of generating more than 5 kW of power under 150 V. The modeling and simulation of this panel was helpful to understand the effect of the contactless system on the I/V and P/V curves of the solar panel.

The chosen geometry for the contactless magnetic coupling element was a pot core transformer, and the actual transformer chosen was issued from a previous work realised by T. Deceuleneer [9]. Some models were introduced to understand how the pot core transformer was designed, and to understand the different principles acting on the transformer and influencing how it functions.

Finally, three different topologies of power electronics converters have been simulated and studied, to understand their impact on the working of the entire system and study the generated losses. The resulting power electronics converter is a resonant, voltage-driven DAB, which limits the high commutation losses generated in the transistors and harmful to the system. The comparison of the P/V curve of the solar panel previously simulated and the P/V curve at the output of the system shows that the resonant voltage-driven DAB is able to transfer 5 kW of power under 150 V effectively.

The work on this project can still be improved, by studying the addition of batteries to the system, after the solar array drive system and the power conditioning and distribution system of the satellite. It is also possible to improve the simulation of the entire system by adding a real, authentic alimentation system, taking into account the first moment when the solar panels of the satellite catch the sun rays, and the impact of eclipses on the system. Another possible point of

improvement can be made in adding an authentic command system, taking into account the difficulty of commanding a system that is not physically linked, and adding sensors and measurement methods to completely command the system and work at the MPP or at any point of the P/V curve found at the output of the system.

Bibliography

[1] Fredrik F. A. Van Der Pijl, Jan. A. Ferreira, Pavol Bauer, and Henk Polinder. Design of an inductive contactless power system for multiple users. In *Conference Record of the 2006 IEEE Industry Applications Conference Forty-First IAS Annual Meeting*, volume 4, pages 1876–1883, 2006.

[2] Sam Abdel-Rahman. Resonant llc converter: Operation and design. Infineon Technologies North America (IFNA) Corp., 2012.

[3] J.M. Barnard, J.A. Ferreira, and J.D. van Wyk. Sliding transformers for linear contactless power delivery. *IEEE Transactions on Industrial Electronics*, 44(6):774–779, 1997.

[4] T. Campi, S. Cruciani, G. Rodríguez, and M. Feliziani. Coil design of a wireless power transfer charging system for a drone. In *2016 IEEE Conference on Electromagnetic Field Computation (CEFC)*, pages 1–1, 2016.

[5] Mauro Carpita, Michael De Vivo, Serge Gavin, and Daniel Bommottet. A rotating contactless power transfer system for space applications. In *2014 International Symposium on Power Electronics, Electrical Drives, Automation and Motion*, pages 238–242, 2014.

[6] Wireless Power Consortium. Introduction to the power class 0 specification introduction to the power class 0 specification version 1.2.3 copyright wireless power consortium 2, 2017.

[7] Wireless Power Consortium. The qi wireless power transfer system power class 0 specification part 4: Reference designs the qi wireless power transfer system part 4: Reference designs power class 0 specification version 1.2.3 copyright wireless power consortium 2, 2017.

[8] Jeroen de Boeij, Elena Lomonova, Jorge Duarte, and Andre Vandenput. Contactless energy transfer to a moving actuator. In *Conference Record of the 2006 IEEE Industry Applications Conference Forty-First IAS Annual Meeting*, volume 4, pages 2020–2025, 2006.

[9] Thibaut Deceuleneer. Contactless power transfer through a rotating transformer for spatial application. *Ecole polytechnique de Louvain, Université catholique de Louvain*, 2016.

[10] Stefan Ditze, Achim Endruschat, Thomas Schriefer, Andreas Rosskopf, and Thomas Heckel. Inductive power transfer system with a rotary transformer for contactless energy transfer on rotating applications. pages 1622–1625, 2016.

[11] Andreas Doleschel and Michael Lege. Contactless solutions for radar rotary joint systems. In *2015 16th International Radar Symposium (IRS)*, pages 451–456, 2015.

[12] D. Dzung, C. Apneseth, J. Endresen, and J.-E. Frey. Design and implementation of a real-time wireless sensor/actuator communication system. In *2005 IEEE Conference on Emerging Technologies and Factory Automation*, volume 2, pages 10 pp.–442, 2005.

[13] A. Esser and H.-C. Skudelny. A new approach to power supplies for robots. *IEEE Transactions on Industry Applications*, 27(5):872–875, 1991.

[14] Nicola Femia, Giovanni Petrone, Giovanni Spagnuolo, and Massimo Vitelli. Optimization of perturb and observe maximum power point tracking method. *IEEE Transactions on Power Electronics*, 20:963–973, 7 2005.

[15] Y. Fujita, A. Hirotsune, and E. Amano. Contactless power supply for layer layer-selection selection-type recordable multi multi-layer optical disk. In *2006 Optical Data Storage Topical Meeting*, pages 252–254, 2006.

[16] A. Garrigos, J.M. Blanes, J.A. Carrasco, and J.B. Ejea. Influence of the parasitic solar array capacitance in the sequential switching shunt series regulator. In *MELECON 2006 - 2006 IEEE Mediterranean Electrotechnical Conference*, pages 1198–1201, 2006.

[17] T. Gerrits, D. C. J. Krop, L. Encica, and E. A. Lomonova. Development of a linear position independent inductive energy transfer system. In *2011 IEEE International Electric Machines Drives Conference (IEMDC)*, pages 1445–1449, 2011.

[18] Dirk Hirschmann, Christian P. Dick, Sebastian Richter, and Rik W. De Doncker. Design of a contactless rotary energy transmission for an industrial application. In *2008 IEEE Power Electronics Specialists Conference*, pages 4314–4319, 2008.

[19] C. Honsberg and S. Bowden. PVeductation - spectral response. `https://www.pveducation.org/pvcdrom/characterisation/spectral-response`. Accessed: 2010-03-27.

[20] Joe-Air Jiang, Tsong-Liang Huang, Ying-Tung Hsiao, Chia-Hong Chen, et al. Maximum power tracking for photovoltaic power systems. *Journal of Applied Science and Engineering*, 8(2):147–153, 2005.

[21] R Khezzar, M Zereg, and A Khezzar. Modeling improvement of the four parameter model for photovoltaic modules. *Solar Energy*, 110:452–462, 2014.

[22] Eun-Soo Kim and Yoon-Ho Kim. A contactless power supply for a dc power service. In *Journal of international Conference on Electrical Machines and Systems*, volume 1, pages 483–491. Journal of International Conference on Electrical Machines and Systems, 2012.

[23] Jozef Lastowiecki and Pawel Staszewski. Sliding transformer with long magnetic circuit for contactless electrical energy delivery to mobile receivers. *IEEE Transactions on Industrial Electronics*, 53(6):1943–1948, 2006.

[24] Jia-You Lee, Li-Yu Huang, and Chong-Yu Chen. Design and implementation of contactless maglev rotating power transfer system with new rotary inductive coupled structure. In *2016 IEEE 8th International Power Electronics and Motion Control Conference (IPEMC-ECCE Asia)*, pages 2442–2449, 2016.

[25] Jia-You Lee, Yen-Ting Lee, and Chih-Jen Hsieh. Study on active vertical maglev inductively coupled structure for contactless rotating power transfer system. In *2018 IEEE International Power Electronics and Application Conference and Exposition (PEAC)*, pages 1–6, 2018.

[26] J. Legranger, G. Friedrich, S. Vivier, and J. C. Mipo. Comparison of two optimal rotary transformer designs for highly constrained applications. In *2007 IEEE International Electric Machines Drives Conference*, volume 2, pages 1546–1551, 2007.

[27] Michael A Lieberman and Alan J Lichtenberg. *Principles of plasma discharges and materials processing*. John Wiley & Sons, 2005.

[28] Marcel Maier, Michael Hagl, Marco Zimmer, Jörg Heinrich, and Nejila Parspour. Design and construction of a novel rotating contactless energy transfer system for an electrical excited synchronous machine, 2016.

[29] E. Matagne. Énergie solaire photovoltaïque dépendance de la puissance vis à vis de l'éclairement. `https://perso.uclouvain.be/ernest.matagne/SOLAIRE/SEM02/S02P10.HTM`. Last updated: 2005-02-25, Accessed: 2022-03-27.

[30] Juergen Meins, Robert Czainski, and Faical Turki. Phase characteristics of resonant contactless high power supplies. *Przeglad Elektrotechniczny (Electrotechnical Review)*, (11):10–13, 2007.

[31] P Merhej, E Dallago, and D Finarelli. Effect of capacitance on the output characteristics of solar cells. In *6th Conference on Ph. D. Research in Microelectronics & Electronics*, pages 1–4. IEEE, 2010.

[32] Arash Momeneh, Miguel Castilla, Mohammad Moradi Ghahderijani, Jaume Miret, and Luis Garcia de Vicuna. Analysis, design and implementation of a residential inductive contactless energy transfer system with multiple mobile clamps. *IET Power Electronics*, 10(8):875–883, 2017.

[33] M. Sc. Artur J. Moradewicz. Contactless energy transmission system with rotatable transformer - modeling, analyze and design, 2008.

[34] Jonas Muhlethaler, Jürgen Biela, Johann Walter Kolar, and Andreas Ecklebe. Improved core-loss calculation for magnetic components employed in power electronic systems. *IEEE Transactions on Power Electronics*, 27(2):964–973, 2012.

[35] K.D. Papastergiou and D.E. Macpherson. Contact-less transfer of energy by means of a rotating transformer. In *Proceedings of the IEEE International Symposium on Industrial Electronics, 2005. ISIE 2005.*, volume 4, pages 1735–1740, 2005.

[36] K.D. Papastergiou, D.E. Macpherson, and F. Fisher. A 1kw phase-shifted full bridge converter incorporating contact-less transfer of energy. In *2005 IEEE 36th Power Electronics Specialists Conference*, pages 83–89, 2005.

[37] Konstantinos D. Papastergiou and D. Ewen Macpherson. An airborne radar power supply with contactless transfer of energy—part ii: Converter design. *IEEE Transactions on Industrial Electronics*, 54(5):2885–2893, 2007.

[38] Zhijun Qian, Osama Abdel-Rahman, Hussam Al-Atrash, and Issa Batarseh. Modeling and control of three-port dc/dc converter interface for satellite applications. *IEEE Transactions on Power Electronics*, 25(3):637–649, 2010.

[39] Djamila Rekioua and Ernest Matagne. *Optimization of photovoltaic power systems: Modelization, Simulation and Control*, volume 102. Springer Verlag, 2012.

[40] Ghislain Remy, Olivier Bethoux, Claude Marchand, and Hussein Dogan. Review of mppt techniques for photovoltaic systems. *Laboratoire de Génie Electrique de Paris (LGEP)/SPEE-Labs, Université Pierre et Marie Curie P*, 6, 2009.

[41] L Schirone, M Macellari, and A Schiaratura. Smp: a technique for mppt management. In *8th European Space Power Conference*, volume 661, page 47, 2008.

[42] Zhan Shen, Zhiguang Li, Long Jin, and Huai Wang. An ac resistance optimization method applicable for inductor and transformer windings with full layers and partial layers. In *2017 IEEE Applied Power Electronics Conference and Exposition (APEC)*, pages 2542–2548, 2017.

[43] J.P.C. Smeets, L. Encica, and E.A. Lomonova. Comparison of winding topologies in a pot core rotating transformer. In *2010 12th International Conference on Optimization of Electrical and Electronic Equipment*, pages 103–110, 2010.

[44] J.P.C. Smeets, D.C.J. Krop, J.W. Jansen, M.A.M. Hendrix, and E.A. Lomonova. Optimal design of a pot core rotating transformer. In *2010 IEEE Energy Conversion Congress and Exposition*, pages 4390–4397, 2010.

[45] J.P.C. Smeets, D.C.J. Krop, J.W. Jansen, and E.A. Lomonova. Contactless power transfer to a rotating disk. In *2010 IEEE International Symposium on Industrial Electronics*, pages 748–753, 2010.

[46] C. L. W. Sonntag, E. A. Lomonova, J. L. Duarte, and A. J. A. Vandenput. Specialized receivers for three-phase contactless energy transfer desktop applications. In *2007 European Conference on Power Electronics and Applications*, pages 1–11, 2007.

[47] Riccardo Trevisan. Contactless energy transfer techniques for industrial applications. power and data transfer to moving parts. 2016.

[48] Fredrik F. A. Van der Pijl, Pavol Bauer, Jan. A. Ferreira, and Henk Polinder. Quantum control for an experimental contactless energy transfer system for multiple users. In *2007 IEEE Power Electronics Specialists Conference*, pages 343–349, 2007.

[49] Pei Long Wang, Xiao Zhuo Xu, Bao Yu Du, Hai Chao Feng, Xu Dong Wang, and Ji Kai Si. Modeling and design optimization of contactless sliding transformer system for ropeless elevators. In *Applied Mechanics and Materials*, volume 416, pages 264–269. Trans Tech Publ, 2013.

[50] Wikipedia. Limite de shockley-queisser — wikipédia, l'encyclopédie libre, 2022. [En ligne; Page disponible le 9-février-2022].

[51] Shi-yao Zhu, Dong-xu Li, and Qing Luo. Effect of nonlinear factors on disturbance characteristics of the solar array drive system on spacecraft. In *The International Conference on Applied Nonlinear Dynamics, Vibration and Control*, pages 421–435. Springer, 2021.

Appendix

A Solar cell datasheet

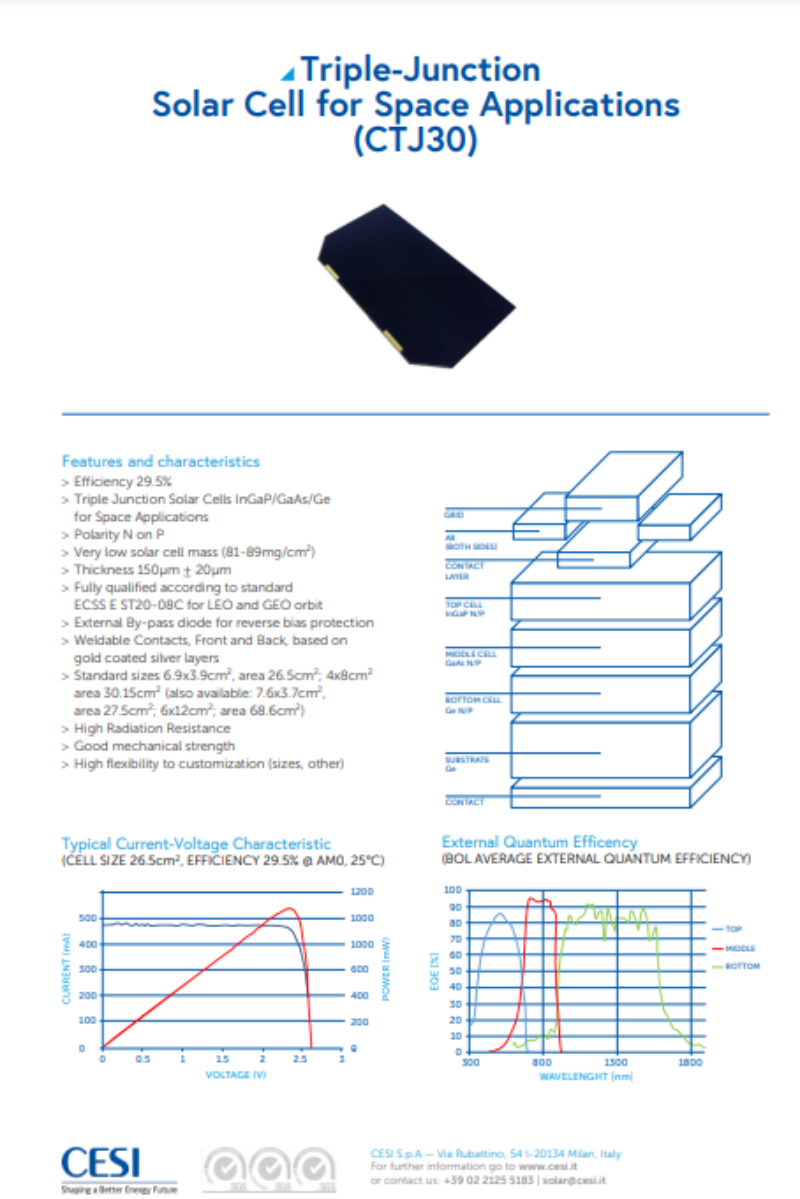

Triple-Junction
Solar Cell for Space Applications
(CTJ30)

Features and characteristics

> Efficiency 29.5%
> Triple Junction Solar Cells InGaP/GaAs/Ge for Space Applications
> Polarity N on P
> Very low solar cell mass (81-89mg/cm²)
> Thickness 150µm ± 20µm
> Fully qualified according to standard ECSS E ST20-08C for LEO and GEO orbit
> External By-pass diode for reverse bias protection
> Weldable Contacts, Front and Back, based on gold coated silver layers
> Standard sizes 6.9x3.9cm², area 26.5cm²; 4x8cm² area 30.15cm² (also available: 7.6x3.7cm², area 27.5cm²; 6x12cm², area 68.6cm²)
> High Radiation Resistance
> Good mechanical strength
> High flexibility to customization (sizes, other)

Typical Current-Voltage Characteristic
(CELL SIZE 26.5cm², EFFICIENCY 29.5% @ AM0, 25°C)

External Quantum Efficency
(BOL AVERAGE EXTERNAL QUANTUM EFFICIENCY)

CESI
Shaping a Better Energy Future

CESI S.p.A. – Via Rubattino, 54 I-20134 Milan, Italy
For further information go to www.cesi.it
or contact us: +39 02 2125 5183 | solar@cesi.it

Performance Data

(AVERAGE ELECTRICAL OUTPUT PARAMETERS @AM0, 1367 W/m² , T=25°C)

Area (cm^2)	I_{SC} (mA)	V_{OC} (V)	I_m (mA)	V_m (V)	P_{max} (W)	Eff (%)
26.5	473	2.6	455	2.32	1.05	29.0
30.15	538	2.61	517	2.33	1.20	29.0

Temperature Coefficients

Electron Energy	Fluence (e/cm^2)	$\Delta J_{SC}/\Delta T$ ($\mu A/cm^2/°C$)	$\Delta V_{OC}/\Delta T$ (mV/°C)	$\Delta J_{pmax}/\Delta T$ (µA/cm2/°C)	$\Delta V_{pm}/\Delta T$ (mV/°C)	$\Delta P_m/\Delta T$ ($\mu W/cm^2/°C$)
0	BOL	15.3	-5.324	12.9	-6.026	-77.8
1MeV	1E14	16.7	-5.589	14.3	-5.964	-73.0
1MeV	5E14	17.2	-5.670	14.0	-6.050	-72.3
1MeV	1E15	16.4	-5.677	17.1	-6.092	-61.5

Radiation Degradation (Remaining Factors)

Electron Energy	Fluence (e/cm^2)	I_{SC}	V_{OC}	P_M
1MeV	1E14	0.99	0.98	0.97
1MeV	5E14	0.96	0.95	0.91
1MeV	1E15	0.91	0.93	0.84

Proton Energy	Fluence (p/cm^2)	I_{SC}	V_{OC}	P_M
100 keV	1E10	0.99	0.98	0.96
100 keV	1E11	0.86	0.94	0.72
1MeV	1E10	1.00	0.98	0.98
1MeV	1E11	1.00	0.93	0.89
10MeV	1E11	1.00	0.99	0.98
10MeV	1E12	1.00	0.94	0.91

Qualification

Fully qualified according ECSS-E-ST-20-8C: "Photovoltaic Assemblies and components"

- Metal Contact thickness 5-10µm
- Degradation after reverse bias < 1%
- Contact Pull Strength > 500gr (4.9 N)
- Humidity and Temperature < 1%
- Solar Absorptance 0.903

CESI
Shaping a Better Energy Future

CESI S.p.A.— Via Rubattino, 54 I-20134 Milan, Italy
For further information go to www.cesi.it
or contact us: +39 02 2125 5183 | solar@cesi.it

B Ferrox datasheet

Material specification 3C90

3C90 SPECIFICATIONS

A low frequency power material for use in power and general purpose transformers at frequencies up to 0.2 MHz.

	CONDITIONS	VALUE	UNIT
μ_i	25 °C; ≤10 kHz; 0.25 mT	2300 ±20%	
μ_a	100 °C; 25 kHz; 200 mT	5500 ±25%	
B	25 °C; 10 kHz; 1200 A/m	≈ 470	mT
	100 °C; 10 kHz; 1200 A/m	≈ 380	mT
P_V	100 °C; 25 kHz; 200 mT	≤ 80	kW/m³
	100 °C; 100 kHz; 100 mT	≤ 80	
	100 °C; 100 kHz; 200 mT	≈ 450	
ρ	DC, 25 °C	≈ 5	Ωm
T_C		≥ 220	°C
density		≈ 4800	kg/m³

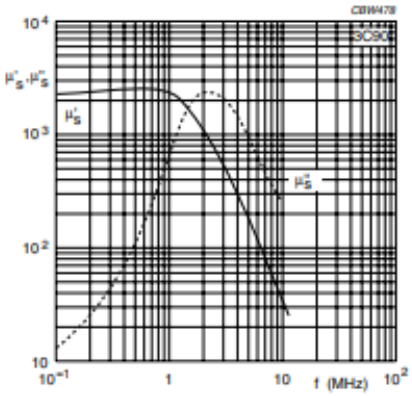

Fig.1 Complex permeability as a function of frequency.

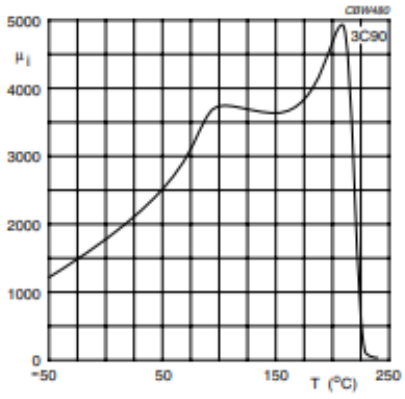

Fig.2 Initial permeability as a function of temperature.

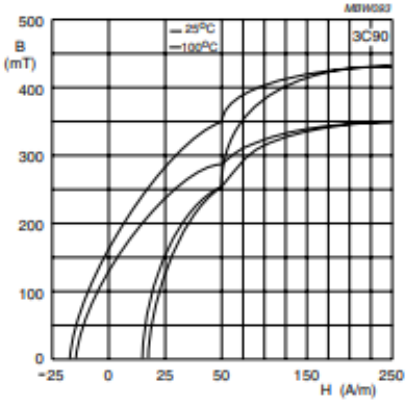

Fig.3 Typical B-H loops.

3C92 SPECIFICATIONS

A low frequency, high Bsat power material for use in power inductors at frequencies up to 0.2 MHz.

SYMBOL	CONDITIONS	VALUE	UNIT
μ_i	25 °C; ≤10 kHz; 0.25 mT	1500 ±20%	
μ_a	100 °C; 25 kHz; 200 mT	= 5000	
B	25 °C; 10 kHz; 1200 A/m	= 540	mT
	100 °C; 10 kHz; 1200 A/m	= 460	
	140 °C; 10 kHz; 1200 A/m	= 400	
P_V	100 °C; 100 kHz; 100 mT	= 50	kW/m³
	100 °C; 100 kHz; 200 mT	= 350	
ρ	DC; 25 °C	= 5	Ωm
T_C		≥ 280	°C
density		= 4800	kg/m³

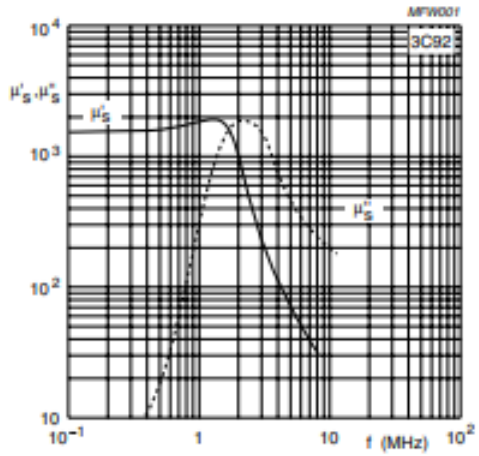

Fig.1 Complex permeability as a function of frequency.

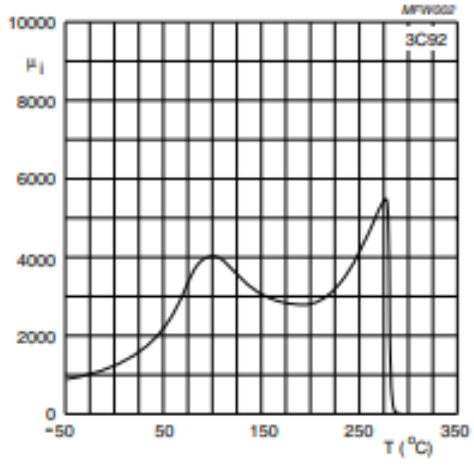

Fig.2 Initial permeability as a function of temperature.

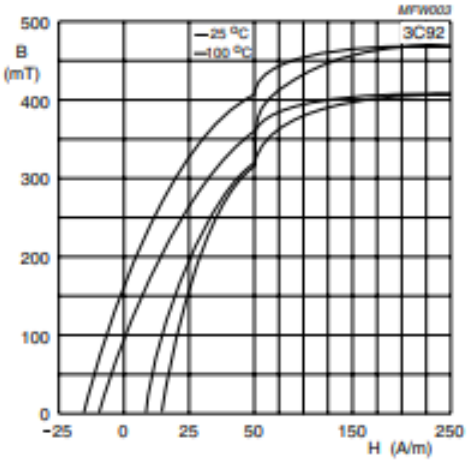

Fig.3 Typical B-H loops.

E cores and accessories — E71/33/32

CORE SETS

Effective core parameters

SYMBOL	PARAMETER	VALUE	UNIT
$\Sigma(l/A)$	core factor (C1)	0.218	mm^{-1}
V_e	effective volume	102000	mm^3
l_e	effective length	149	mm
A_e	effective area	683	mm^2
A_{min}	minimum area	676	mm^2
m	mass of core half	≈ 260	g

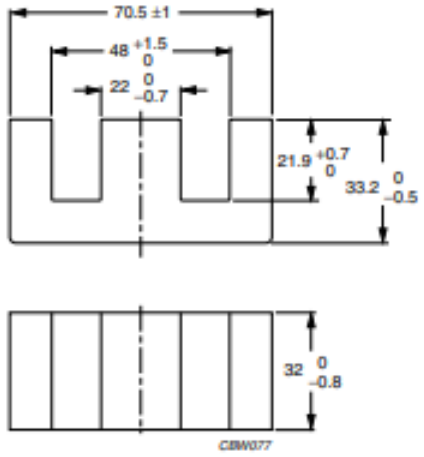

Dimensions in mm.

Fig.1 E71/33/32 core half.

Core halves

A_L measured in combination with a non-gapped core half, clamping force for A_L measurements 60 ±20 N, unless stated otherwise.

GRADE	A_L (nH)	μ_e	TOTAL AIR GAP (μm)	TYPE NUMBER
3C90	100 ±5%(1)	≈ 17	≈ 17800	E71/33/32-3C90-E100
	160 ±5%(1)	≈ 28	≈ 9620	E71/33/32-3C90-E160
	250 ±5%(1)	≈ 43	≈ 5280	E71/33/32-3C90-E250
	315 ±5%(1)	≈ 55	≈ 3900	E71/33/32-3C90-E315
	400 ±8%(1)	≈ 69	≈ 2860	E71/33/32-3C90-E400
	630 ±10%(1)	≈ 109	≈ 1620	E71/33/32-3C90-E630
	10800 ±25%	≈ 1880	≈ 0	E71/33/32-3C90
3C92 des	8000 ±25%	≈ 1390	≈ 0	E71/33/32-3C92
3C94	10800 ±25%	≈ 1880	≈ 0	E71/33/32-3C94
3C95 des	13330 ±25%	≈ 2315	≈ 0	E71/33/32-3C95
3F3	100 ±5%(1)	≈ 17	≈ 17800	E71/33/32-3F3-E100
	160 ±5%(1)	≈ 28	≈ 9620	E71/33/32-3F3-E160
	250 ±5%(1)	≈ 43	≈ 5280	E71/33/32-3F3-E250
	315 ±5%(1)	≈ 55	≈ 3900	E71/33/32-3F3-E315
	400 ±8%(1)	≈ 69	≈ 2860	E71/33/32-3F3-E400
	630 ±10%(1)	≈ 109	≈ 1620	E71/33/32-3F3-E630
	10000 ±25%	≈ 1740	≈ 0	E71/33/32-3F3

Note

1. Measured in combination with an equal gapped core half.

C Litz wire datasheet

Structure		External diameter without wrapping		External diameter with wrapping 1 x 52 (1 x Natural silk)		External diameter with wrapping 2 x 52 (2 x Natural silk)		Cross-section	DC-Resistance at 20°C (68°F)			Metres per kg
No. of strands	diameter of single wire [mm]	min [mm]	max [mm]	min [mm]	max [mm]	min [mm]	max [mm]	[mm²]	min [Ω/km]	nno [Ω/km]	max [Ω/km]	nom [m/kg]
	0.016	Other dimensions on request										
	AWG 54											
	0.020	Other dimensions on request										
	AWG 52											
	0.022	Other dimensions on request										
	AWG 51											
	0.025	Other dimensions on request										
	AWG 50											
10		0.127	0.142	0.157	0.177	0.187	0.212	0.00707	2176	2467	2713	11764
20		0.179	0.200	0.209	0.235	0.239	0.270	0.01414	1088	1233	1357	6060
25								0.01767				4964
30								0.02121				3921
35				External diameter depending on type of wrapping. Dimensions on request				0.02474				3355
45								0.03181				2611
60	0.03							0.04241				1960
75								0.05301				1567
90	AWG 48							0.06362				1307
105								0.07422				1119
120								0.08482				980
135								0.09542				871
180								0.12723				653
225								0.15904				522
270								0.19085				435
Other types of litz wire up to external diameter 11 mm on request												
10		0.164	0.186	0.194	0.221	0.224	0.256	0.01282	1228	1387	1522	7847
12		0.183	0.208	0.213	0.243	0.243	0.278	0.1538	1023	1156	1268	6536
15		0.201	0.229	0.236	0.269	0.261	0.299	0.01923	819	925	1015	5229
20		0.232	0.264	0.267	0.304	0.292	0.334	0.02564	614	694	761	3922
25		0.260	0.295	0.295	0.335	0.320	0.365	0.03204	491	555	609	3137
30		0.284	0.323	0.319	0.363	0.344	0.393	0.03845	409	462	522	2615
35		0.307	0.349	0.342	0.389	0.367	0.419	0.04486	351	396	448	2241
45	0.04	0.348	0.395	0.383	0.435	0.408	0.465	0.0568	273	308	348	1743
60		0.405	0.460	0.440	0.500	0.465	0.530	0.07691	205	231	266	1231
75	AWG 46	0.453	0.515	0.488	0.555	0.513	0.585	0.09613	164	185	213	985
90		0.497	0.565	0.532	0.605	0.567	0.645	0.11536	136	154	178	821
105		0.537	0.610	0.572	0.650	0.607	0.690	0.3459	117	132	152	704
120		0.572	0.650	0.607	0.690	0.642	0.730	0.5381	102	116	133	615
135		0.607	0.690	0.642	0.730	0.677	0.770	0.7304	91	103	118	547
180		0.722	0.820	0.757	0.860	0.792	0.900	0.23072	68	77	90	385
225		0.805	0.915	0.840	0.955	0.895	1.015	0.26840	55	62	72	308
270		0.884	1.005	0.919	1.045	0.974	1.105	0.34608	45.5	51.4	60.3	257
Other types of litz wire up to external diameter 11 mm on request												
6		0.162	0.179	0.192	0.214	0.222	0.249	0.01202	1320	1480	1613	8505
8		0.186	0.206	0.216	0.241	0.246	0.276	0.01602	990	1100	1210	6379
10		0.209	0.231	0.244	0.271	0.269	0.301	0.02003	792	888	968	5103
12		0.232	0.257	0.267	0.297	0.292	0.327	0.02403	660	740	807	4253
15		0.256	0.283	0.291	0.323	0.316	0.353	0.03004	528	592	645	3402
20		0.295	0.327	0.330	0.367	0.355	0.397	0.04006	396	444	484	2552
25		0.330	0.366	0.365	0.406	0.390	0.436	0.05007	317	355	387	2041
30		0.362	0.401	0.397	0.441	0.422	0.471	0.06008	264	296	332	1701
35	0.05	0.391	0.433	0.426	0.473	0.451	0.503	0.07	226	254	285	1458
45		0.443	0.490	0.478	0.530	0.503	0.560	0.09012	176	197	222	1134
60	AWG 44	0.515	0.570	0.550	0.610	0.585	0.650	0.12017	132	148	169	801
75		0.577	0.639	0.612	0.679	0.647	0.719	0.15021	106	118	136	641
90		0.633	0.701	0.668	0.741	0.703	0.781	0.18025	88	99	113	534
105		0.683	0.756	0.718	0.796	0.753	0.836	0.21029	75	85	97	458
120		0.728	0.806	0.763	0.846	0.798	0.886	0.24033	66	74	85	400
135		0.773	0.856	0.808	0.896	0.863	0.956	0.27037	59	66	75	356
180		0.918	1.017	0.953	1.057	1.008	1.117	0.36050	44.0	49.3	57.6	250
225		1.025	1.135	1.060	1.175	1.115	1.235	0.45062	35.2	39.5	46.0	200
270		1.126	1.246	1.161	1.286	1.216	1.346	0.54075	29.3	32.9	38.4	167
Other types of litz wire up to external diameter 11 mm on request												
3		0.163	0.189	0.193	0.224	0.223	0.259	0.01212	1331	1468	1578	8537
5		0.205	0.238	0.240	0.278	0.265	0.308	0.02019	799	881	947	5122
6		0.220	0.254	0.255	0.294	0.280	0.324	0.02423	666	734	789	4268
8		0.253	0.293	0.288	0.333	0.313	0.363	0.03231	499	551	592	3201
10		0.283	0.328	0.318	0.368	0.343	0.88	0.4038	399	440	473	2561
12		0.315	0.365	0.350	0.405	0.375	0.435	0.04846	333	367	394	2134
15		0.347	0.402	0.382	0.442	0.407	0.472	0.06058	266	294	316	1702
20		0.401	0.464	0.436	0.504	0.461	0.534	0.08077	200	220	237	1280
25		0.448	0.519	0.483	0.559	0.508	0.589	0.10096	160	176	189	1024
30		0.491	0.568	0.526	0.608	0.561	0.648	0.12115	133	147	163	854
35		0.530	0.614	0.565	0.654	0.600	0.694	0.14134	114	126	139	732
45		0.601	0.696	0.636	0.736	0.671	0.776	0.18173	89	98	108	570
60		0.699	0.810	0.734	0.850	0.769	0.890	0.24230	67	73	83	402
75		0.783	0.906	0.813	0.946	0.873	1.006	0.30288	53	59	66	322
90		0.859	0.994	0.894	1.034	0.949	1.094	0.36345	44.4	48.9	55.2	268
105		0.927	1.074	0.962	1.114	1.017	1.174	0.42403	38.0	41.9	47.3	230
120	0.071	0.988	1.144	1.023	1.184	1.078	1.244	0.4846	33.3	36.7	41.4	201
135		1.049	1.214	1.084	1.254	1.139	1.314	0.54518	29.6	32.6	36.8	179
180	AWG 41	1.246	1.443	1.281	1.483	1.336	1.543	0.72691	22.2	24.5	28.2	126
225		1.391	1.610	1.426	1.650	1.481	1.710	0.90864	17.8	19.6	22.5	107
270		1.528	1.769	1.563	1.809	1.618	1.869	1.09036	14.8	16.3	18.8	94
315		1.649	1.910	1.684	1.950	1.739	2.010	1.27209	12.7	14.0	16.1	72
405		1.870	2.165	1.905	2.205	1.960	2.265	1.63555	9.9	10.9	12.5	56
420			2.13					1.67	9.5	10.5	11.3	54
525			2.39	External diameter depending on type of wrapping. Dimensions on request				2.09	7.6	8.4	9.0	43
630			2.61					250	6.3	7.0	7.5	36
735			2.82					2.92	5.4	6.0	6.4	31
840			3.03					3.33	4.8	5.2	5.6	27
945			3.20					3.75	4.3	4.7	5.0	24
1260			3.70					5.00	3.2	3.5	3.8	17
1575			4.15					6.21	2.5	2.8	3.0	13
1890			4.55					7.49	2.1	2.3	2.5	11
2205			4.86					8.74	1.8	2.0	2.1	10
2835			5.60					11.23	1.4	1.6	1.7	7.5

PACK Feindrähte

Rudolf Pack GmbH & Co.
Am Bäkweg 9-11
D-51645 Gummersbach

Tel.: +49/(0) 22 61/95 67- 0
Fax: +49/(0) 22 61/95 67-67

www.pack-feindraehte.de
info@pack-feindraehte.de

Technical Data

RUPALIT® Litz wire

(The technical data comply in part with the specification given in standard IEC 60317-11)

RUPALIT® high-frequency litz wires are constructed from enamelled copper wire (magnet wire) made of RUPOL®, RUPEX® or RUTHERM® – see illustrations below. (Aluminium magnet wires on request)

On special request, we can also supply any other design of litz wire up to an overall cross-section of 1.000 mm².

For further information, please refer to our Data Sheets

RUPALIT®

RUPALIT®

RUPALIT® Profile

RUPALIT® Planar

RUPALIT® Safety (IEC 60950)

RUPALIT® Safety Profile (IEC 60950)

RUPALIT® Braided

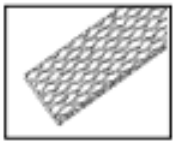

RUPALIT® 05

RUPOL® Safety (IEC 60950)

RUPA® Profile

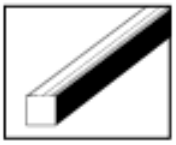

D Transistor datasheet

International
IOR Rectifier

PD - 94004B

IRFP260N

HEXFET® Power MOSFET

- Advanced Process Technology
- Dynamic dv/dt Rating
- 175°C Operating Temperature
- Fast Switching
- Fully Avalanche Rated
- Ease of Paralleling
- Simple Drive Requirements

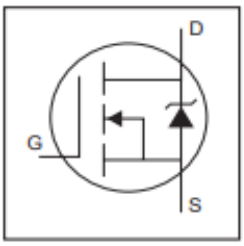

V_{DSS} = 200V

$R_{DS(on)}$ = 0.04Ω

I_D = 50A

Description

Fifth Generation HEXFETs from International Rectifier utilize advanced processing techniques to achieve extremely low on-resistance per silicon area. This benefit, combined with the fast switching speed and ruggedized device design that HEXFET Power MOSFETs are well known for, provides the designer with an extremely efficient and reliable device for use in a wide variety of applications.

The TO-247 package is preferred for commercial-industrial applications where higher power levels preclude the use of TO-220 devices. The TO-247 is similar but superior to the earlier TO-218 package because of its isolated mounting hole.

TO-247AC

Absolute Maximum Ratings

	Parameter	Max.	Units
I_D @ T_C = 25°C	Continuous Drain Current, V_{GS} @ 10V	50	A
I_D @ T_C = 100°C	Continuous Drain Current, V_{GS} @ 10V	35	
I_{DM}	Pulsed Drain Current ①	200	
P_D @T_C = 25°C	Power Dissipation	300	W
	Linear Derating Factor	2.0	W/°C
V_{GS}	Gate-to-Source Voltage	±20	V
E_{AS}	Single Pulse Avalanche Energy②	560	mJ
I_{AR}	Avalanche Current①	50	A
E_{AR}	Repetitive Avalanche Energy①	30	mJ
dv/dt	Peak Diode Recovery dv/dt ③	10	V/ns
T_J T_{STG}	Operating Junction and Storage Temperature Range	-55 to +175	°C
	Soldering Temperature, for 10 seconds	300 (1.6mm from case)	
	Mounting torque, 6-32 or M3 srew	10 lbf•in (1.1N•m)	

Thermal Resistance

	Parameter	Typ.	Max.	Units
$R_{\theta JC}$	Junction-to-Case	—	0.50	°C/W
$R_{\theta CS}$	Case-to-Sink, Flat, Greased Surface	0.24	—	
$R_{\theta JA}$	Junction-to-Ambient	—	40	

E Python code to reduce the size of the files issued by LTSpice

This small code is used to resize large LTSpice output files. It reads every line of the file, and rewrites in an other file only the lines where the voltage has increased. This is also useful to have a monotonically increasing value for the voltage.

```python
with open("large file path") as data:
    with open("resized file path", "w") as f:
        prev = 0
        next(data)
        for line in data:
            split = line.split() # [time, v_out, Res]
            val = float(split[2])
            if val > prev:
                f.write(line)
                prev = val
```

Figure E.1: Python code to resize large LTSpice files

UNIVERSITÉ CATHOLIQUE DE LOUVAIN
École polytechnique de Louvain
Rue Archimède, 1 bte L6.11.01, 1348 Louvain-la-Neuve, Belgique | **www.uclouvain.be/epl**